Integrated optical sensors based on semiconductor lasers and ring resonators using intensity interrogation

Jinyan Song

Thèse de doctorat
de l'Université Paris-Sud

Ecole doctorale Ondes et Matière
Spécialité : Physique

Présentée par Jinyan Song
Pour obtenir le grade de docteur de l'Université Paris-Sud

Capteurs optiques intégrés basés sur des lasers à semiconducteur et des résonateurs en anneaux interrogés en intensité

Soutenue le 14 décembre 2012
devant la commission d'examen :

Monsieur Niko HILDEBRANDT	Président
Monsieur Guanghua DUAN	Rapporteur
Madame Sara DUCCI	Rapporteur
Monsieur Jian-Jun HE	Co-directeur de thèse
Madame Qingli KOU	Co-directrice de thèse
Madame Sophie BOUCHOULE	Invitée

The Ph.D. journey is an uncertain adventure full of unexpected challenges. Many people offered me support and encouragement during the last several years to help me get through and reach the final stage. They make this journey both enjoyable and productive. Here I want to say thank you to many people along with me.

First and foremost, I would like to thank Dr. Qingli Kou for being an amiable, understanding, and supportive advisor. Her training and advice have helped me to grow as a scientist. Her encouragement always could inspire me during the hard time. I always remember her support from my very first day to the very last in France. Equally, I appreciate Prof. Jianjun He for his inspiring suggestions and guide across the whole project. Whenever I encountered bottleneck, he always helped me and show me the way out. The discussions with him are always constructive and fruitful.

I am grateful to Prof. Sara Ducci from University of Paris7 and Dr. Guanghua Duan from III-V lab for their patient review and constructive suggestions on my manuscript. Furthermore, I would like to thank them for attending my defense as jury members. I also appreciate Prof. Niko Hildebrandt from IEF for being the president of my defense and showing me his well equipped lab and amazing work on biosensing applications.

Especially, I appreciate Dr. Sophie Bouchoule at LPN for her comprehensive training on clean room techniques for semiconductor fabrication. She helped me a lot during the development of the device. I also appreciate Dr. Mingyu Li and Dr. Lei Wang for the informative and helpful communication. During my stay in China, they are always approachable and available.

Many others have also contributed to this work. I would say thank you to my colleagues at ISMO, LPN, IEMN and EDOM, including Philippe Bréchignac (Director of ISMO), Marie-Claire Paul, Bénédicte Daly, Laurent Berger, Catherine Salou, Emilie Bulard, Guillaume Aubry, Sandrine Lacombe, Jean-Yves Marzin (Director of LPN), Jean-Christophe Harmand, Elisabeth Galopin, Gille Patrarche, Yacomotti Alejandro, Cambril Edmond, Guy Aubin, Jean-Louis Oudar, Anthony Martinez, Kamel Merghem, David Chouteau, Stephane Guilet, Xavier Lafosse, Laurent Couraud, Zheng Han, Zhuang Zhao, Quan Dong, David Troadec, Bernard Bourguignon (Director of EDOM), Christophe Blondel, Martine Basset...Thank you for making the experience in France colorful and memorable.

Equally, I am grateful to all the people form IOE at Zhejiang University, including Tingting Lang, Lei Jin, Tingting Yu, Min Lou, Jialiang Jin, Shenghua Peng, Jianjun Meng, Jun Zou, Xianxin Jiang, Wenxiong Wei, Lin Wu, Xiang Xia, Xiao Ma, Ying Wang, Yu Hu, Sen Zhang, Luping Zhu, Hongli Zhu… You make IOE like a warm family.

Finally, I would like to thank my family. Thank you to my parents for alway being supportive and tolerant. You are my role model for being honest and brave. Thank you to my young brother. He is optimistic and when I was abroad, he accompanied my parents well. I also appreciate my lovely wife. She always takes good care of me and supports me unconditionally.

Table of the Contents

CHAPTER 1 Introduction 1

1.1 Brief review of optical sensors 2

1.2 Objectives of thesis 4

1.3 Outline 5

Reference 6

CHAPTER 2 Basic theory and analysis of waveguides and ring cavity resonance 9

2.1 Simulation methods 10

2.1.1 FDM method 10

2.1.2 BPM method 13

2.1.3 FDTD method 14

2.2 Sensitivity analysis 16

2.3 Working principle and analysis tools of ring resonator 19

2.3.1 Basic structure 19

2.3.2 Resonance equation 20

2.3.3 Radius-wavelength dispersion equation 21

2.3.4 Free spectral range (FSR) 22

2.3.5 Finesse and quality factor (Q factor) 23

2.4 Analytical solution of ring cavity resonance 23

2.4.1 Amplitude coupling equation 24

2.4.2 Single ring 25

2.4.3 Transfer function 25

2.5 Analysis of the operation characteristics of ring resonator 28

2.5.1 Influence of coupling coefficient 28

2.5.2 Influence of the propagation loss 30

2.5.3 Influence of the length of cavity 31

2.6 Sensor based on micro-ring resonator 33

Reference 35

CHAPITRE 3 Sensor based on cascaded laser and ring resonator 37

3.1 Basic structure and principle of the cascaded sensor 39

3.1.1 Basic structure 39

3.1.2 Working principle and transmission analysis 40

3.2 Design and simulation 42

3.2.1 Design parameters 43

3.2.2 Influence of the FSR difference 43

3.2.3 Influence of the Q factor of the cavity 45

3.3 Experimental results and discussions *45*
3.3.1 Fabrication and characterization of the FP laser 46
3.3.2 Fabrication and characterization of the ring resonator 49
3.3.3 Measurement and discussion of the cascaded device 52
3.4 Conclusion *56*
Reference: *58*
CHAPTER 4 Design and analysis of temperature compensation in waveguide sensors 61
4.1 The structure of the sensor *62*
4.1.1 Basic principle and transmission spectrum 63
4.1.2 Working principle of the device 63
4.2 Simulation results and discussion *67*
4.2.1 Components description 68
4.2.2 Simulation analysis 68
4.3 Effect of waveguide loss *71*
4.3.1 Analysis of the Q factor 72
4.3.2 Analysis of the intensity of the transmission 73
4.3.3 Analysis of the intensity of sensitivity 74
4.4 Conclusion *75*
Reference *76*
CHAPTER 5 Experimental investigation of the oxide/non-oxide interface after oxidation of AlGaAs 77
5.1 Wet oxidation of AlGaAs *78*
5.1.1 Basic principle 79
5.1.2 Volume change after wet oxidation 80
5.1.3 Pesence of Ga fraction on isotropic and stable oxidation 81
5.1.4 Influence of the aluminum content on oxidation rate 82
5.1.5 Effect of the thickness of the layer to be oxidiwed 83
5.1.6 Influence of doping 84
5.1.7 Effect of oxidation duration and temperature 84
5.1.8 Influence of layer structures 86
5.1.9 Influence of the gas flow 87
5.2 Characterization of the interfaces of oxidized samples *88*
5.2.1 Wet oxidation setup 88
5.2.2 Characterization by ellipsometry 89
5.2.3 Fabrication of mesas and observation by STEM and EDX 91
5.3 Effect of H_2 plasma treatment in wet oxidation *106*
5.3.1 Fabrication of samples 106

5.3.2 Experimental results and discussion 107
5.4 Conclusion *109*
Reference *111*
CHAPTER 6 Design, fabrication and characterization of waveguides and laser based on GaAs/AlGaAs **115**
6.1 Waveguides based on GaAs/AlGaAs material system *116*
6.1.1 Design and fabrication 116
6.1.2 Propagation loss characterization 118
6.1.3 Discussion 126
6.2 Fabrication and characterization of FP laser working on TM mode based on GaAs/GaAsP/AlGaAs *128*
6.2.1 Fabrication 129
6.2.2 Characterization 131
6.3 Conclusion *134*
Reference *135*
CHAPTER 7 Conclusion **137**
COMMUNICATIONS **141**

CHAPTER 1

Introduction

Rapid detection of chemical and biological analytes is of great interest for a variety of applications including quality controlling, disease diagnosis, biological molecule recognition, and environment monitoring.

Optical sensing can be defined as the technology of control and manipulation of photons during their propagation and interaction with the analytes and the output signal analysis to retrieve the information of the samples. The field is attracting interest globally and many stunning technologies are being developed. Regardless of the technology implemented, an optical sensor consists of one active part providing light and one passive sensing part where the interaction of light and analytes happens. Most work is focused on the study of passive parts among which micro-ring resonator based on silicon-on-insulator is especially promising and it has attracted attentions of many leading research groups. The low-cost easy-to-fabricate passive device has been demonstrated but an external source is always required which increases coupling complexity of the device and brings additional cost. In contrast, integrated sensor aims at the integration of optical source and sensing part on a single chip. With this technology, the difficulty and the cost associated with the coupling of the light into conventional passive sensors are removed. Furthermore, the integration brings advantages including compactness, large-array production, robustness, reliability and potential low cost.

1.1 Brief review of optical sensors

Nowadays, several representative chemical and biological sensors based on a variety of techniques including fiber-optic, planer waveguide, and high quality factor (Q factor) structures have drawn world-wide attention and been intensely developed.

Besides telecommunication applications, optical fiber is used recently in the fields of information sensing due to the merits of low cost, high reliability, flexibility, remote measurement, well established fabrication process, etc.

Optical sensing components based on fibers include fiber Bragg gratings [1-4], long period fiber gratings [5, 6], Mach-Zehnder interferometers, Fiber Fabry-Pérot interferometers [7-9], surface plasmon resonance devices [10, 11], photonic crystal fiber [12-14], etc.

Fiber Bragg grating is one of the basic optical fiber components that have a variety of applications. In this structure, the refractive index in the propagation direction has a periodic distribution. The period of refractive index perturbation is a function of resonance wavelength and effective index of the mode. The change of effective index of the mode induced by the change of refractive index of the sample surrounding the fiber shifts the Bragg wavelength. The detection limit in the order of 10^{-5} RIU (refractive index unit) has been reported on single mode fiber Bragg grating sensor [3].

However, fiber Bragg grating sensor is intrinsically insensitive to the external refractive index change because it is not directly exposed to the surrounding medium. Despite the issue can be alleviated by thinning or etching of the fiber cladding after the fabrication of fiber Bragg grating [1, 3], the mechanical strength and durability of the sensor are greatly degraded.

The development of photonic crystal fibers was a breakthrough in fiber optic technology. This technology provides unprecedented properties and can overcome many limitations intrinsic to standard optical fibers.

The geometry of photonic crystal is characterized by a periodic distribution of air holes running along the fiber, centered on a solid or hollow core. By carefully choosing the parameters, such as the lattice pitch and air-hole diameter, a large proportion of the optical field propagates through the fiber as an evanescent field. The samples to be measured in the air holes have an effective overlap with the optical field without removing the cladding of the fiber which allows for good mechanical strength and durability of the sensor. In contrast with conventional optical fibers, photonic crystal fibers offer higher sensitivity and larger design flexibility. The detection limit in the order of 4.6×10^{-7} RIU has been reported based on a directional coupler built with photonic crystal fibers [12].

Another approach to enhance the interaction of the optical mode of the fiber and the surrounding material is to reduce the size of the fiber core so that more power is transmitted outside the tiny core. The microfiber is reported [15] and implemented in the sensing field [16]. A detection limit in the order of 10^{-5} RIU has been achieved based on microfiber loops [16].

Unlike the approach based on optical fibers, sensors based on planar waveguides are miniaturized and offer potential high-density array integration which is suitable for lab-on-a-chip applications.

Different material systems for planar waveguides have been explored including SiO_2 [17], Si_3N_4 [18], polymer [19], etc. In order to improve the sensitivity, the evanescent field near the interface needs to be enhanced. The waveguides based on silicon-on-insulator material has drawn more attention in recent years [20, 21] for the ultrahigh refractive index contrast and the sensitivity [22].

The planar waveguides are suitable for a variety of sensing schemes such as Mach-Zehnder interferometer [23-25], surface plasmon resonance devices [26-28], and micro-ring resonator [29-33]. Compared with Mach-Zehnder interferometer and surface plasmon resonance devices, micro-ring resonator can build high-density array of integrated sensors with ultra-small foot-prints by advanced silicon-on-insulator waveguide technology. Furthermore, two micro-ring resonators can be combined relying on the Vernier effect which gives high-precision measurement using a relative shift in the resonant wavelengths of the two rings [34-36]. A detection limit in the order of 10^{-6} RIU has been achieved [34] based on cascaded micro-ring resonators using wavelength interrogation and the order of 10^{-7} RIU is feasible by using intensity interrogation [36].

Wavelength interrogation and intensity interrogation are two approaches to deduce the refractive index change of the surrounding analyte, relying on monitoring the transmission wavelength shift or output power variation. For a sensor system based on wavelength interrogation method, a high-end tunable laser with a photodetector or a combination of a broadband light source and a high-resolution optical spectrum analyzer is required to accurately measure the output spectrum of the optical sensor. As opposed to wavelength interrogation, the intensity interrogation scheme significantly reduced the cost of the

sensing devices by just using broadband source and photodetector [36]. However, the drawback of this approach is that the low spectral power density of the broadband source results in a low output power especially when the resonant peaks are sharp in high-sensitivity sensors. Further, the intensity interrogation using broad band source requires a large ring size and small free spectrum range to enhance output power, which restricts the flexibility of design.

1.2 Objectives of the thesis

Most of the works reported in the literatures use a passive interferometer such as a Mach-Zehnder interferometer, Fabry-Perot cavity, or a ring resonator based on silicon-on-insulator or silica platform as the sensing device. An external light source is used in this case, which leads to additional complexities in optical coupling and packaging.

The goal of the thesis is to realize ultra-compact, potentially low-cost, high-sensitivity and integrated optical sensor which could be achieved in two directions—hybrid integration or monolithic integration.

Hybrid integration of III-V laser source with silicon-on-insulator waveguide has been investigated by many groups offering a bridge to make use of the advantages of both platforms. As opposed to hybrid integration, monolithic integration is developed to build the active part and passive part of the sensor on one single chip. Monolithic integration is obviously more robust and reliable and spares the alignment cost but it comes along with other challenges at the same time. In this thesis, we explored in both directions.

An optical biosensor based on the cascade of a Fabry-Perot cavity laser and a micro-ring resonator is first investigated to improve the sensitivity by using Fabry-Perot cavity laser with higher spectral power density rather than broadband source. The ring and the laser were planned to be fabricated separately and connected by an optical fiber to demonstrate its principle and potential for low-cost practical applications.

It should be noted that although discrete Fabry-Perot cavity laser is used in the proof-of-principle experiment, it can be replaced by a heterogeneously integrated ring or Fabry-Perot cavity laser with the cavity length more accurately defined by photolithography. Compared to all-passive cascaded double-ring sensor, the integration of a laser on the sensor chip will eliminate the need for an external light source and fiber coupling. By using a 1xN splitter integrated with N ring resonators, the Fabry-Perot cavity laser can be shared by a large array of ring sensors for parallel processing.

A design based on Fabry-Perot cavity laser and two ring resonators will also be investigated. In this scheme, a reference ring is added to eliminate the influence of environmental temperature fluctuation and the wavelength drift of the laser. Based on intensity interrogation scheme with power measurements using three integrated photodetectors, the approach is suitable for low-cost, large-array, fully integrated sensors with compensation for the temperature instability and the laser wavelength drift. The simulation and analysis are performed on silicon-on-insulator material system but the concept can be easily transplanted to other substrates.

GaAs material system is ideal for laser diode which makes it a potential candidate for integrated sensor. In addition, by wet oxidation, low index native oxide can be fabricated to form high index contrast passive waveguide suitable for high-sensitivity sensing. With the goal of making monolithically integrated sensor, we are going to explore the GaAs waveguide fabricated by wet oxidation and the TM mode laser based on tensile strained quantum wells given that TM mode allows higher sensitivity than TE mode.

1.3 Outline

After the introduction which constitutes the chapter one, the manuscript is organized as follows:

In chapter two, the simulation and analysis tools for the design of optical waveguide and micro-ring resonator are given. Several fundamental methods are introduced and basic analysis is performed.

In chapter three, a highly-sensitive integrated optical sensor based on the cascade of a Fabry-Perot cavity laser and a micro-ring resonator is investigated. The basic structure and working principle were introduced in the first section. The design and fabrication of Fabry-Perot cavity laser and micro-ring resonator were described. Then the experimental results of the cascaded sensor were shown at the end of the chapter, demonstrating its principle and potential for low-cost practical applications.

In chapter four, a fully integrated sensor based on micro-ring resonator and easy-to-fabricate Fabry-Perot cavity laser or single-mode laser is illustrated. We mainly investigated the compensation method of the fluctuation of environmental temperature and the wavelength drift of laser diode by simple intensity detection from three photodetectors. In the end, the effect of optical loss in the waveguide is analysed for sensing applications.

In chapter five, we turn to GaAs platform seeking for the monolithic integration. As an essential technology to form high index contrast, the mechanism of wet oxidation of AlGaAs has been experimentally investigated. We show detailed information of the interface of oxide/non-oxide by scanning transmission electron microscopy because of its key role in optical loss of waveguide. The oxidation caused by neighboring oxide of high Al content layer is illustrated. A superlattice structure is proposed and it shows higher resistance to the oxidation across the interface compared with bulk AlGaAs, even with bulk GaAs. In the last section, we investigated the effect of hydrogen plasma in wet oxidation.

In chapter six, we present the results on optical waveguide with buried oxide layer and laser diode working on TM mode. At first the measurements of the propagation loss of the waveguide by Fabry-Perot method are shown at 1550nm and 830nm. Then we describe the fabrication process and the characterization results of the TM mode FP laser based on tensile-strained quantum wells providing a building block for future monolithic integration.

The conclusion is addressed in the final chapter.

Reference

[1] A. Iadicicco, S. Campopiano, A. Cutolo, M. Giordano, and A. Cusano, "Nonuniform thinned fiber bragg gratings for simultaneous refractive index and temperature measurements," IEEE Photon. Technol. Lett., 17, 1495-1497, 2005.

[2] P. Lu and Q. Chen, "Fiber Bragg grating sensor for simultaneous measurement of flow rate and direction," Meas. Sci. Technol., 19, 125302-125309, 2008.

[3] W. Liang, Y. Huang, Y. Xu, R.K. Lee, A. Yariv, "Highly sensitive fiber Bragg grating refractive index sensors," Appl. Phys. Lett., 86 , 151122-151122-3, 2005.

[4] X. Fang, C. R. Liao, and D. N. Wang, "Femtosecond laser fabricated fiber Bragg grating in microfiber for refractive index sensing," Opt. Lett., 35 ,1007-1009, 2010.

[5] A. P. Zhang, L. Y. Shao, J. F. Ding, and S. He, "Sandwiched long-period gratings for simultaneous measurement of refractive index and temperature," IEEE Photon. Technol. Lett., 17, 2397-2399, 2005.

[6] P. L. Swart, "Long-period grating Michelson refractometric sensor," Meas. Sci. Technol., 15, 1576-1580, 2004.

[7] Y. J. Rao, "Recent progress in fiber optic extrinsic Fabry-Perot interferometric sensors," Opt. Fiber Technol., 12, 227-237, 2006.

[8] Z. L. Ran, Y. J. Rao, W. J. Liu, X. Liao, and K. S. Chiang, "Laser-micromachined Fabry-Perot optical fiber tip sensor for high-resolution temperature-independent measurement of refractive index," Opt. Express, 16, 2252-2263, 2008.

[9] L. Li, L. Xia, Z. Xie, and D. Liu, "All-fiber Mach-Zehnder interferometers for sensing applications," Opt. Express, 20, 11109-11120, 2012.

[10] K. Kurihara, H. Ohkawa, Y. Iwasaki, O. Niwa, T. Tobita, K. Suzuki, "Fiber-optic conical microsensors for surface plasmon resonance using chemically etched single-mode fiber," Anal. Chim. Acta., 523, 165-170, 2004.

[11] R. Micheletto, "Modeling and test of fiber-optics fast SPR sensor for biological investigation," Sens. Actuators A, 119, 283-290, 2005.

[12] Darran K. C. Wu, Boris T. Kuhlmey, and Benjamin J. Eggleton, "Ultrasensitive photonic crystal fiber refractive index sensor," Opt. Lett., 34, 322-324, 2009.

[13] B. J. Eggleton, C. Kerbage, P. S. Westbrook, R. S. Windeler, and A. Hale, "Microstructured ptical fiber devices," Opt. Express, 9, 698 -713, 2001.

[14] L. Rindorf and O. Bang, "Highly sensitive refractometer with a photonic-crystal-fiber long-period grating," Opt. Lett., 33, 563-565, 2008.

[15] L. Tong, R.R. Gattass, J.B. Ashcom, S. He, J. Lou, M. Shen, I. Maxwell, E. Mazur, "Subwavelength-diameter silica wires for low-loss optical wave guiding," Nature, 426, 816-819, 2003.

[16] X. Guo and L. M. Tong, "Supported microfiber loops for optical sensing," Opt. Express, 16 , 14429-14434, 2008.

[17] B.J. Luff J.S. Wilkinson, J. Piehler, U. Hollenback, J. Ingenhoff and N. Fabricius, "Integrated optical Mach-Zehnder biosensor," J. Lightwave Technol., 16, 583-591 , 1998.

[18] F. Prieto, B. Sepulveda, A. Calle, A Llobera, C. Dominguez, A. Abad, A. Montoya and L.M. Lechuga, "An integrated optical interferometric nanodevice based on silicon technology for biosensor applications," Nanotechnology, 14, 907-912, 2003.

[19] C. Chao and L.J. Guo, "Biochemical sensors based on polymer microrings with sharp asymmetrical resonance," Applied Phys. Lett., 83, 1527-1529, 2003.

[20] D. X. Xu, A. Densmore, A. Delâge, P. Waldron, R. McKinnon, S. Janz, J. Lapointe, G. Lopinski, T. Mischki, E. Post, P. Cheben, and J. H. Schmid, "Folded cavity SOI microring sensors for high sensitivity and real time measurement of biomolecular binding," Opt. Express, 16, 15137-15148, 2008.

[21] A. Densmore, M. Vachon, D.-X. Xu, S. Janz, R. Ma, Y.-H. Li, G. Lopinski, A. Delâge,J. Lapointe, C. C. Luebbert, Q. Y. Liu, P. Cheben, and J. H. Schmid, "Silicon photonic wire biosensor array for multiplexed real-time and label-free molecular detection," Opt. Lett., 34, 3598-3600, 2009.

[22] A. Densmore, D.-X. Xu, P. Waldron, S. Janz, P. Cheben, J. Lapointe, A. Delâge, B. Lamontagne, J. H. Schmid, and E. Post, "A silicon-on-insulator photonic wire based evanescent field sensor," IEEE Photon. Technol. Lett., 18, 2520-2522, 2006.

[23] F. Prieto, B. Sepúlveda, A. Calle, A. Llobera, C. Domínguez, A. Abad, A. Montoya, and L. M. Lechuga, "An integrated optical interferometric nanodevice based on silicon technology for biosensor applications," Nanotechnology, 14, 907-912, 2003.

[24] B. J. Lu, J. S. Wilkinson, J. Piehler, U. Hollenbach, J. Ingen-ho, and N. Fabricius, "Integrated optical Mach-Zehnder biosensor," J. Lightwave Technol., 16, 583-592, 1998.

[25] R. G. Heideman, P. V. Lambeck, "Remote opto-chemical sensing with extreme sensitivity: design, fabrication and performance of a pigtailed integrated optical phase-modulated Mach-Zehnder interferometer system," Sens. Actuators B: Chemical, 61, 100-127, 1999.

[26] R.D. Harris, J.S.Wilkinson, "Waveguide surface plasmon resonance sensors," Sens. Actuators B, 29, 261-267, 1995.

[27] R. Levy , S. Ruschin, "SPR waveguide sensor based on transition of modes at abrupt discontinuity," Sens. Actuators B, 124, 459-465, 2007.

[28] R. Levy, A. Peled, S. Ruschin, "Waveguided SPR sensor using a Mach-Zehnder interferometer with variable power splitting ratio," Sens. Actuators B: Chem., 119, 20-26, 2006.

[29] P. Dumon, W. bogaerts, V. Wiaux, J. Wouters, S. beckx, J. V. Campenhout, D. Taillaert, B. Luyssaert, P. Bienstman, D. V. Thourhout, and R. Baets, "Low-loss SOI photonic wires and ring resonators fabricated with deep UV lithography," IEEE Photon. Technol. Lett., 16, 1328-1330, 2004.

[30] S.-Y. Cho and N. M. Jokerst, "A polymer microdisk photonic sensor integrated onto silicon," IEEE Photon. Technol. Lett., 18, 2096-2098, 2006.

[31] M. Armani, R. P. Kulkarni, S. E. Fraser, R. C. Flagan, and K. J. Vahala, "Label-free, single-molecule detection with optical microcavities," Science, 317, 783-787, 2007.

[32] K. De Vos, I. Bartolozzi, E. Schacht, P. Bienstmanl, and R. Baets, "Silicon-on-Insulator microring resonator for sensitive and label-free biosensing," Opt. Express, 15, 7610-7615, 2007.

[33] D.-X. Xu, A. Densmore, A. Del˙age, P. Waldron, R. McKinnon, S. Janz, J. Lapointeki, G. Lopinski, T. Mischki, E. Post, P. Cheben, and J. H. Schmid, "Folded cavity SOI microring sensors for high sensitivity and real time measurement of biomolecular binding," Opt. Express, 16 , 15137-15148, 2008.

[34] T. Claes, V. Bogaerts and P. Bienstman, "Experimental characterization of a silicon photonic biosensor consisting of two cascaded ring resonators based on the Vernier-effect and introduction of a curve fitting method for an improved detection limit," Opt. Express, 18, 22747-22761, 2010.

[35] L. Jin, M. Li, and J.-J. He, "Highly-sensitive silicon-on-insulator sensor based on two cascaded micro-ring resonators with vernier effect", Opt. Commun, 284, 156-159, 2011.

[36] L. Jin, M. Li, and J.-J. He, "Optical waveguide double-ring sensor using intensity interrogation with a low-cost broadband source," Opt. Lett., 36, 1128-1130, 2011.

CHAPTER 2

Basic theory and analysis of waveguides and ring cavity resonance

Waveguide is the most basic component and the analysis of waveguide is the first step for the design of the devices. The simulation and analysis tools for the design of optical waveguides are shown in this chapter. Several powerful methods are briefly introduced and basic analyses are performed.

Micro-ring resonator is the main building block of the passive part of the sensor in our project. The relevant theories and analysis are introduced in this chapter. First of all, basic working principles and main parameters are illustrated. Then the analytical solution and the influence of several key parameters to the performance of the ring resonator are studied and analyzed.

2.1 Simulation methods

The fundamental theory behind all photonic devices can be described by the well-known Maxwell's equations which are widely used for calculating and analyzing the behavior of electromagnetic fields. However, analytical solutions of the Maxwell's equations cannot be derived for most applications except for some simple structures. In order to analyze the realistic photonic components with sophisticated geometry structures, numerical methods are developed to simulate and predict the behavior of lightwave.

In this section, several numerical methods are introduced for the design of photonic devices. The mode characteristic of optical waveguides can be analyzed by finite difference method (FDM) [1] and finite element method (FEM) [2]. Beam propagation method (BPM) and finite-difference time-domain (FDTD) are widely used to simulate the light propagation in optical components.

2.1.1 FDM method

Optical waveguides are the most fundamental building block of integrated optical devices, and the mode analysis of the waveguides is therefore the first step for all further analysis. A variety of numerical methods have been developed for this purpose including the boundary element method (BEM) [3], method of moments (MoM) [4], BPM [5], FEM [2], and FDM [1].

The full-vector wave equation can be written from Maxwell's equations as

$$\begin{pmatrix} P_{xx} & P_{xy} \\ P_{yx} & P_{yy} \end{pmatrix} \begin{pmatrix} E_x \\ E_y \end{pmatrix} = \beta^2 \begin{pmatrix} E_x \\ E_y \end{pmatrix} \tag{2.1}$$

E_x and E_y are the electric fields, β is the propagation constant of the mode. P_{xx}, P_{xy}, P_{yx} and P_{yy} can be expressed as

$$P_{xx}E_x = \frac{\partial}{\partial x}\left[\frac{1}{n^2}\frac{\partial\left(n^2E_x\right)}{\partial x}\right] + \frac{\partial^2 E_x}{\partial y^2} + n^2k^2E_x \tag{2.2.a}$$

$$P_{yy}E_y = \frac{\partial^2 E_y}{\partial x^2} + \frac{\partial}{\partial y}\left[\frac{1}{n^2}\frac{\partial\left(n^2E_y\right)}{\partial y}\right] + n^2k^2E_y \tag{2.2.b}$$

$$P_{xy}E_y = \frac{\partial}{\partial x}\left[\frac{1}{n^2}\frac{\partial\left(n^2E_y\right)}{\partial y}\right] - \frac{\partial^2 E_y}{\partial x\partial y} \tag{2.2.c}$$

$$P_{yx}E_x = \frac{\partial}{\partial y}\left[\frac{1}{n^2}\frac{\partial\left(n^2E_x\right)}{\partial x}\right] - \frac{\partial^2 E_x}{\partial y\partial x} \tag{2.2.d}$$

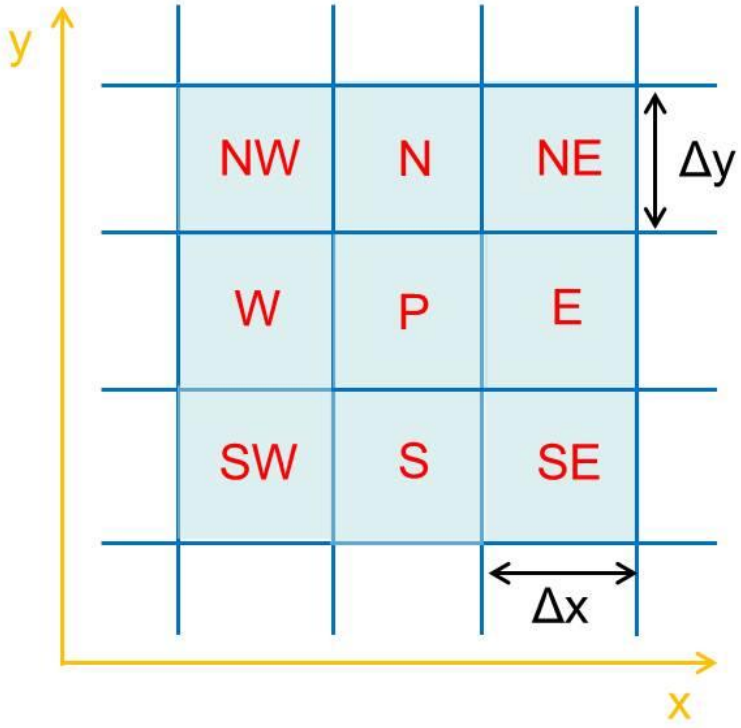

Fig. 2.1 Two-dimensional FDM grid.

The discretization of refractive index distribution in the cross section of the waveguide is shown in Fig. 2.1. P is the target grid and the grids around P are denoted as NW, N, NE, W, E, SW, S, and SE. Here W, E, N, and S represent west, east, north and south, respectively. The differential form of P_{xx}, P_{xy}, P_{yx}, P_{yy} can be derived as follows.

First, the differential form of P_{xx} can be written as

$$P_{xx}:\begin{matrix} 0 & \dfrac{1}{(\Delta y)^2} & 0 \\ \dfrac{a_W}{(\Delta x)^2} & n_P^2k^2-\dfrac{2}{(\Delta y)^2}-\dfrac{2a_P}{(\Delta x)^2} & \dfrac{a_E}{(\Delta x)^2} \\ 0 & \dfrac{1}{(\Delta y)^2} & 0 \end{matrix} \tag{2.3}$$

where a_W, a_P and a_E are dimensionless coefficients defined as

$$\begin{cases} a_W = \dfrac{4\left(n_W^2n_P^2+n_E^2n_W^2\right)}{n_P^4+2n_E^2n_P^2+2n_W^2n_P^2+3n_E^2n_W^2} \\ a_P = \dfrac{2\left(2n_P^4+n_E^2n_P^2+n_P^2n_W^2\right)}{n_P^4+2n_E^2n_P^2+2n_W^2n_P^2+3n_E^2n_W^2} \\ a_E = \dfrac{4\left(n_E^2n_P^2+n_E^2n_W^2\right)}{n_P^4+2n_E^2n_P^2+2n_W^2n_P^2+3n_E^2n_W^2} \end{cases} \tag{2.4}$$

The differential form of P_{yx} is written as

$$P_{yx}:\begin{matrix} \dfrac{1\text{-}a_{NW}}{4\Delta x\Delta y} & \dfrac{3\left(a_{NE}-a_{NW}\right)}{4\Delta x\Delta y} & \dfrac{a_{NE}-1}{4\Delta x\Delta y} \\ 0 & 0 & 0 \\ \dfrac{a_{SW}-1}{4\Delta x\Delta y} & \dfrac{3\left(a_{SW}-a_{SE}\right)}{4\Delta x\Delta y} & \dfrac{1\text{-}a_{SE}}{4\Delta x\Delta y} \end{matrix} \tag{2.5}$$

where the dimensionless coefficients are

$$\begin{cases} \alpha_{NE} = \dfrac{2\left(n_{NE}^2n_N^2+3n_{NE}^2n_{NW}^2\right)}{n_N^4+2n_{NE}^2n_N^2+2n_{NW}^2n_N^2+3n_{NE}^2n_{NW}^2} \\ \alpha_{NW} = \dfrac{2\left(n_{NW}^2n_N^2+3n_{NE}^2n_{NW}^2\right)}{n_N^4+2n_{NE}^2n_N^2+2n_{NW}^2n_N^2+3n_{NE}^2n_{NW}^2} \\ \alpha_{SE} = \dfrac{2\left(n_{SE}^2n_S^2+3n_{SE}^2n_{SW}^2\right)}{n_S^4+2n_{SE}^2n_S^2+2n_{SW}^2n_S^2+3n_{SE}^2n_{SW}^2} \\ \alpha_{SW} = \dfrac{2\left(n_{SW}^2n_S^2+3n_{SE}^2n_{SW}^2\right)}{n_S^4+2n_{SE}^2n_S^2+2n_{SW}^2n_S^2+3n_{SE}^2n_{SW}^2} \end{cases} \tag{2.6}$$

Similarly, the differential form of P_{xy} and P_{yy} can also be derived.

With Eq. (2.3)-Eq. (2.6), we can discretize Eq. (2.1) to an eigenvalue problem. This eigenvalue equation determines the optical mode of the waveguide. Propagation constant β is the eigenvalue and E_x, E_y are the corresponding eigen functions.

2.1.2 BPM method

FDM is no longer applicable for propagation of lightwave along the waveguide with variant index distribution in the propagation direction, e.g. splitters, couplers and multimode interference (MMI) structures. BPM is developed to deal with this kind of problems [6]. This approach is widely used for simulation of a variety of photonics components because of its simplicity and relatively high accuracy.

Many different kinds of BPMs have been developed and reported in the literature including finite difference (FD) BPM [6], fast Fourier transforms (FFT) BPM [7], and finite element method (FEM) BPM [8]. It should be noted that conventional BPM is only effective for paraxial analysis without index discontinuity in the propagation direction and scalar BPM can only be applied to weak confinement waveguides. Furthermore, this method is not good at dealing with reflections. In order to improve BPM for more complex applications, several efforts have been made such as wide-angle BPM [9], bidirectional BPM [10] and semi/full-vectorial BPM [11] which make it possible to analyze and simulate very complex optical components. Here we introduce the basic two-dimensional BPM model.

The scalar field assumption allows the wave equation to be written in the form of the well-known Helmholtz equation as

$$\frac{\partial^2 \phi}{\partial x^2} + \frac{\partial^2 \phi}{\partial z^2} + [k(x,z)]^2 \phi = 0 \tag{2.7}$$

where $k(x,z) = k_0 n(x,z)$, k_0 is the wavenumber in free space, and $n(x,z)$ is the refractive index distribution.

Considering that in typical guided-wave problems the most rapid variation in the field ϕ is the phase variation in the propagation direction. A so-called slowly varying field *u(x, z)* can be defined as follows

$$\phi(x,z) = u(x,z) e^{i\bar{k}z} \tag{2.8}$$

Here $\bar{k}$ is a constant number to represent the average phase variation of the field ϕ, and is referred as the reference wavenumber. The reference wavenumber is frequently expressed in terms of a reference refractive index, $\bar{n}$, via $\bar{k} = k_0 \bar{n}$. Introducing the above expression into the Helmholtz equation yields the following equation for the slowly varying field

$$\frac{\partial^2 u}{\partial z^2} + 2i\bar{k}\frac{\partial u}{\partial z} + \frac{\partial^2 u}{\partial x^2} + (k^2 - \bar{k}^2)u = 0 \tag{2.9}$$

At this point the above equation is completely equivalent to the exact Helmholtz equation, except that it is expressed in terms of *u*. It is now assumed that the variation of *u* with *z* is sufficiently slow so that the first term above can be neglected with respect to the second. This is the familiar slowly varying envelope approximation and in this context it is also referred to as the paraxial approximation. With this assumption and after slight rearrangement, the above equation reduces to

$$\frac{\partial u}{\partial z} = \frac{i}{2\bar{k}}\left(\frac{\partial^2 u}{\partial x^2} + (k^2 - \bar{k}^2)u\right) \tag{2.10}$$

The numerical results can be achieved by FD method and discretization.

2.1.3 FDTD method

FDTD method [12, 13] is a popular numerical simulation technique without any approximation which was first reported by Yee [14]. This method provides rigorous solution to the Maxwell's Equations which permits high accuracy of the simulation results. FDTD method became the ideal approach to deal with the interaction between the electromagnetic field and the material system. In spite of the extensive consumption of large computing resources, FDTD is intuitive to understand and easy to use. Here, we take an isotropic and nondispersive material system as an example which provides

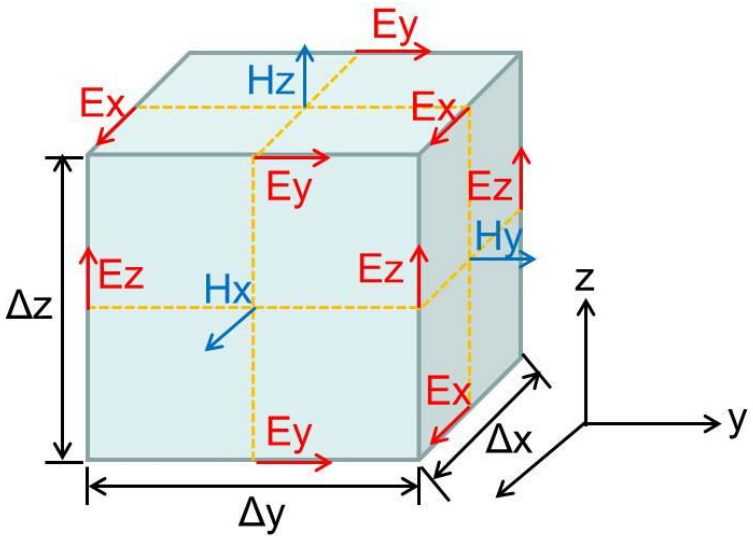

Fig. 2.2 Yee's Grid

$$\begin{cases} \vec{D} = \varepsilon \vec{E} \\ \vec{B} = \mu \vec{H} \\ \vec{J}_e = \sigma \vec{E} \\ \vec{J}_m = \sigma^* \vec{H} \end{cases} \tag{2.11}$$

where ε, μ is the permittivity and the permeability, and σ, σ^* is the electric conductivity and the magnetic conductivity, respectively. By Eq. (2.11), we can rewrite the Maxwell's equations as

$$\Delta \times \vec{E} = -\mu \frac{\partial \vec{H}}{\partial t} - \sigma^* \vec{H} \tag{2.12.a}$$

$$\Delta \times \vec{H} = \varepsilon \frac{\partial \vec{E}}{\partial t} + \sigma \vec{E} \tag{2.12.b}$$

These equations can be extended to six scalar equations which can be solved numerically with the FDTD method. Eq. (2.12) is first discretized according to Yee's mesh [14], as shown in Fig. 2.2. All *E* and *H* field components in the grids are cross-linked to each other with a half of the step ($\Delta x/2$, $\Delta y/2$ and $\Delta z/2$). At any point, the updated value of the *E*-field in time is dependent on the stored value of the *E*-field and the change of *H*-field and vice versa. They are also shifted with half of the step in the time domain. The magnetic field vector components are solved at a given instant with the electric field vector components solved half of the time step later. The discretization forms of Eq. (2.12) are given as

$$\vec{H}^{m+\frac{1}{2}} = \left(\frac{1 - \frac{\sigma^* \Delta t}{2\mu}}{1 + \frac{\sigma^* \Delta t}{2\mu}} \right) \bullet \vec{H}^{m-\frac{1}{2}} - \left(\frac{\frac{\Delta t}{\mu}}{1 + \frac{\sigma^* \Delta t}{2\mu}} \right) \nabla \times \vec{E}^m \tag{2.13.a}$$

$$\vec{E}^{m+1} = \left(\frac{1 - \frac{\sigma^* \Delta t}{2\mu}}{1 + \frac{\sigma^* \Delta t}{2\mu}} \right) \bullet \vec{E}^{m+1} - \left(\frac{\frac{\Delta t}{\mu}}{1 + \frac{\sigma^* \Delta t}{2\mu}} \right) \nabla \times \vec{H}^{m+\frac{1}{2}} \tag{2.13.b}$$

where m is the time index. The formulas Eq. (2.13) can be easily implemented with the central difference form. It should be pointed out that in order to obtain a stable and convergent solution, the time step Δt cannot be too large. It should fulfill the following condition

$$c\Delta t < \frac{1}{\sqrt{\frac{1}{\Delta x^2} + \frac{1}{\Delta y^2} + \frac{1}{\Delta z^2}}} \tag{2.14}$$

where c is the light speed in the material. A light excitation can be placed inside the computation region. The calculation results of every step are stored for the next time step and the E and H fields are resolved iteratively. As mentioned before, FDTD method requires a lot of computing resources especially in the case of 3D-FDTD. It is therefore applicable only to a structure with a limited size.

2.2 Sensitivity analysis

Most integrated sensors are based on the principal of evanescent field (EF). The evanescent tail of optical waveguide interacts with the surrounding materials resulting in change of effective index of waveguide mode. These devices provide a promising approach for the label-free and real-time detection of biological molecules or chemical solutions. Waveguide sensors built on semiconductor materials can have small footprint, suitable to be integrated into compact arrays and attractive for "lab-on-a-chip" development.

As shown in Fig. 2.3, when the light propagates in the waveguide, the power of the mode partially extends into the cladding layer which can interact with the material of cladding in a small depth. The evanescent field can be written as

$$E = E_0 \exp(-\delta / d_p) \tag{2.15}$$

where δ is the distance from the interface, d_p is the penetration depth where the field amplitude decays to 1/e of that at the interface.

There are two sensing types based on the samples: homogeneous sensing and surface sensing as shown in Fig. 2.3. In the case of homogeneous sensing, the samples are homogeneous solutions with uniform refractive index which affects the effective index of the waveguide. As for surface sensing, the samples are thin layers attached to the interface resulting in effective refractive index change.

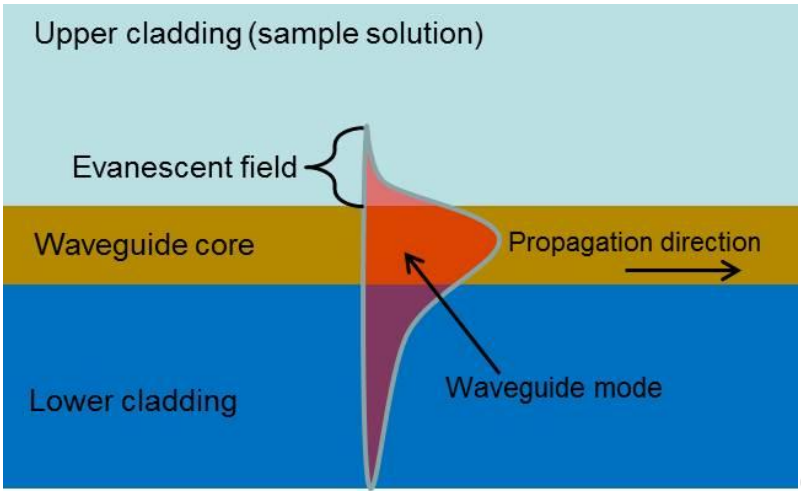

(a)

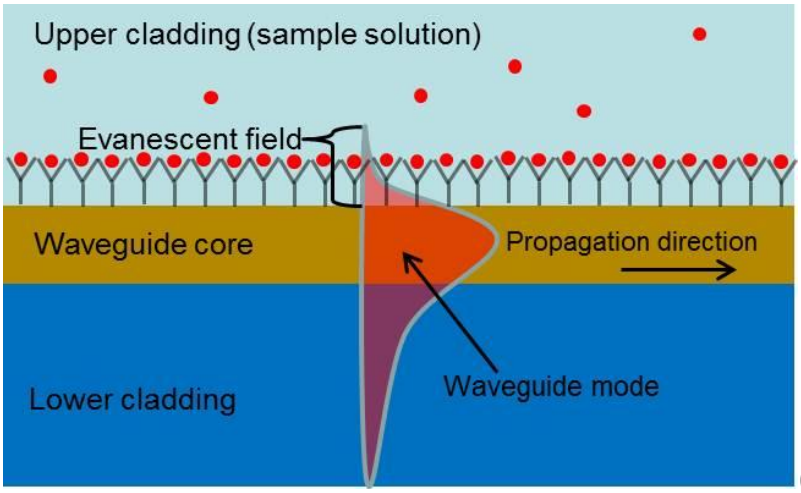

(b)

Fig. 2.3 Schematic of sensing based on evanescent field. (a) homogeneous sensing (b) surface sensing.

The waveguide sensitivity of EF sensors is defined as the ratio of effective index change of the waveguide mode over ambient refractive index change (homogeneous sensing) or variation of thickness of an adsorbed molecular layer (surface sensing). In this thesis, we focus on homogeneous sensing and the waveguide sensitivity in this case is given as

$$S_{WG} = \frac{dn_{eff}}{dn_c} \tag{2.16}$$

The waveguide sensitivity is determined by the waveguide structure, including the core thickness and the refractive index contrast between the core and the cladding. It also depends on the polarization mode. For SOI waveguide with a thin core layer and a large refractive index contrast, the TM polarization mode provides higher maximum sensitivity [15].

As shown in Fig. 2.4, the sensitivity (homogeneous sensing) of SOI planar waveguides depends on the thickness of the core layer. The refractive index of Si and SiO_2 is 3.48 and 1.444, respectively. It was assumed that the refractive index of up-cladding changes from 1.32 to 1.33, and the working wavelength is 1550 nm. The maximum sensitivity of TE mode reaches 32 % with a core thickness of 40 nm while the maximum sensitivity of TM mode stands at 47 % with a core thickness of 190 nm. The optimal core layer thickness is 220 nm for surface sensing [15].

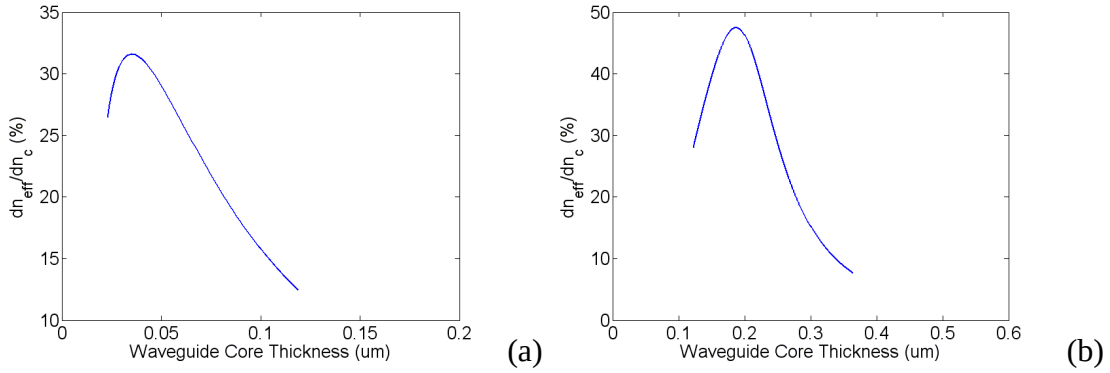

Fig. 2.4 Sensitivity versus thickness of Si core layer (a) TE mode (b) TM mode

Fig. 2.5 shows the sensitivity (homogeneous sensing) of $Al_{0.34}Ga_{0.66}As/AlO_x$ planar waveguides as a function of the thickness of the $Al_{0.34}Ga_{0.66}As$ core layer. The refractive index of $Al_{0.34}Ga_{0.66}As$ and AlO_x is 3.438 and 1.55, respectively. Assume the refractive index of the up-cladding changes from 1.32 to 1.33 and the working wavelength is 800 nm. The maximum sensitivity of TM mode reaches 38 % with a core thickness of 90 nm.

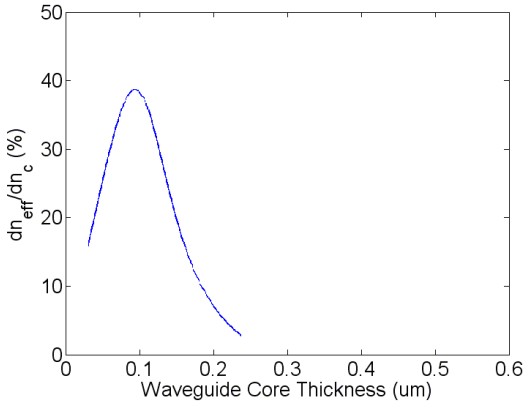

Fig. 2.5 Sensitivity versus thickness of $Al_{0.34}Ga_{0.66}As$ core layer on TM mode

Based on the above analysis, we used 450 nm×220 nm SOI waveguide as an example for theoretical analysis. The sensitivity reaches 42 % on TM mode. In experiment, easy-to-fabricate 1000 nm×50 nm ridge waveguide was used with a sensitivity of 5 % for TE mode. The TM mode on such a waveguide is leaky.

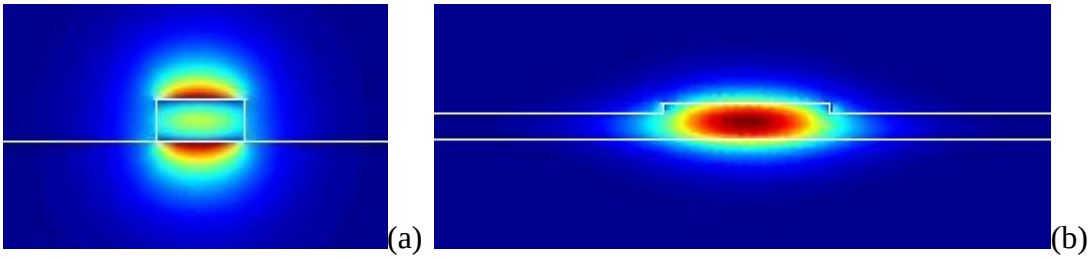

(a) (b)

Fig. 2.6 (a) 450 nm×220 nm SOI stripe waveguide on TM mode (b) SOI ridge waveguide with 220 nm core layer, width 1μm, ridge height 50 nm on TE mode.

2.3 Working principle and analysis tools of ring resonator

2.3.1 Basic structure

Ring resonator typically consists of a micro-ring cavity and input/output waveguides as shown in Fig. 2.7. The input light goes through the input port of the input waveguide. In the coupling region near the ring resonator, the gap between the waveguide and the ring is small enough for the light to couple from the waveguide to the ring. A proportion of light resonates (the direction of the light propagation is shown by the arrows in Fig. 2.7) in the ring cavity and couples out to the output waveguide in another coupling region. Finally, the output light is collected from the drop port.

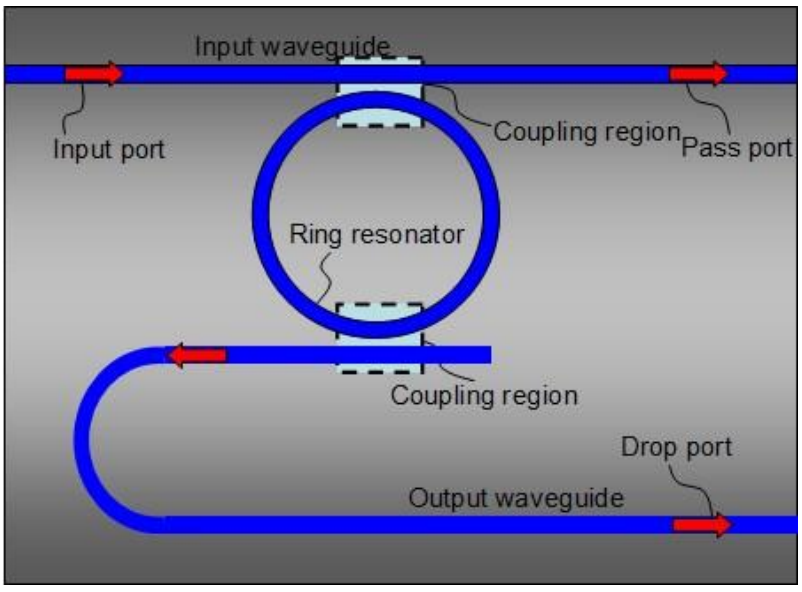

Fig. 2.7 Schematic of a passive ring resonator

An optical device such as a biosensor can comprise a single-ring resonator or multi-ring resonator. The multi-ring resonator can be constructed by coupling multiple rings in series or in parallel, as shown in Fig. 2.8 and Fig 2.9, respectively.

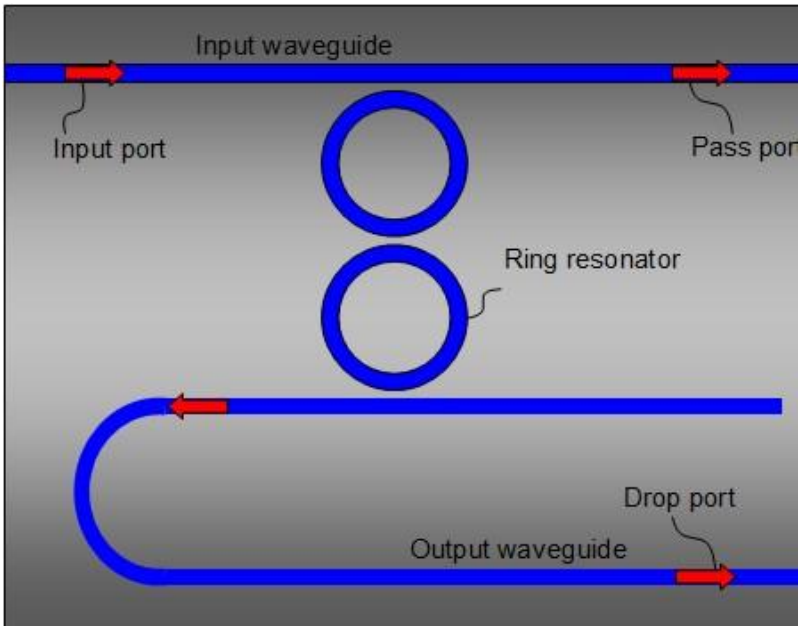

Fig. 2.8 Schematic of series multi-ring resonator

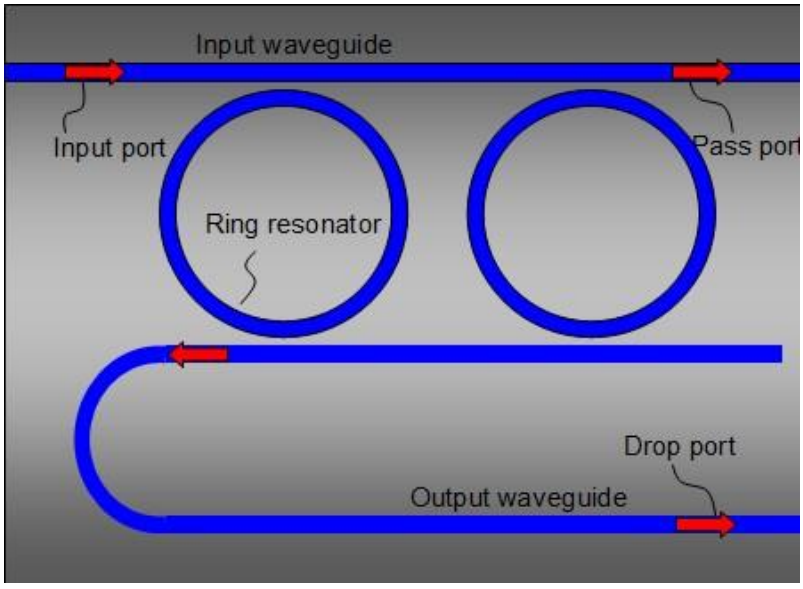

Fig. 2.9 Schematic of parallel multi-ring resonator

2.3.2 Resonance equation

If the wavelength λ satisfies the resonant condition,

$$2\pi R n_{eff} = m\lambda \tag{2.17}$$

the coupling of the light with the wavelength λ will be enhanced and all other wavelengths will be suppressed. As a result, only λ will be dropped from the drop port, while the rest of the wavelengths will pass through and output from the pass port. Here *R* is the radius of the ring, n_{eff} is the effective index of the bending waveguide, and *m* is an integer.

From Eq. (2.17), we can obtain the radius

$$R = \frac{m\lambda}{2\pi n_{eff}} \tag{2.18}$$

For a given *R*, a series of λ can satisfy this equation with a corresponding *m*. It means a series of wavelengths can resonate in the ring resonator.

2.3.3 Radius-wavelength dispersion equation

A wavelength that is enhanced by resonance in the ring cavity satisfies Eq. (2.17). However, n_{eff} of the waveguide varies with wavelength. Therefore, n_{eff} is a function of wavelength and can be described as $n_{eff} = n_{eff}(\lambda)$. The radius can be regarded as a function of *m* and *λ*, i. e., *R=R(m, λ)*. From Eq. (2.17), we can obtain

$$2\pi R \frac{dn_{eff}}{d\lambda} + 2\pi n_{eff} \frac{\partial R}{\partial \lambda} = m \tag{2.19}$$

which can be rewritten as

$$\frac{\partial R}{\partial \lambda} = \frac{m}{2\pi n_{eff}} \left(1 - \frac{2\pi R}{m} \frac{dn_{eff}}{d\lambda} \right) \tag{2.20}$$

$$\frac{\partial R}{\partial \lambda} = \frac{m}{2\pi n_{eff}^2} \left(n_{eff} - \lambda \frac{dn_{eff}}{d\lambda} \right) \tag{2.21}$$

Then we can get the radius-wavelength dispersion equation

$$\frac{\partial R}{\partial \lambda} = \frac{m n_g}{2\pi n_{eff}^2} \tag{2.22}$$

where n_g is the group effective index of the waveguide.

$$n_g = n_{eff} - \lambda \frac{dn_{eff}}{d\lambda} \tag{2.23}$$

Similarly, since *R* is also a function of *m*, we can derive from Eq. (2.18)

$$\frac{\partial R}{\partial m} = \frac{\lambda}{2\pi n_{eff}} \tag{2.24}$$

Therefore, the change of m and λ induces a change of the radius of the ring. From Eqs. (2.22) and (2.24) we can obtain the difference of *R*,

$$\Delta R = \frac{\partial R}{\partial \lambda}\Delta\lambda + \frac{\partial R}{\partial m}\Delta m = \frac{1}{2\pi n_{eff}}\left(\frac{m n_g}{n_{eff}}\Delta\lambda + \lambda\Delta m\right) \tag{2.25}$$

where △λ is the change of wavelength and △m is the change of resonance order, △m =1,2, ⋯.

2.3.4 Free spectral range (FSR)

As mentioned above, with fixed radius of ring, there are a series of wavelengths which satisfy the resonant Eq. (2.17) and can be enhanced in the ring resonator. The wavelength difference between two adjacent resonant wavelengths is called free spectral range (FSR). Assuming the corresponding order for the two resonance peaks are m and m-1, from Eq. (2.17), the wavelength is inversely proportional to the resonance order so when $\triangle\lambda_m$= FSR, △m= -1. Take the derivative of Eq. (2.17) with respect to λ, we can get

$$2\pi R\frac{dn_{eff}}{d\lambda}\Delta\lambda_m = m\Delta\lambda_m + \lambda\Delta m = m\Delta\lambda_m - \lambda \tag{2.26}$$

Then we can obtain

$$FSR = \Delta\lambda_m = \frac{\lambda}{m}\left(1 - \frac{2\pi R}{m}\frac{dn_{eff}}{d\lambda}\right)^{-1} \tag{2.27}$$

From Eq. (2.17), Eq. (2.27) can be transformed as

$$FSR = \frac{\lambda n_{eff}}{m}\left(n_{eff} - \lambda\frac{dn_{eff}}{d\lambda}\right)^{-1} \tag{2.28}$$

According to Eq. (2.23), the FSR is

$$FSR = \frac{\lambda n_{eff}}{m n_g} = \frac{\lambda^2}{2\pi R n_g} \tag{2.29}$$

Since the FSR is inversely proportional to the size of the ring resonator, the ring must be small in order to achieve a large FSR. If the radius of the ring is too large, the FSR could be too narrow to achieve good filtering effect. Therefore, a small ring is required for

filtering. But the bending loss will increase with decreasing ring size. For typical waveguide based on SiO_2, the bending loss becomes too large when the ring radius is less than tens of microns. A method to solve this problem is to increase the refractive index contrast between the waveguide core and the cladding. Waveguide based on SOI or AlGaAs/AlOx can achieve small ring with a radius less than 5 μm which allows for high flexibility of design.

2.3.5 Finesse and quality factor

The finesse and quality factor (Q factor) are two key characteristics of the ring resonator which are used to evaluate the quality of the resonator and they are defined as

$$F = \frac{FSR}{\Delta\lambda_{FWHM}} = \frac{\pi t \exp(-\pi R\alpha_R)}{1-t^2 \exp(-2\pi R\alpha_R)} \tag{2.30}$$

$$Q = \frac{\lambda}{\Delta\lambda_{FWHM}} = \frac{2\pi R n_g}{\lambda} F \tag{2.31}$$

$$\Delta\lambda_{FWHM} \approx \frac{FSR}{\pi}\left(\frac{\exp(\pi R\alpha_R)}{t - t\exp(-\pi R\alpha_R)}\right) \tag{2.32}$$

$\Delta\lambda_{FWHM}$ is full width at half maximum (FWHM) at resonance wavelength. Normally, a larger Q or F means the resonator is of good quality for filtering and the resonance peaks are sharper.

2.4 Analytical solution of ring cavity resonance

The transfer matrix method is an effective method to analyze transmission of micro-ring resonator. A matrix can be used to represent the coupling region and another matrix to represent the phase difference and amplitude decay of the light propagation in the ring cavity or the waveguides. Therefore, the complete process—the light is coupled into the ring cavity, transmits in the ring cavity and coupled out of the ring—could be described by the product of matrixes easily. The multi-ring resonators with different connection structures can also be described by this method. We will take single ring resonator as an example for analysis. As we know, the propagation constants of the waveguide and the ring should be the same for efficient coupling from one to another. In the following analysis, we suppose the propagation constants are equal by proper design and optimization.

2.4.1 Amplitude coupling equation

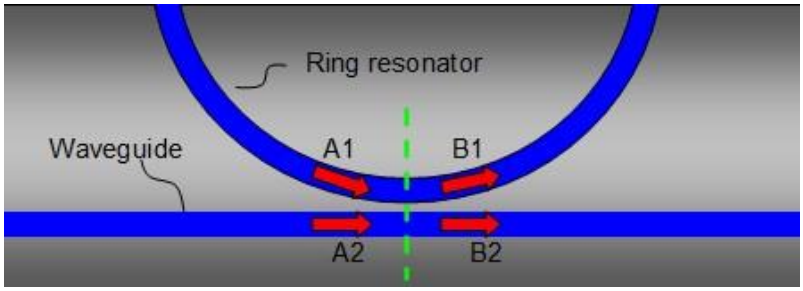

Fig. 2.10 The coupling between ring and waveguide

For the coupling region as shown in Fig. 2.10, A_1 and A_2 are input amplitudes in the ring and the straight waveguide. B_1 and B_2 are output amplitudes in the ring and the waveguide, respectively. Analyzing the optical field transmission in the coupling region by coupled-mode equation, we can obtain

$$B_1 = tA_1 - j\kappa A_2 \tag{2.33}$$

$$B_2 = -j\kappa A_1 + tA_2 \tag{2.34}$$

where κ is amplitude coupling coefficient for the crossover passing through the coupling region, t is the amplitude transmission coefficient. They are described as

$$\kappa = \sin[\int_{-L}^{L} K(z)dz] \tag{2.35}$$

$$t = \cos[\int_{-L}^{L} K(z)dz] \tag{2.36}$$

where $K(z)$ is the coupling coefficient as a function of position z in the direction of light propagation. It is easy to derive $\kappa^2 + t^2 = 1$, which is in accordance with the law of conservation of energy. Here we assume κ and t do not change with wavelength.

Eqs. (2.33) and (2.34) can be represented in matrix form as follows

$$\begin{pmatrix} B_1 \\ B_2 \end{pmatrix} = \begin{pmatrix} t & -j\kappa \\ -j\kappa & t \end{pmatrix} \begin{pmatrix} A_1 \\ A_2 \end{pmatrix} \tag{2.37}$$

which gives the transfer matrix equation of the coupling region.

2.4.2 Single ring

The structure of single ring resonator is shown in Fig. 2.11. Here *R* is the radius of the ring. The length of the input and output waveguides is 2L. The light injected from input port will inter-couple into the ring in the coupling region as shown in Fig. 2.10. A part of the light from the waveguide is coupled into the ring and at the same time a part of the light from the ring is coupled into the waveguide. As a result, a part of the light is coupled into the output waveguide.

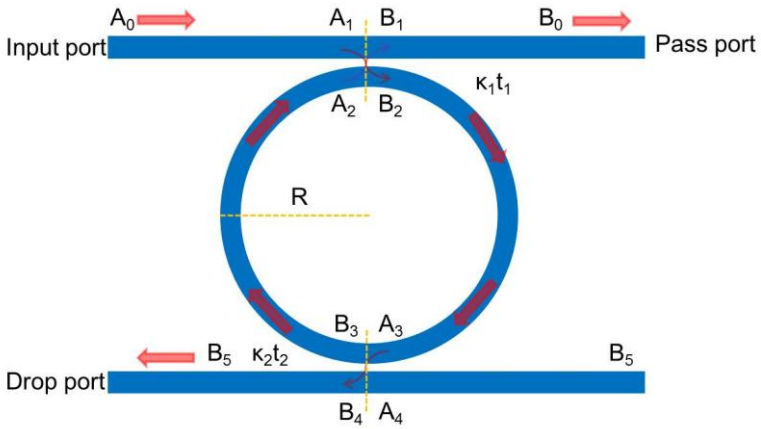

Fig. 2.11 Schematic of single ring resonator with input and output waveguides

The propagation constant of the ring and the waveguide are expressed as $\beta = 2\pi n_{eff} / \lambda$. α_R is the loss coefficient of the optical mode in the ring, which includes the propagation loss, scattering loss, banding loss and leakage loss. α_L is the loss coefficient in the waveguide. κ_1, κ_2 and t_1, t_2 are amplitude coupling coefficient and amplitude transmission coefficient of the two coupling regions, respectively. A_i and B_i are the input and output amplitudes of a coupling region, respectively.

2.4.3 Transfer function

Likewise, according to Eqs. (2.33) and (2.34), we can get

$$B_1 = t_1 A_1 - j\kappa_1 A_2 \tag{2.38}$$

$$B_2 = t_1 A_2 - j\kappa_1 A_1 \tag{2.39}$$

The two equations above can be rewritten as

$$A_2 = \frac{t_1}{j\kappa_1} A_1 - \frac{1}{jk_1} B_1 \tag{2.40}$$

$$B_2 = \frac{1}{j\kappa_1} A_1 - \frac{t_1}{jk_1} B_1 \tag{2.41}$$

which can written in matrix form

$$\begin{pmatrix} A_2 \\ B_2 \end{pmatrix} = \begin{pmatrix} \frac{t_1}{j\kappa_1} & -\frac{1}{j\kappa_1} \\ \frac{1}{j\kappa_1} & -\frac{t_1}{j\kappa_1} \end{pmatrix} \begin{pmatrix} A_1 \\ B_1 \end{pmatrix} \tag{2.42}$$

Similarly, we can get

$$\begin{pmatrix} A_4 \\ B_4 \end{pmatrix} = \begin{pmatrix} \frac{t_2}{j\kappa_2} & -\frac{1}{j\kappa_2} \\ \frac{1}{j\kappa_2} & -\frac{t_1}{j\kappa_2} \end{pmatrix} \begin{pmatrix} A_3 \\ B_3 \end{pmatrix} \tag{2.43}$$

At the same time, according to the transmission in the ring cavity we can get the change of amplitude as

$$A_3 = B_2 \exp(-j(\beta - j\alpha_R)\pi R) \tag{2.44}$$

$$A_2 = B_3 \exp(-j(\beta - j\alpha_R)\pi R) \tag{2.45}$$

The two equations above can be transformed to matrix form as

$$\begin{pmatrix} A_3 \\ B_3 \end{pmatrix} = \begin{pmatrix} 0 & \exp(-j(\beta - j\alpha_R)\pi R) \\ \exp(j(\beta - j\alpha_R)\pi R) & 0 \end{pmatrix} \begin{pmatrix} A_2 \\ B_2 \end{pmatrix} \tag{2.46}$$

From Eqs. (2.42), (2.43) and (2.46), we can get

$$\begin{pmatrix} A_4 \\ B_4 \end{pmatrix} = \begin{pmatrix} \frac{t_2}{j\kappa_2} & -\frac{1}{j\kappa_2} \\ \frac{1}{j\kappa_2} & -\frac{t_1}{j\kappa_2} \end{pmatrix} \begin{pmatrix} 0 & \exp(-j(\beta - j\alpha_R)\pi R) \\ \exp(j(\beta - j\alpha_R)\pi R) & 0 \end{pmatrix} \begin{pmatrix} \frac{t_1}{j\kappa_1} & -\frac{1}{j\kappa_1} \\ \frac{1}{j\kappa_1} & -\frac{t_1}{j\kappa_1} \end{pmatrix} \begin{pmatrix} A_1 \\ B_1 \end{pmatrix} \tag{2.47}$$

Then we can obtain

$$B_1 = MA_1 + NA_4 \tag{2.48}$$

$$B_4 = NA_1 + M'A_4 \tag{2.49}$$

Here

$$\begin{cases} M = \dfrac{t_1 - t_2 \exp(-j2(\beta - \alpha_R)\pi R)}{1 - t_1 t_2 \exp(-j2(\beta - \alpha_R)\pi R)} \\ M' = \dfrac{t_2 - t_1 \exp(-j2(\beta - \alpha_R)\pi R)}{1 - t_1 t_2 \exp(-j2(\beta - \alpha_R)\pi R)} \\ N = -\dfrac{\kappa_1 \kappa_2 \exp(-j(\beta - \alpha_R)\pi R)}{1 - t_1 t_2 \exp(-j2(\beta - \alpha_R)\pi R)} \end{cases} \tag{2.50}$$

Since A_4=0, Eqs. (2.48) and (2.49) can be rewritten as

$$\frac{B_1}{A_1} = \frac{t_1 - t_2 \exp(-j2(\beta - \alpha_R)\pi R)}{1 - t_1 t_2 \exp(-j2(\beta - \alpha_R)\pi R)} \tag{2.51}$$

$$\frac{B_4}{A_1} = -\frac{\kappa_1 \kappa_2 \exp(-j(\beta - \alpha_R)\pi R)}{1 - t_1 t_2 \exp(-j2(\beta - \alpha_R)\pi R)} \tag{2.52}$$

Considering the distance from input and output port to the coupling region is L and the propagation loss coefficient of the waveguide is α_L, we can get

$$\begin{cases} A_0 = A_1 \exp(j(\beta - \alpha_L)L) \\ B_0 = B_1 \exp(-j(\beta - \alpha_L)L) \\ B_5 = B_4 \exp(-j(\beta - \alpha_L)L) \end{cases} \tag{2.53}$$

From Eqs. (2.51), (2.52) and (2.53) we can achieve the transfer functions from input port 1 to output port 2 and from input port 1 to output port 3 as follows

$$U = \frac{B_0}{A_0} = \frac{B_1}{A_1} \exp(-2j(\beta - \alpha_L)L) = \frac{t_1 - t_2 \exp(-j2(\beta - \alpha_R)\pi R)}{1 - t_1 t_2 \exp(-j2(\beta - \alpha_R)\pi R)} \exp(-2j(\beta - \alpha_L)L) \tag{2.54}$$

$$V = \frac{B_5}{A_0} = \frac{B_4}{A_1} \exp(-2j(\beta - \alpha_L)L) = \frac{-\kappa_1 \kappa_2 \exp(-j(\beta - \alpha_R)\pi R)}{1 - t_1 t_2 \exp(-j2(\beta - \alpha_R)\pi R)} \exp(-2j(\beta - \alpha_L)L) \tag{2.55}$$

In case α_R =0 and α_L =0, it is easy to find

$$|U|^2 + |V|^2 = 1 \tag{2.56}$$

It means input power and output power are equal without propagation loss of waveguide and ring resonator.

2.5 Analysis of the operation characteristics of ring resonator

In this part, we will analyze the influence of different parameters of the ring resonator. We take SOI waveguide as an example. At 1550 nm, the effective index of TE mode is 2.8 and the group index is 3.62.

κ is amplitude coupling coefficient in the coupling region and we can get the power coupling coefficient as

$$K = \kappa^2 \tag{2.57}$$

In the following analysis, we use *K* to represent the coupling effect of the coupling region.

$\frac{B_4}{A_1}$ is the amplitude transmission coefficient of the ring resonator. According to Eq. (2.52), the power transmission spectrum of the ring resonator is defined as

$$T = 10 \times \log_{10} \left| \frac{B_4}{A_1} \right|^2 = 10 \times \log_{10} \left| -\frac{\kappa_1 \kappa_2 \exp(-j(\beta - \alpha_R)\pi R)}{1 - t_1 t_2 \exp(-j2(\beta - \alpha_R)\pi R)} \right|^2 \tag{2.58}$$

To design a ring resonator, we have to decide several parameters such as the power coupling coefficient and the length of the cavity.

2.5.1 Influence of coupling coefficient

Fig. 2.12 shows the influence of different coupling coefficients of the two coupling regions. The transmission spectrum from the drop port is monitored. Here we set K_1=0.05, K_2=0.05, 0.1 and 0.2. The radius is 5 μm and the loss is assumed to be zero. From the simulation results we can see that when K_1=K_2, the output reaches the maximum. When K_1 is not equal to K_2, the output power of the drop port decreases. Therefore, we make K_1=K_2=K in the following analysis and the real device design.

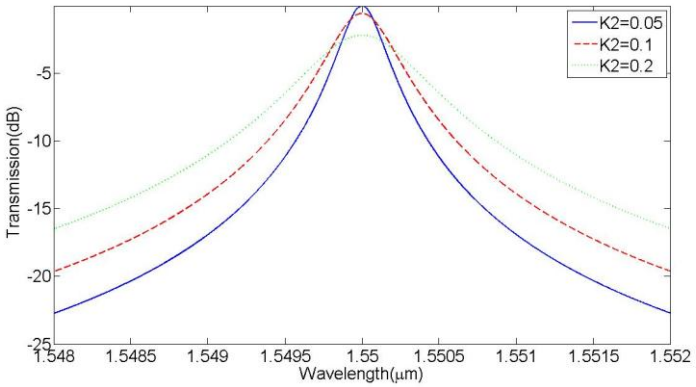

Fig. 2.12 The transmission of ring with different drop port coupling coefficients.

Fig. 2.13 shows the simulation results of different coupling coefficients for a given loss. Here R is 50 μm and the waveguide propagation loss is assumed to be 5 dB/cm (i.e. $\alpha=5/(4.343)$ cm^{-1}). As shown in Fig. 2.14, for a given loss, the sharpness and the Q value of the resonance peaks increase with the reduction of the coupling coefficient. But at the same time the power of the resonance peaks decreases. On the contrary, a larger K value results in less sharp resonance peaks but higher intensity. In practical device design, we have to consider the compromise between the sharpness of the peaks and the intensity.

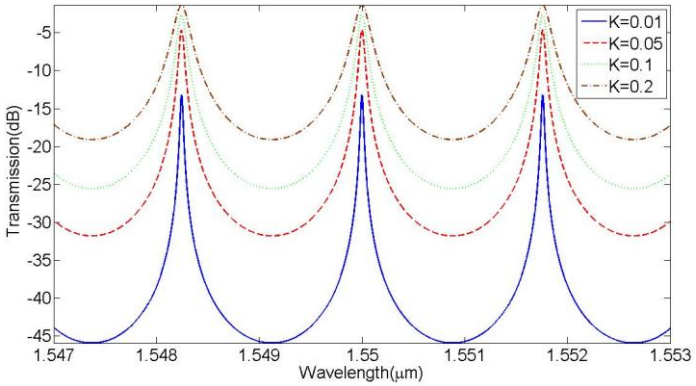

Fig. 2.13 Transmission of rings with different coupling coefficients for a given loss value of 5 dB/cm.

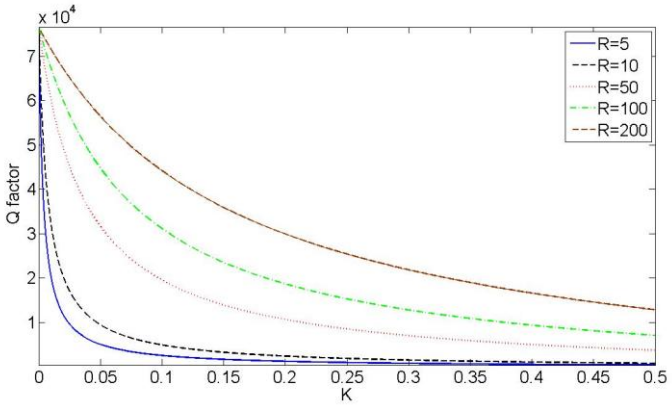

Fig.2.14 Q factor versus K value with radius of the ring as a parameter. The loss is assumed to be 5dB/cm.

2.5.2 Influence of the propagation loss

Fig. 2.15 shows the influence of the waveguide loss to the output transmission through the drop port. We set the intensity coupling coefficient to 5 %. The radius of the ring is 5 μm. From the graph, we can see that the intensity of the resonance peaks decreases with increasing loss. In the fabrication of the bending waveguide, attention must be paid to keep the sidewall of the waveguide smooth to minimize the loss. Fig. 2.16 shows the *Q* factor as a function of the loss with a radius of 5 μm.

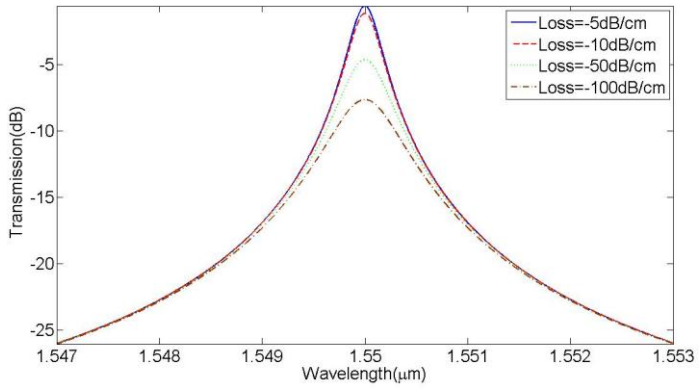

Fig. 2.15 The influence of the loss coefficient

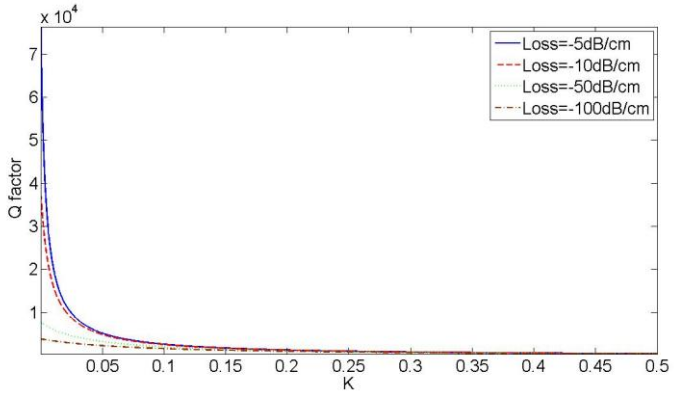

Fig. 2.16The *Q* factor versus *K* coefficient with loss coefficient as a parameter

2.5.3 Influence of the length of cavity

Fig. 2.17 shows the influence of the ring radius to the output transmission. Here we assume the *K* value is 10 % and the waveguide loss is 1 dB/cm. With the increase of the radius of the ring, the intensity of the resonance peaks decrease and the *Q* factor increases. The FSR is inversely proportional to the radius of the ring. Fig. 2.18 shows the *Q* factor as a function of the radius.

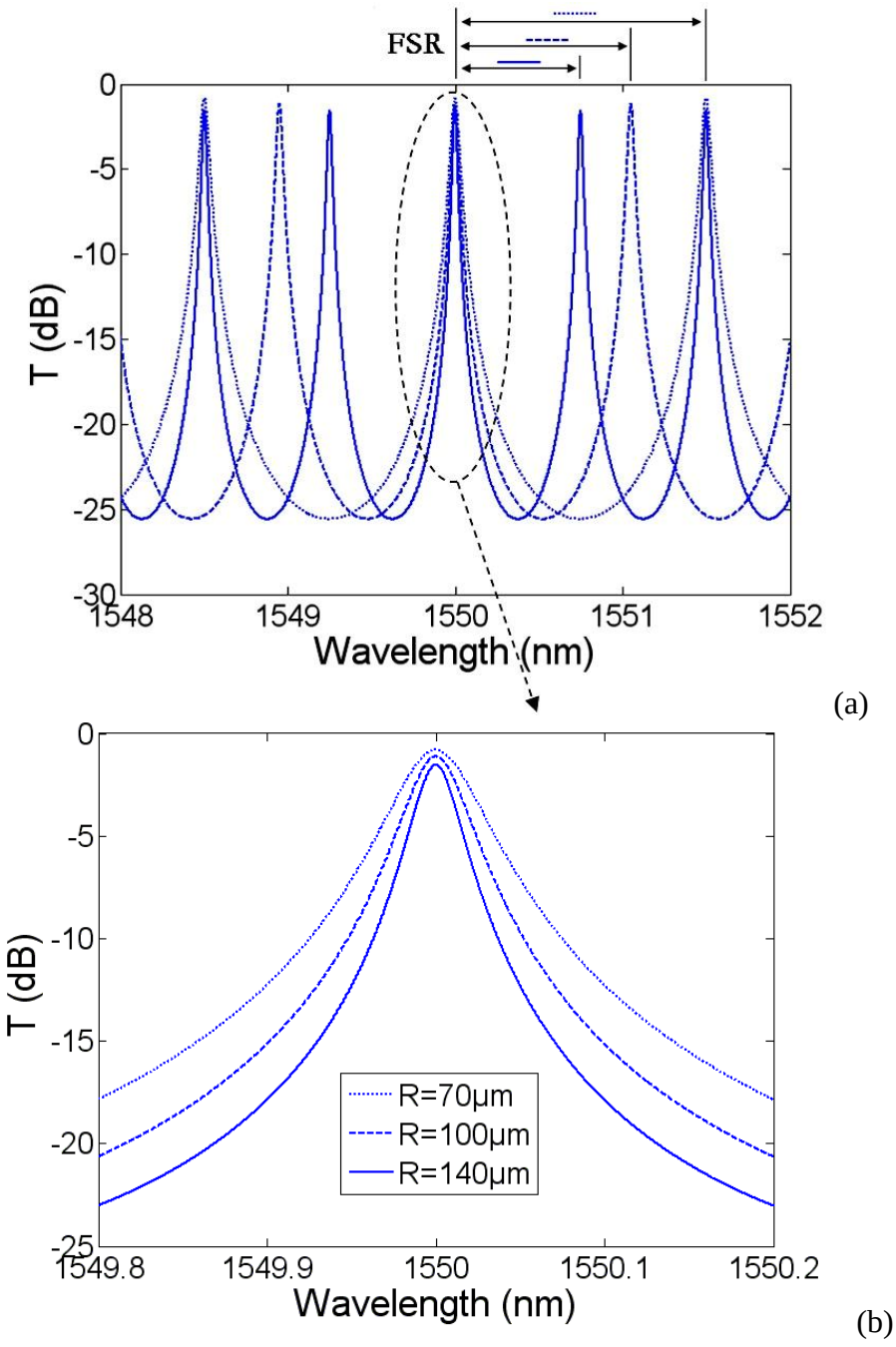

Fig. 2.17 The influence of cavity length to the transmission spectrum for a given *K* coefficient and loss value

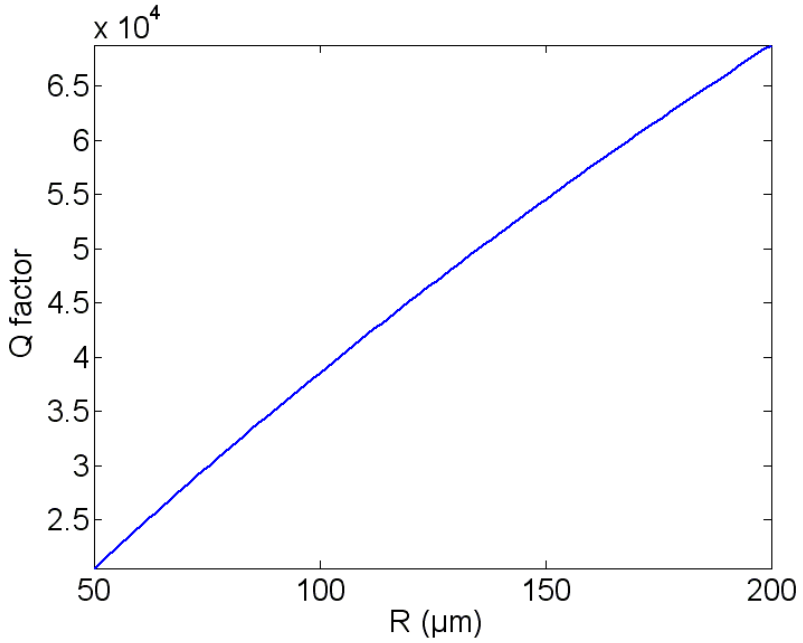

Fig. 2.18 The influence of cavity length to the *Q* factor for a given *K* coefficient and loss value

2.6 Sensor based on micro-ring resonator

Recently, micro-ring resonators have received great interest because of their merits such as low-cost, compactness, and integration potential. They have extensive applications in optical signal processor, filter, wavelength division multiplexer/demultiplexer, wavelength converter, modulator and laser. In addition, micro-ring resonators are suitable for sensing applications. The transmission resonance peaks are sharp and can shift sensitively with the surrounding refractive index change. The small footprints of ring resonators allow for integration with other devices for high-sensitivity, low-cost, label-free optical sensors.

Micro-ring resonator sensor relies on the effective index change induced by the samples to be analyzed. From the resonance equation, we can get:

$$m \cdot d\lambda = \left(\frac{dn_{eff}}{dt} \cdot dt + \frac{dn_{eff}}{d\lambda} \cdot d\lambda \right) \cdot L \tag{2.59}$$

$\frac{dn_{eff}}{dt} \cdot dt$ is the change of effective index of mode and $\frac{dn_{eff}}{d\lambda}$ is wavelength dispersion coefficient. For waveguide with small wavelength dispersion, we can get

$$\frac{d\lambda}{\lambda} = \frac{dn_{eff}}{n_{eff}} \tag{2.60}$$

Hence, the resonance wavelength can shift with the change of effective index of mode. We can detect the shift of wavelength to measure the refractive index change of the sample.

For large dispersion waveguide, we cannot ignore the dispersion. From Eq. (3.41) we can get

$$d\lambda = \lambda \cdot \frac{\frac{dn_{eff}}{dt} \cdot dt}{\left(n_{eff} - \frac{dn_{eff}}{d\lambda} \cdot \lambda \right)} = \lambda \cdot \frac{dn_{eff}}{n_g} \tag{2.61}$$

It can be written as

$$\frac{d\lambda}{\lambda} = \frac{dn_{eff}}{n_g} \tag{2.62}$$

Considering the transmission shift of one SFR

$$d\lambda = FSR = \frac{\lambda^2}{n_g \cdot L} \tag{2.63}$$

From Eq. (2.62), we can obtain the measurement range

$$\Delta n_{eff} = \frac{d\lambda}{\lambda} \cdot n_g = \frac{\left(\frac{\lambda^2}{n_g \cdot L} \right)}{\lambda} \cdot n_g = \frac{\lambda}{L} = \frac{n_{eff}}{m} \tag{2.64}$$

From the Eq. (2.64), we can find the refractive index change to allow one SFR shift of the transmission spectrum is dependent on the resonance order, or in another word, the cavity length.

Reference

[1] M. S. Stern, "Semivectorial polarized finite difference method for optical waveguides with arbitrary inde profiles," IEEE Proceedings Pt. J., 135, 56-63, 1988.

[2] B. M. A. Rahman and J. B. Davies, "Finite-element solution of integrated optical waveguides," IEEE J. Lightwave Technol., 2, 682-687,1984.

[3] W. Yang and A. Gopinath, "A boundary integral method for propagation problems in integrated optical structures," J. Lightwave Technol., 7, 777-779, 1995.

[4] M. M. Ney, "Method of moments as applied to electromagnetic problems," IEEE Trans. Microwave Theory Tech., 33, 972-980, 1985.

[5] S. Jungling, and J. C. Chen, "A study and optimization of eigenmode calculations using the imaginary-distance beam-propagation method," IEEE J. Quantum Electron., 30, 2098-2105, 1994.

[6] Y. C. Chuang, and N. Dagli, "An assessment of finite difference beam propagation method," IEEE J.Qutantum Electron., 26, 1335-1339, 1990.

[7] R. Scarmozzino and R. M. Osgood, "Comparison of finite-difference and Fourier-transform solutions of the parabolic wave equation with emphasis on integrated-optics applications," J. Opt. Soc. Am. A., 8, 724-731, 1991.

[8] B. A. M. Rahman and J. B. Davies, "Finite element analysis of optical and microwave problems," IEEE Trans.Microwave Theory Tech., 32, 20-28, 1983.

[9] G. R. Hadley, "Wide-angle beam propagation using Padé approximant operators," Opt. Lett., 17, 1426-1428, 1992.

[10] H. L. Rao, R. Scarmozzino, and R. M. Osgood, "A bi-directional beam propagation method for multiple dielectric interfaces," IEEE Photon. Technol. Lett., 11, 830-832, 1999.

[11] W. P. Huang, C. L. Xu, and S. K. Chaudhuri, "A finite-difference vector beam propgation method for three-dimensional waveguide structures," IEEE Photon. Technol. Lett., 41, 148-151, 1992.

[12] A. Taflove, "Review of the formulation and application of the finite-difference time-domain method for numerical modeling of electromagnetic wave infractions with arbitrary structures", Wave Motion, 10, 547-582, 1988.

[13] A. Taflove, "Computational Electrodynamics: The Finite-difference Time-domain Method," Artech House, Norwood, MA, 1995.

[14] K. S. Yee, "Numerical solution of initial boundary value problems involving Maxwell's equations in isotropic media," IEEE Trans. Antennas Propagat., 14, 302-307, 1966.

[15] A. Densmore, D.-X. Xu, P. Waldron, S. Janz, P. Cheben, J. Lapointe, A. Delâge, B. Lamontagne, J. H. Schmid, and E. Post, "A Silicon-on-Insulator Photonic Wire Based Evanescent Field Sensor," IEEE Photon. Technol. Lett., 18, 2520-2522 , 2006.

CHAPTER 3

Sensor based on cascaded laser and ring resonator

Recently optical label-free biosensors have received great interest because of their merits such as low cost, high sensitivity and ultra-compactness [1-4]. Surface plasmon resonance in noble-metal nano-structures and evanescent field (EF) waveguide sensing are two main optical techniques that are commonly used in real-time label-free biosensing applications such as environmental monitoring, biological recognition, medical diagnostics, food quality and safety analysis [1-12]. Significant efforts are put into the development of EF sensors due to their potential for increased sensitivity and suitability for implementing into multi-channel detection. The waveguide EF sensors rely on monitoring the perturbation of the waveguide mode effective refractive index due to the varying concentration of an analyte in the solution covering the waveguide surface. A variety of structures and mechanisms have been developed such as interferometer-based biosensors [5, 6], high-Q ring resonator based biosensors [7-11], and optical fiber based biosensors [12]. Among them, micro-ring resonators allow a higher sensitivity due to the sharp resonance peaks and small footprints.

In most of these photonic biosensors, a crucial component is a transducer that can transform a refractive index change in its environment to a measurable change in its optical transmission. In this work, we focus on the sensors with micro ring resonator as the transducer due to the merits of high sensitivity, low cost, small footprint and potential for large array fabrication and integration.

The refractive index change of the environment can be deduced from the monitoring of the transmission wavelength shift or output power change. The wavelength interrogation method requires a high-end tunable laser or high resolution spectrum analyzer which is not suitable for low-cost integrated devices. In this work, we focus on intensity interrogation method due to its potential for achieving low-cost, easy-to-fabricate and fully integrated devices.

Silicon-on-insulator (SOI) is a material system with many advantages for sensing applications. Its high index contrast allows high-sensitivity and integration of many sensors on a small chip to simultaneously measure multiple parameters. Moreover, it permits cheap and reliable fabrication in high volume with CMOS-compatible processes. Recently, several research groups have demonstrated ring resonator based sensors on SOI [6-11]. The common method is based on wavelength interrogation that measures the wavelength shift of the resonance peaks. I

In this chapter, we introduce a sensor based on cascaded FP laser and ring sensor using intensity interrogation. The passive ring resonator is fabricated on SOI while the FP laser is fabricated in InGaAsP/InP. The devices have been investigated theoretically and experimentally, demonstrating its principle and potential for low-cost practical applications.

3.1 Basic structure and principle of the cascaded sensor

In this section, we introduce the basic principle and structure of an intensity interrogated sensor using a multimode Fabry-Perot (FP) laser cascaded with a single ring resonator. The ring resonator and the FP laser cavity have slightly different free spectral ranges (FSRs) so that the Vernier effect can be employed to greatly increase the sensitivity. In contrast to the all-passive cascaded double-ring sensor, a multimode FP laser, instead of a passive reference ring, is integrated in the system for producing a reference comb. This not only eliminates the need for an external broadband source, but also produces a much higher spectral power density and energy efficiency. The sensitivity is also improved due to the narrow linewidth of each mode of the FP laser as compared to the transmission peaks of the reference ring.

3.1.1 Basic structure

Fig. 3.1(a) shows the device structure of the sensor. The output of an FP laser is coupled to a single micro-ring resonator through the input port of the bus waveguide. The light corresponding to the resonant wavelengths of the ring is transmitted through the ring and output to the drop port while the light of all other wavelengths is passed straight through to the pass port. The FP laser can be replaced by a ring laser as shown in Fig. 3.1(b) with the same working principal.

In the example device considered in this experiment, the FP laser is fabricated on InP based material system, while the ring resonator is fabricated in SOI for high refractive index sensitivity. The SOI waveguide is covered by an upper cladding layer except in the sensing window containing the ring resonator which is exposed to a fluid sample to be analyzed. The FSRs of the FP cavity $\Delta\lambda_{FSR_L}$ and the ring resonator $\Delta\lambda_{FSR_R}$ are designed to be as close as possible for obtaining high sensitivity with the intensity interrogation method. The output power is measured by a detector at the end of the drop port of the ring.

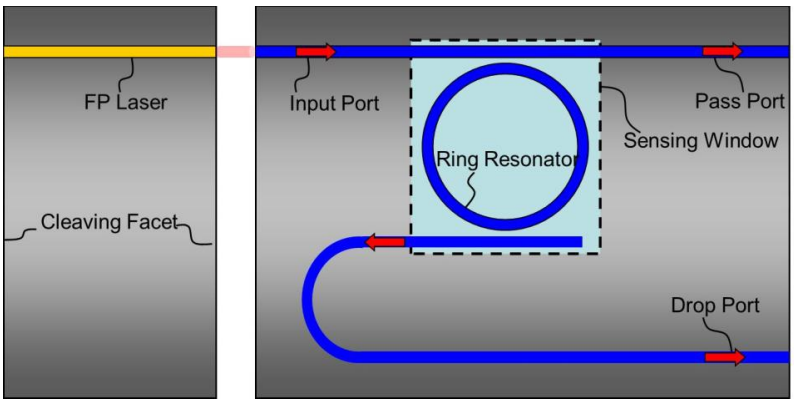

(a)

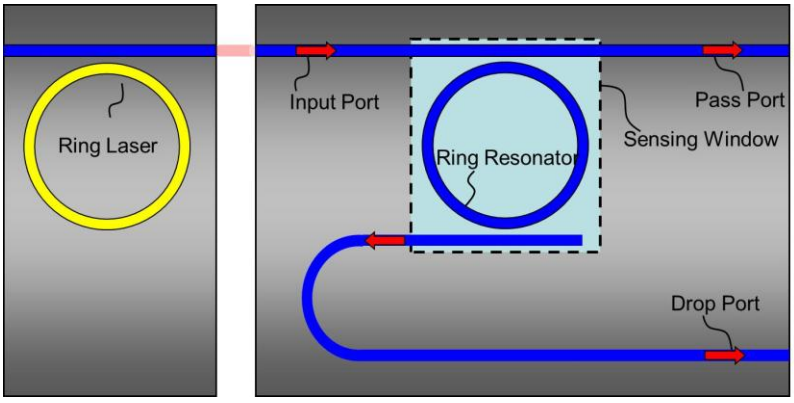

(b)

Fig. 3.1. Schematic of the cascaded FP cavity laser (a) or ring laser (b) and micro-ring resonator sensor.

3.1.2 Working principle and transmission analysis

There are two common interrogation approaches that have been applied in optical micro-resonant cavity based sensing: intensity interrogation and wavelength interrogation [7]. Although the sensor chips can be made cheap, wavelength interrogation scheme demands an expensive high-end tunable laser scanning repeatedly the transmission spectra of the sensors or a high resolution optical spectrum analyzer (OSA) for monitoring accurately the spectral shifts. These instruments are very expensive and bulky. A low-resolution micro-OSA based on array waveguide grating (AWG) or etched diffraction grating (EDG) can be integrated with optical sensors on the same chip [8, 13, 14]. This requires the sensors to have a large resonant wavelength shift with a small refractive index change of analyte. An alternative approach to reduce the cost of the sensing system is to use intensity interrogation instead of wavelength interrogation. Although the intensity interrogation can be realized by measuring the intensity change at a fixed wavelength at the resonance peak of a high-Q ring resonator, the light source needs to have a very accurate wavelength with a narrow bandwidth and a high stability, which is difficult to achieve in practice. A more practical low-cost approach is to measure the transmitted power of a cascaded double-ring sensor with a broadband source as the input [11]. A high sensitivity of 450 dB/RIU (refractive index units) was achieved experimentally. A drawback of this approach is that the low spectral power density of the broadband source results in a low output power especially when the resonant peaks are sharp. In this work, the intensity interrogation is adopted for the simplicity and low cost. The difference is that we used an FP laser as the source whose power density is much higher than the broad band source.

The output power distribution $P_L(\lambda)$ of the multimode FP laser source can be written as the product of a spectral power distribution function $P_G(\lambda)$ which is related to the material gain, and a periodic comb function $C_L(\lambda)$ corresponding to the resonance peaks of the FP cavity, i.e.,

$$P_L(\lambda) = P_G(\lambda) C_L(\lambda) \tag{3.1}$$

Assuming the transmission coefficient of the ring is $T_R(\lambda)$, the output signal of the sensor P_O is given by

$$P_O = \int_0^\infty [P_L(\lambda)T_R(\lambda)]d\lambda = \int_0^\infty [P_G(\lambda)C_L(\lambda)T_R(\lambda)]d\lambda \tag{3.2}$$

Both the reference comb $C_L(\lambda)$ and the ring transmission $T_R(\lambda)$ exhibit a series of periodic peaks. When the FSRs of the FP cavity and the ring resonator are slightly different, the product $C_L(\lambda)T_R(\lambda)$ has a series of peaks with varying amplitudes, as shown by the solid curve in Fig. 3.2 (a). The highest peak occurs at the position where a resonance peak of the ring is well aligned with a resonance peak of the FP cavity. The envelope function is also periodic with the period given by

$$\Delta\lambda = \frac{\Delta\lambda_{FSR_L}\Delta\lambda_{FSR_R}}{\left|\Delta\lambda_{FSR_L} - \Delta\lambda_{FSR_R}\right|} \tag{3.3}$$

where $\Delta\lambda_{FSR_L} = \lambda^2 / 2n_L L_L$ and $\Delta\lambda_{FSR_R} = \lambda^2 / n_R L_R$ are the FSRs of the FP cavity and the ring, respectively. Here n_L, n_R are the group effective refractive indices and L_L, L_R are the lengths of the waveguides of the FP cavity and the ring, respectively.

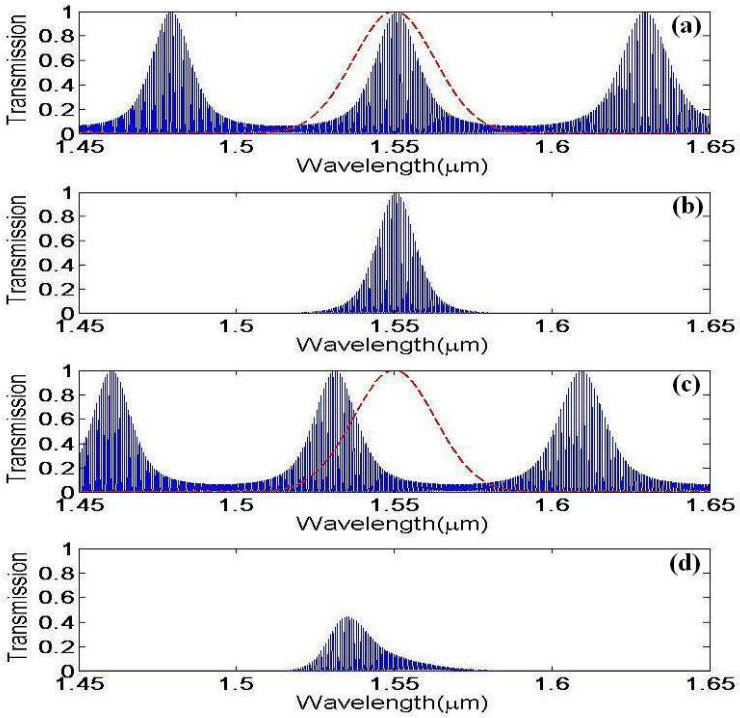

Fig. 3.2. (a) Product $C_L(\lambda)T_R(\lambda)$ for cascaded FP cavity and ring resonator with slightly different FSRs (solid curve) when its envelope function is aligned with the spectral power distribution function $P_G(\lambda)$ (dashed curve); (b) Output spectrum corresponding to case (a); (c) Same as (a) but the envelope function is shifted by the refractive index variation of the analyte; (d) Output spectrum corresponding to case (c) with reduced total power.

The spectral power distribution $P_G(\lambda)$ can be approximately represented by a Gaussian function as shown by the dashed curve in Fig. 3.2 (a). When the refractive index of the fluidic sample in the reservoir above the sensing window changes, the resonant wavelengths of the ring shifts by

$$\Delta\lambda_R = \lambda\Delta n_{eff} / n_{eff} \tag{3.4}$$

where n_{eff} and Δn_{eff} are the effective refractive index of the ring and its variation, respectively. The envelope function of the product $C_L(\lambda)T_R(\lambda)$ shifts by $F\Delta\lambda_R$ because of the Vernier effect, with the amplification factor F given by

$$F = \frac{\Delta\lambda_{FSR_L}}{\left|\Delta\lambda_{FSR_L} - \Delta\lambda_{FSR_R}\right|} \tag{3.5}$$

From Eq. (3.2), the output signal of the sensor is determined by the overlap integral of the spectral power distribution function $P_G(\lambda)$ and the product $C_L(\lambda)T_R(\lambda)$. When the envelope function of the product $C_L(\lambda)T_R(\lambda)$ is aligned with $P_G(\lambda)$, the output power is maximal, as shown in Fig. 3.2 (b). When the envelope function is shifted by the refractive index variation of the analyte, as shown in Fig. 3.2 (c), the output spectrum will be reduced, as shown in Fig. 3.2 (d). Since the envelope function can shift sensitively to the effective index change of the ring, a highly sensitive intensity interrogated sensor can be achieved.

For the intensity interrogation, only half period of the envelope function can be used in order to uniquely determine the refractive index change. Therefore, the maximal shift of the resonant wavelengths of the ring is half of its FSR, i.e., $\Delta\lambda_R = \frac{1}{2}\Delta\lambda_{FSR_R}$. The measurement range of the refractive index change is therefore given by

$$\Delta n_{\max} = \frac{1}{2} S \times \lambda n_{eff} / n_R L_R \tag{3.6}$$

where S is the ratio of the change in the waveguide effective refractive index to the change of the analyte refractive index, which is determined by the transverse structure of the waveguide.

3.2 Design and simulation

In this section we show the design and simulation of an example device used in our experimental demonstration. The FP laser and the ring sensor are based on InP system and SOI system, respectively. Simulation and calculation were performed and the key parameters such as the FSR difference and Q factor were discussed.

3.2.1 Design parameters

The ring resonator is designed on SOI substrate with a 220 nm Si layer on a 2 μm SiO_2 insulator layer. For rib waveguide with the silicon layer fully etched through, because of the high refractive index contrast, the waveguide width needs to be designed rather small to keep it single mode. The gap between the bus waveguide and the ring also needs to be very small (in the order of 0.1 μm) in order to achieve required coupling. Consequently, the fabrication process requires e-beam lithography, which is costly and time consuming. For the device reported in this work, we use shallow etched ridge waveguides of 1 μm wide with about 40 nm in height in order to maintain the single mode operation. Directional couplers with 1 μm gaps between the bus waveguide and the ring are used to couple light into and out of the ring resonator. The sensor can therefore be fabricated by conventional photolithography. The interference order of the ring at 1550 nm is chosen to be 1600, corresponding to a ring diameter of 280 μm. Assume the coupling coefficient between the ring and the bus waveguide is 40 % and the propagation loss of the waveguide is 1 dB/cm. The corresponding FWHM of the resonance peaks of the sensing ring is 125 pm.

For the ideal case of TM polarization, the ratio between the effective index change and the sample index change is 42 % which is much higher than that of TE mode. Because of the resolution limit of the contact photolithography, the designed 1 μm-wide shallow etched waveguide has high loss for TM mode due to the lateral leakage [15]. As a result, we can only use TE mode for which the ratio between the effective index change and the sample index change is 4.7 %.

The FP laser is fabricated on InP substrate using a standard laser structure with 5 InGaAsP quantum wells. The ridge waveguide of the laser is 3 μm wide. The laser sample is cleaved into appropriate length (~470 μm) to obtain approximately the same FSR as that of the ring.

When the FP cavity and the ring have exactly the same FSR, the overall FSR of the cascaded sensor becomes infinite, as we can see from Eq. (3.3). In this case, the product $C_L(\lambda)T_R(\lambda)$ exhibits a series of resonant peaks with an uniform amplitude that depends on the degree of overlap between the resonance peaks of the FP cavity and the ring, which is in turn determined by the effective index of the ring. Usually, the FSR of the FP cavity is slightly different from that of the ring, due to limitation by the accuracy of the cleaving. As a result, the envelope function of the product $C_L(\lambda)T_R(\lambda)$ becomes a periodic function with the period (referred as the overall FSR) determined by Eq. (3.3). It decreases when the FSR difference between the FP cavity and the ring increases.

3.2.2 Influence of the FSR difference

In the case of cascaded double-ring sensor with a broadband source, it was shown that the overall FSR must be much larger than the spectral bandwidth of the input source. The sensitivity decreases drastically with the FSR difference between the two rings due to the reduction of the overall FSR as shown in Fig. 3.3 [11]. Consequently, the FSR difference between the two rings needs to be limited to below 1.5 % for a broadband source with a bandwidth of 28 nm.

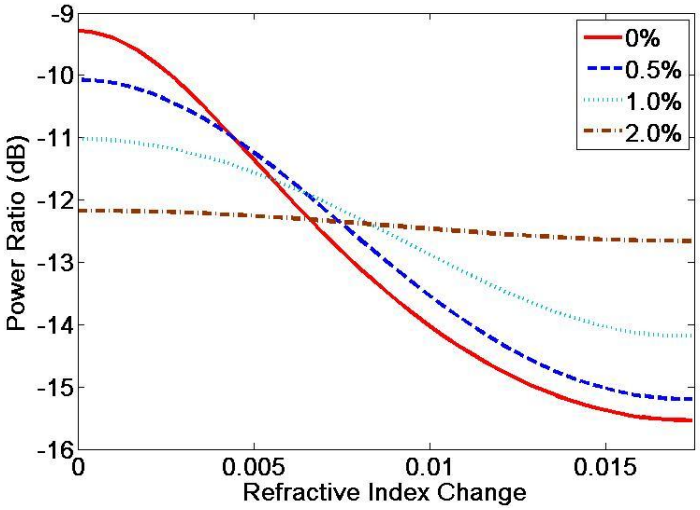

Fig. 3.3. Output power versus sample refractive index change with the FSR difference between the double ring resonators as a parameter.

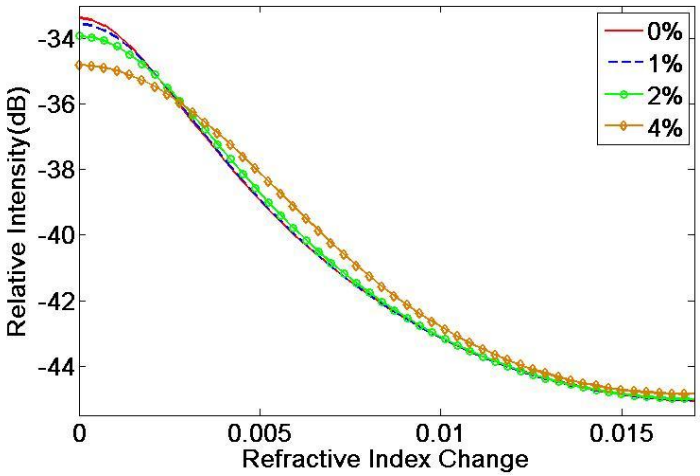

Fig. 3.4. Output power versus sample refractive index change with the FSR difference between the FP laser and the ring resonator as a parameter.

In our case, the 3 dB bandwidth of the spectral distribution function $P_G(\lambda)$ of the FP laser is only about 3 nm. The much narrower spectral distribution function $P_G(\lambda)$ makes the sensitivity of the sensor almost independent on the FSR difference between the FP cavity and the ring resonator. Fig. 3.4 shows the output power as a function of the sample refractive index change with the FSR difference as a parameter. We can see that the slopes of the curves are almost the same for different FSR differences. This results in a large tolerance on the cleaved cavity length of the FP laser.

3.2.3 Influence of the Q factor of the cavity

It should be mentioned that the sensitivity of the sensor increases with the sharpness of the resonance peaks of both the sensing ring and the reference comb. In the case of intensity interrogation using cascaded passive double-ring sensor with a broadband source, the higher sharpness of the resonance peaks (i.e. the Q-factor) of the rings leads to a lower output power [11], which in turn limits the sensitivity due to detection noises. Here, by using an FP laser for generating the reference comb, we obtain extremely sharp peaks with ultra-high spectral power density. According to the measurements by using a spectrum analyzer, the full width at half maximum (FWHM) of the peaks of the FP laser is about 50 MHz, corresponding to 0.4 pm at 1530 nm, or a Q-factor of 3.8×10^6.

To show the effect of the sharpness of the FP laser, we plot the output power change versus the sample refractive index change in Fig. 3.5 with the FWHM of the reference comb as a parameter. The FWHM of the sensing ring is assumed to be 125 pm and the FSR difference is set to 0. Apparently, the sensitivity of the sensor as represented by the slopes of the curves increases with the peak sharpness of the reference comb. When the FWHM of the reference comb is also 125 pm, the sensitivity is about 600 dB/RIU. It increases to 1270 dB/RIU when the FWHM of the reference comb is reduced to 0.4 pm. The increase saturates when the FWHM is below about 10 pm. Therefore, compared to the case of a double-ring sensor with the reference ring having the same FWHM as the sensing ring, the sensitivity is more than doubled by using the FP laser.

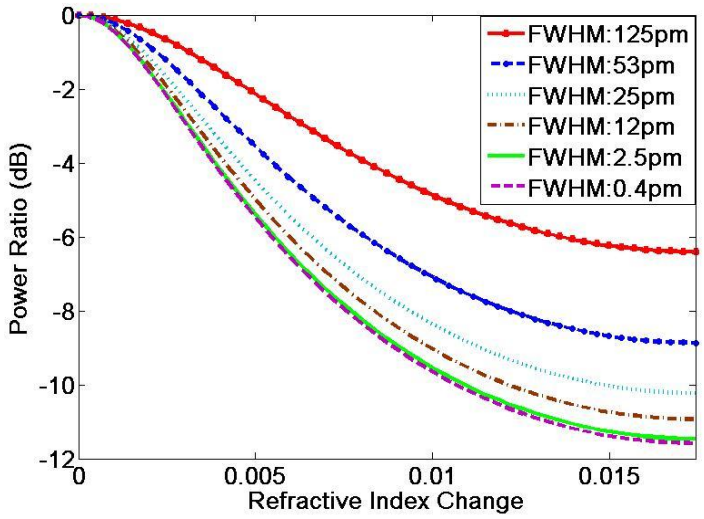

Fig. 3.5. Normalized output power change versus the sample refractive index change, with the FWHM of the peaks of the reference comb as a parameter.

3.3 Experimental results and discussions

In this section, we introduce the fabrication process of the ring and the FP laser, and the characterization of these devices. The InP based FP laser and the SOI ring resonator can be integrated on the same chip using flip-chip mounting or other hybrid integration techniques

[16-17]. As a proof-of-principle experiment, we fabricated the chips separately as discrete components and use an optical fiber to couple them.

3.3.1 Fabrication and characterization of the FP laser

The layer structure of the wafer for the FP laser fabrication is shown in Table. 3.1. The active layers consist of 5 QWs of $In_{0.8}Ga_{0.2}As_{0.8}P_{0.2.}$

No.	Layer	Composition	Thickness (μm)	Doping (cm^{-3})
1	Cap	p+ - InGaAs	0.2	Zn:1e19
2	Cladding	p - InP	1.5	Zn:1e18
3	Etch-stop	p - InGaAsP (1.3μm)	0.004	Zn:4e17
4	Cladding	p - InP	0.15	Zn:4e17
5	GRINSCH	p - InGaAsP (1.05μm)	0.025	Zn:4e17
6		p - InGaAsP (1.15μm)	0.025	Zn:4e17
7		p - InGaAsP (1.25μm)	0.025	Zn:4e17
8	QW	In0.8Ga0.2As0.8P0.2	0.0055	Si:4e17
9	Barrier	InGaAsP (1.25μm)	0.01	Zn:4e17
10	QW	In0.8Ga0.2As0.8P0.2	0.0055	Si:4e17
11	Barrier	InGaAsP (1.25μm)	0.01	Zn:4e17
12	QW	In0.8Ga0.2As0.8P0.2	0.0055	Si:4e17
13	Barrier	InGaAsP (1.25μm)	0.01	Zn:4e17
14	QW	In0.8Ga0.2As0.8P0.2	0.0055	Si:4e17
15	Barrier	InGaAsP (1.25μm)	0.01	Zn:4e17
16	QW	In0.8Ga0.2As0.8P0.2	0.0055	Si:4e17
17	GRINSCH	n - InGaAsP (1.25μm)	0.025	Si:4e17
18		n - InGaAsP (1.15μm)	0.025	Si:4e17
19		n - InGaAsP (1.10μm)	0.025	Si:4e17
20		n - InGaAsP (1.05μm)	0.025	Si:4e17
21	Buffer	n - InP	1.5	Si:2e18
--	Substrate	n+ - InP	--	S or Sn : ~ 4e18

Table 3.1. Layer structure of 5 QWs wafer for laser fabrication.

The FP laser chip was fabricated by standard procedure and the fabrication process as shown in Fig. 3.6 is described in detail as follows:

Process:
1) Photolithography to define the pattern 2) ICP dry etching to etch through the cap layer (etch depth around 400nm) 3) Remove the photo resist by oxygen plasma 4) Wet etching to form the ridge waveguide (Height of the ridge ~1.5 μm) 5) Planarization by SU-8 or BCB 6) Photolithography to define the electrode pattern 7) Metallization to deposit the electrode on top surface 8) Lift-off to remove the resist 9) Back side thinning 10) Back side electrode deposition Annealing and cleave into desired length

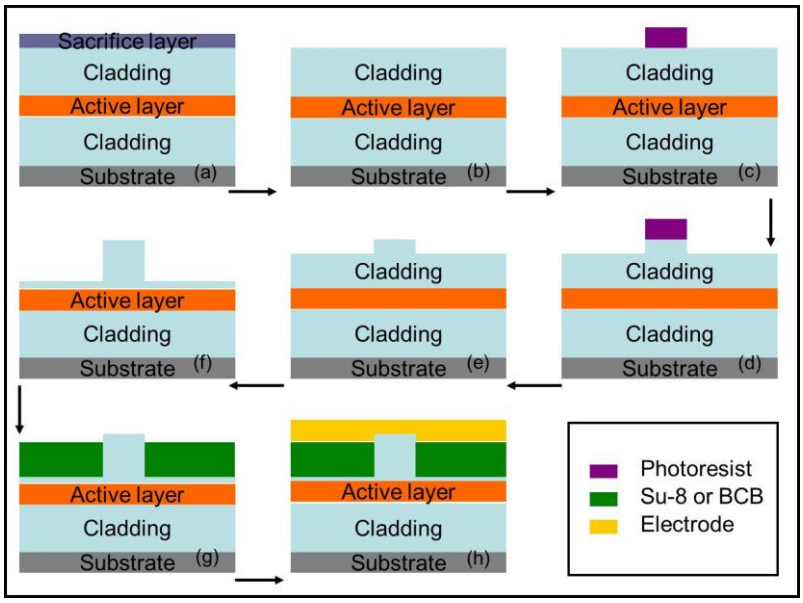

Fig. 3.6 Fabrication process of the FP laser.

The cross section of the FP laser chip is shown in Fig. 3.7. The sidewall is not perfectly vertical because of the anisotropic wet etching. The etching stopped at the etch-stop layer above the active region which can be recognized by different contrast from the photo. Then the array of FP laser was bonded to aluminum nitride plate which is of high thermal conductivity. The electrodes on the array were wire bonded to large surface electrodes on the same plate for convenience of test. The final chip is shown in Fig. 3.8.

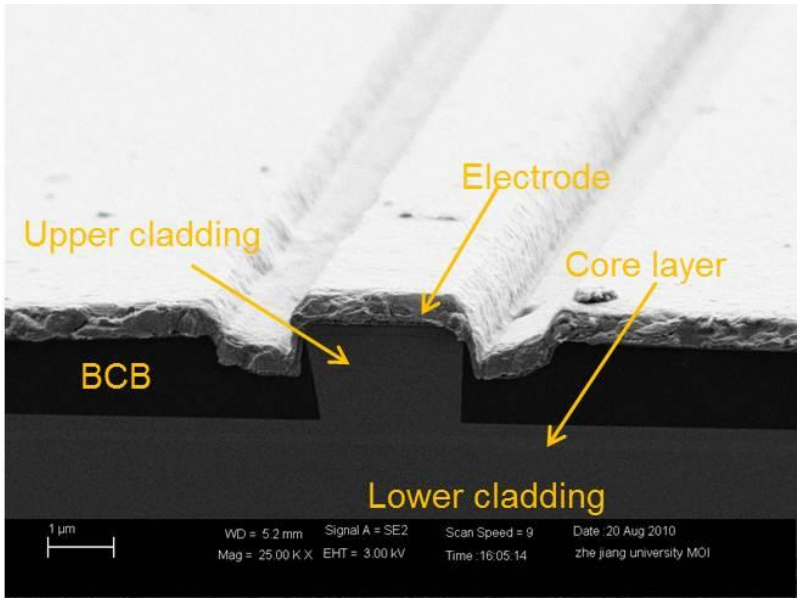

Fig. 3.7 Cross section of FP laser

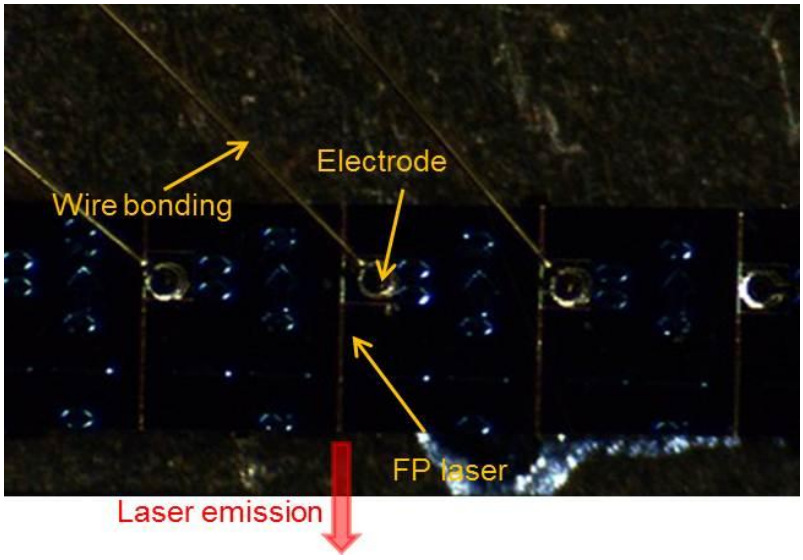

Fig. 3.8 Top view of laser array with wire bonding.

The FP laser was cleaved into cavity length of about 470 µm. The lasing performance was tested with a threshold current of around 20 mA as shown in Fig. 3.9 (a). The spectrum was measured by OSA shown in Fig 3.9 (b). The optical power (collected by lens fiber) at 50 mA was more than 3 dBm. During the operation of the laser, the temperature is controlled by thermoelectric cooling chip (TEC) at around 20 ℃. During the measurement of the cascaded laser and the sensor, the temperature can be used to adjust the spectrum of the laser chip.

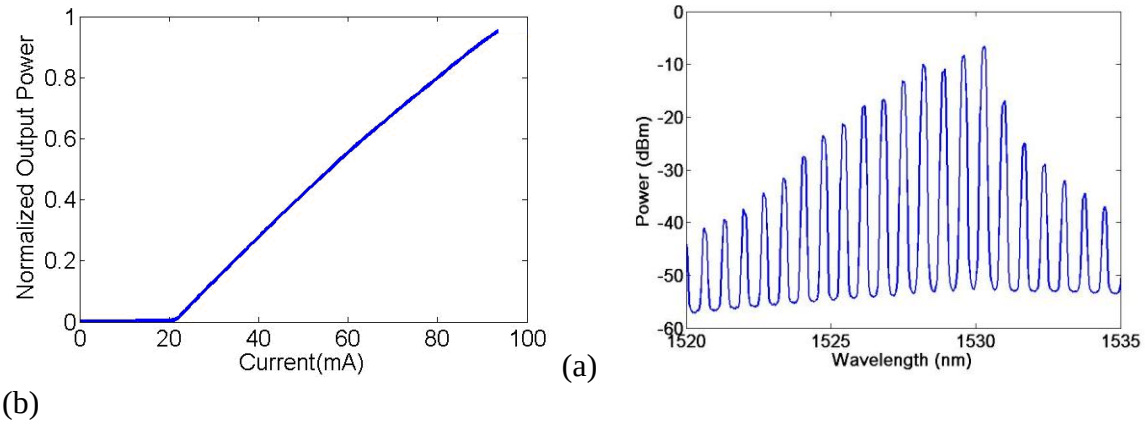

Fig. 3.9 LI curve (a) and spectrum (b) of FP laser.

The linewidth of each peak was measured by using a spectrum analyzer and the full width at half maximum (FWHM) of the peaks of the FP laser is about 50 MHz, corresponding to 0.4 pm at 1530 nm, or a Q-factor of 3.8×10^6. The peaks of FP laser are much sharper than the peaks of the ring (Q factor in the order of 10^4).

3.3.2 Fabrication and characterization of the ring resonator

The SOI ring resonator was fabricated by using conventional photolithography and inductively coupled plasma (ICP) etching using CF_4 chemistry. The height of the ridge waveguide is 40 nm. The perimeter of the ring is about 885 μm, corresponding to FSR $\Delta\lambda_{FSR_R} \approx 0.7nm$. The light is coupled from the bus waveguide to the ring by directional couplers. The waveguides are covered by Su-8 layer as upper cladding and a sensing window was opened on the top of the ring by photolithography to form a sample reservoir as shown in Fig. 3.10.

The fabrication process of the ring resonator as shown in Fig. 3.10 is described in detail as follows:

Process:
1) Photolithography to define the pattern 2) Dry etching to etch the waveguide (etching depth around 50nm) 3) Remove the photo resist by oxygen plasma 4) SU-8 photolithography to expose the sensing window 5) Combine with microfluidic chip (PDMS)
Backside thinning and cleaving

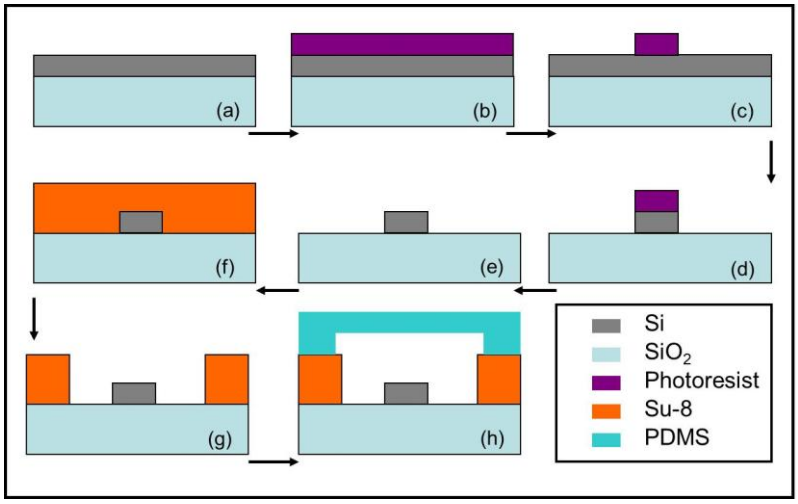

Fig. 3.10. The fabrication process of the ring resonator based on SOI.

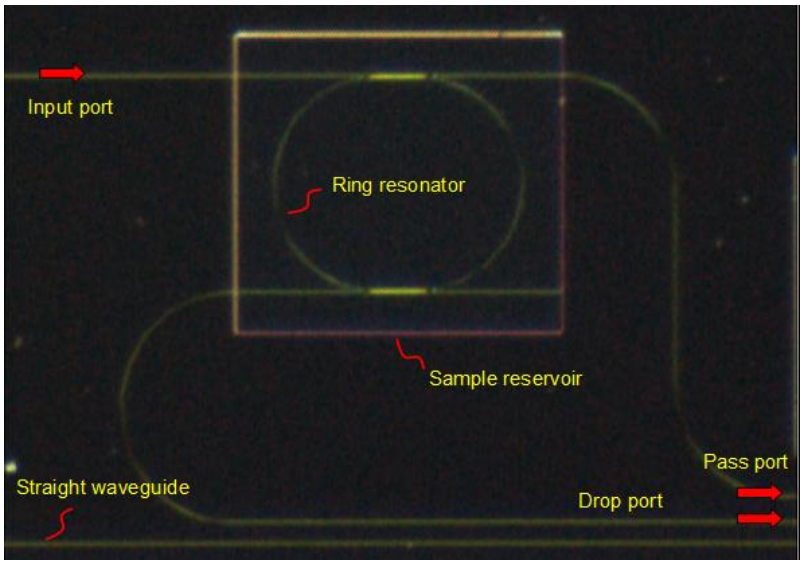

Fig. 3.11 Top view image of the single ring and bus waveguides by optical microscope.

Fig. 3.11 illustrates the final device of single ring resonator and the input/output bus waveguides. The microfluidic channel was omitted in this experiment for the simplicity of fabrication and measurement. We use tunable laser as the input source for the characterization of the ring. The output from the pass port or drop port can be collected by a microscope objective or lensed fiber.

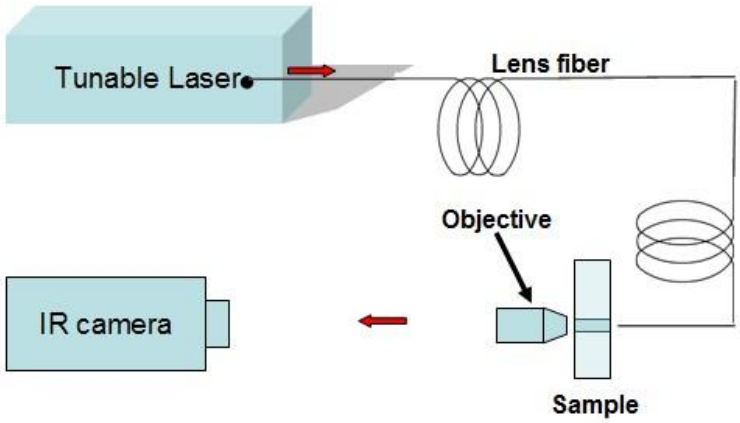

Fig. 3.12 The setup for output mode observation

The setup for observation of output optical mode is shown in Fig. 3.12. Here we use tunable laser from Agilent (Agilent 81600B) as input source. Lensed fiber is used to focus the light on the cleaved facet of the sample. At the output end, an objective (60 X) is used for the focusing and imaging of the output optical mode. Finally, the image is shown by an IR camera.

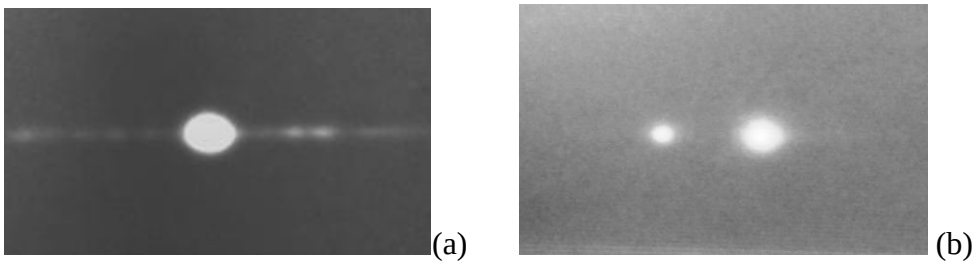

Fig. 3.13 (a) Optical mode of a straight waveguide. (b) Optical mode of the ring

Fig. 3.13 shows the image of optical mode. For the straight waveguide, we can see a bright output point as shown in Fig. 3.13(a). The ring resonator consists of two ports so we can see two output points as shown in Fig. 3.13(b). Changing the input wavelength we can see the power ratio between the pass port and drop port changes with different wavelengths. This is consistent with the transmission property of the ring resonator.

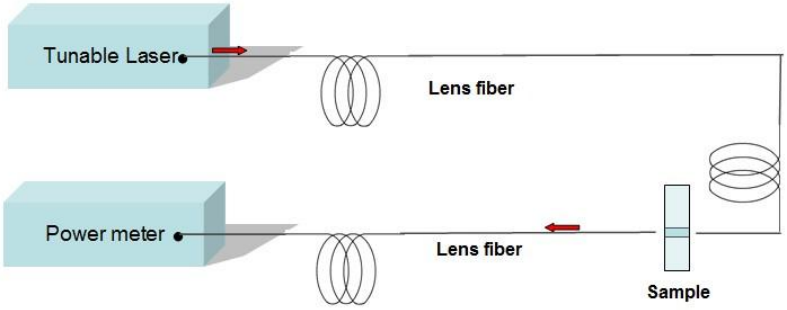

Fig. 3.14 The setup for transmission spectrum measurements

The setup for transmission spectrum measurements is shown in Fig. 3.14. Here we still use tunable laser from Agilent (Agilent 81600B) as the input source. Instead of a microscope objective, we use lensed fiber for output power collection. Finally, the output power is measured by power meter from Agilent (Agilent 81635A). The transmission of the ring resonator from the drop port is shown in Fig. 3.15.

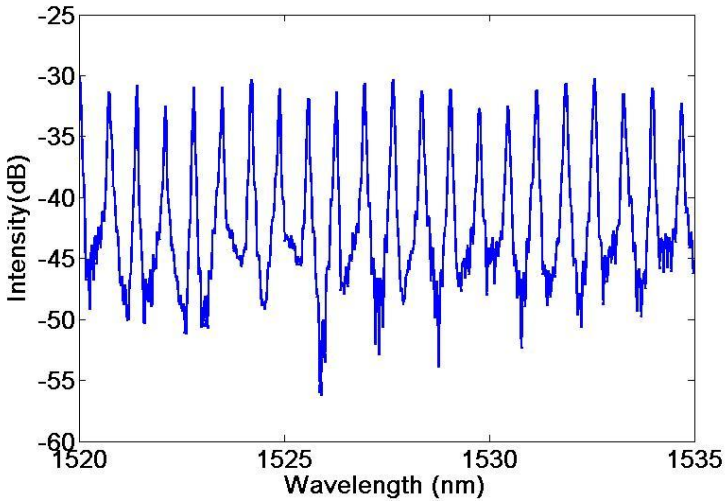

Fig. 3.15 Transmission spectrum from drop port of single ring

3.3.3 Measurements and discussions of the cascaded device

Fig. 3.16 shows the emission spectrum of the FP laser measured by an optical spectrum analyzer (OSA) and the transmission spectrum of the ring resonator measured by using a tunable laser as the source and a power detector. An FSR difference of less than 1 % was achieved between the ring and the FP laser. The center emission wavelength of the FP laser is 1528 nm and the FWHM of the power distribution function is about 3 nm.

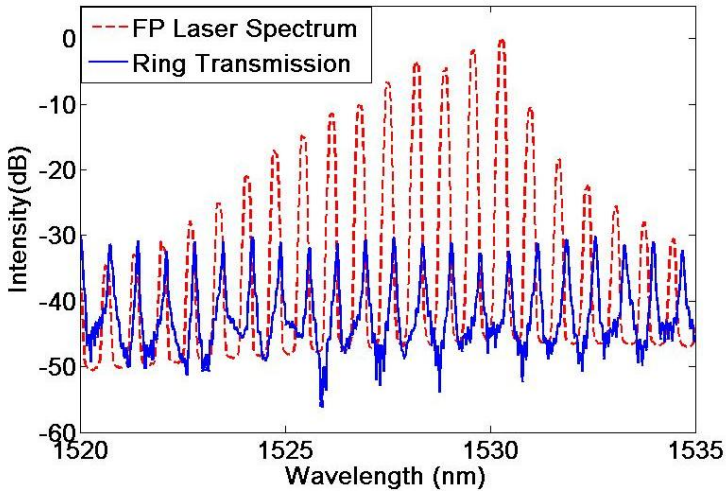

Fig. 3.16. FP laser spectrum (dashed curve) and the ring transmission spectrum (solid curve) showing almost identical FSRs.

To demonstrate the intensity interrogation scheme, the light from the FP laser was coupled into and out of the ring sensor by using lensed fibers as shown in Fig. 3.17. The coupling loss at each end is estimated to be about -10 dB. To compensate for the coupling loss, an erbium doped fiber amplifier (EDFA) was used to boost the power. Different concentrations of aqueous solution of NaCl were used as the analyte.

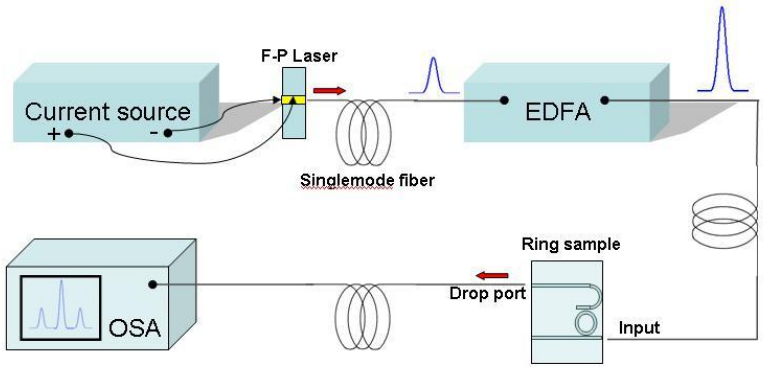

Fig. 3.17. Schematic of the experimental setup.

Fig. 3.18 shows the transmission spectra of the ring resonator measured using a tunable laser when the sensing ring was exposed to aqueous solutions of NaCl with different concentrations of 0 % and 4 %. The refractive index of an aqueous solution of NaCl varies with 0.0017~0.0018 RIU per mass % [18]. The wavelength shift sensitivity of the single ring is therefore about 22 nm/RIU.

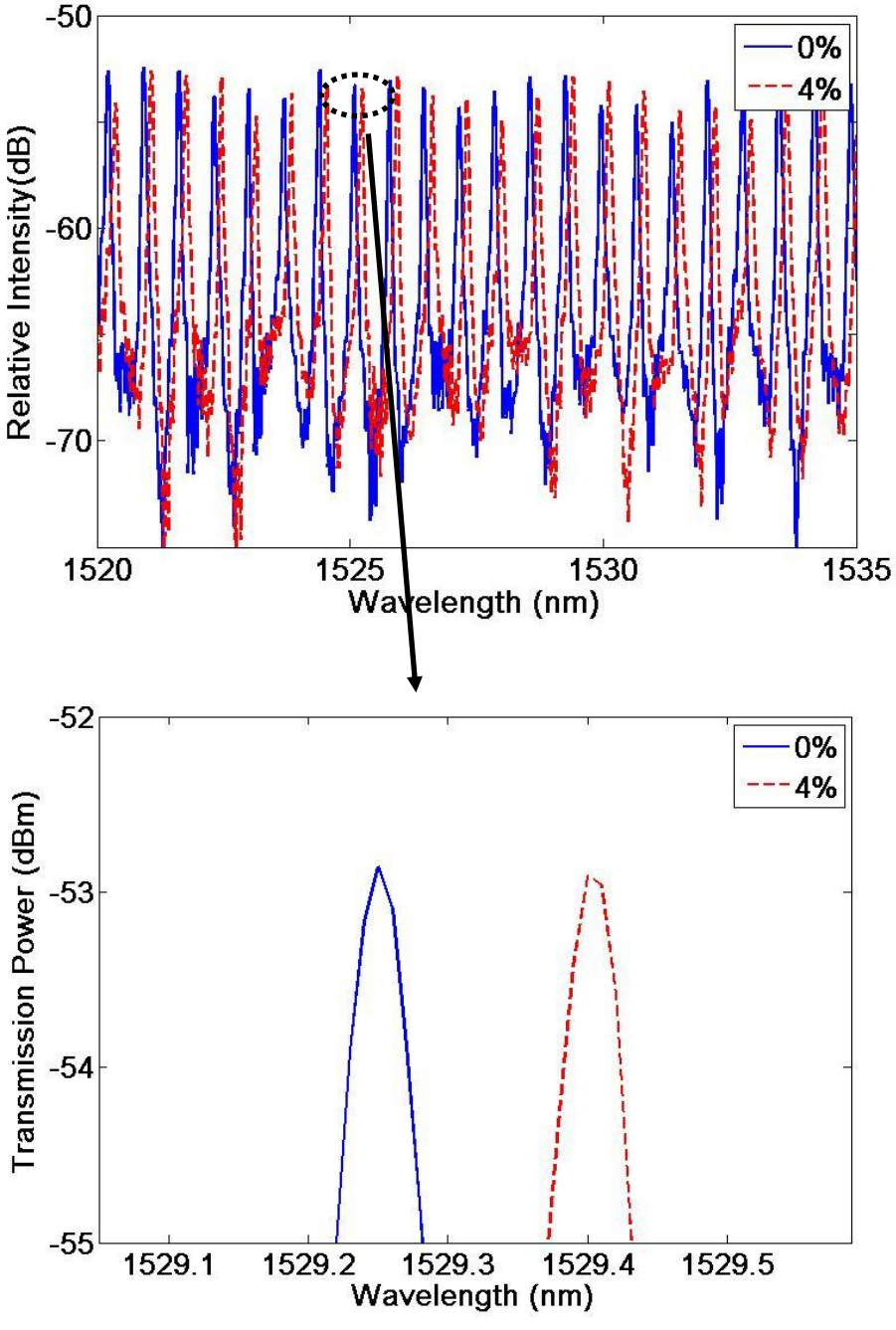

Fig. 3.18. Transmission spectra of the ring with different concentrations of NaCl solution.

Fig. 3.19 shows the measured output spectra of the sensor for different concentrations of NaCl solution of 0 %, 4 % and 8 % when the FP laser is used as the input source. During the setup, the current and temperature of the FP laser were adjusted so that the resonance peaks of the laser were well aligned with the peaks of the ring to obtain the maximum output power when the concentration of the NaCl solution is 0. The resonance peaks of the FP laser were fixed during the measurement. Therefore, the positions of the peaks in the output spectrum remained fixed while their magnitudes changes with the shift of the

transmission peaks of the ring resonator when the concentration of the NaCl solution increases.

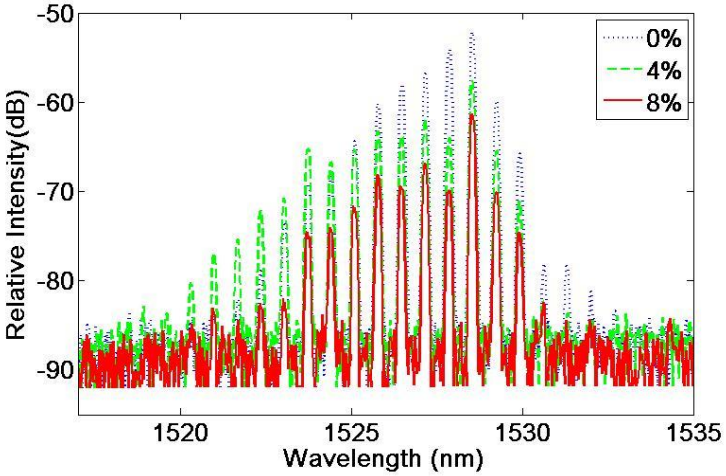

Fig. 3.19. Output spectra of the sensor based on cascaded FP laser and ring resonator with different concentrations of NaCl solution.

Fig. 3.20 shows the normalized output power versus the sample refractive index change of the aqueous solutions of NaCl of different concentrations. The power out of the EDFA was monitored during the measurement as a reference. By fitting the measured data with theoretical calculation, we obtained the actual Q factor of the single-ring of about 1.1×10^{4}. This corresponds to a coupling coefficient between the ring and the bus waveguides of 43 %, assuming that the propagation loss is 1 dB/cm and the FSRs of the ring and the F-P cavity are 0.7 nm and 0.693 nm, respectively. The sensitivity of the sensor reaches about 1000 dB/RIU. This is more than twice that of the cascaded double-ring sensor reported in [11], which was fabricated from the same wafer as the single ring resonator used in the current experiment. This sensitivity is also much higher than that of the intensity interrogated SPR sensors [4]. Note that while the transmission spectrum usually exhibits irregular measurement noises, they are averaged out in the integrated power measurement. Assuming that the relative power measurement accuracy is 0.01 dB (achievable with an Agilent power sensor, for example), the detection limit for the refractive index variation is 1×10^{-5}.

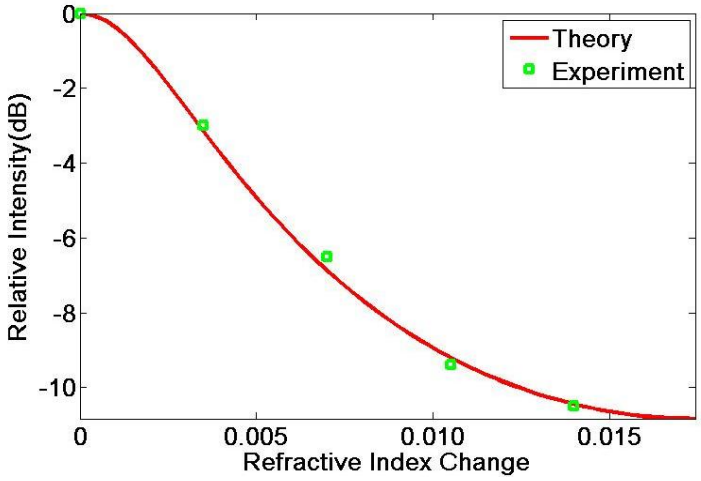

Fig. 3.20. Normalized output power versus refractive index change of aqueous solutions of NaCl.

This preliminary experimental result is expected to be improved by optimizing the coupling coefficient between the ring and the bus waveguides to increase the Q-factor of the ring resonator. Due to the high spectral power density of the FP laser, the sharper resonance peaks of the ring can result in a higher sensitivity without degrading the output power. Our theoretical analysis shows that the sensitivity can reach 5000 dB/RIU by decreasing the coupling coefficient from 40 % to 10 %. Besides, by using a deep-etched rib waveguide with narrower width, which can be patterned by electron beam lithography, the propagation loss for the TM mode can be reduced drastically and the sensor can operate in TM mode with the sensitivity improved by an order of magnitude as compared to the TE mode. This will lead to a refractive index detection limit of about 2×10^{-7}.

For comparison, a wavelength interrogated sensor based on monitoring the wavelength shift of the resonance peak of a ring resonator or the reflection peak of a fiber Bragg grating typically has a sensitivity in the order of 100 nm/RIU [7]. This corresponds to a refractive index detection limit of 10^{-5}, assuming a wavelength measurement accuracy of 1 pm.

It should be pointed out that although a discrete FP laser is used in the proof-of-principle experiment presented in this work, it can be replaced by a heterogeneously integrated ring or FP laser with cavity length more accurately defined by photolithography. Compared to all-passive cascaded double-ring sensor, the integration of a laser on the sensor chip will eliminate the need for an external light source and fiber coupling, thus resulting in more compact, robust and low-cost devices. By using a 1xN splitter integrated with N ring resonators, the FP laser can be shared by a large array of ring sensors for parallel processing.

3.4 Conclusion

In summary, we have investigated theoretically and experimentally a highly-sensitive intensity-interrogated waveguide biosensor based on cascaded FP laser and SOI ring

resonator. The detection scheme employs a low-cost easy-to-fabricate FP laser to serve as a reference comb for the sensing ring. Its sharp emission peaks with high spectral power density results in a high sensitivity for the sensor compared to previously investigated all-passive double-ring sensor. No tunable laser or high-resolution spectrometer is required. Preliminary experiments have demonstrated the operation principle with a sensitivity of 1000 dB/RIU, more than twice that of the double-ring sensor. The sensitivity can be improved by an order of magnitude by using TM mode in SOI waveguide platform. Due to the much higher spectral power intensity of the FP laser compared with a broadband source such as an LED, the coupling coefficient between the ring and the waveguide can be reduced to increase the Q-factor without significantly degrading the output power. Theoretically, an ultrahigh sensitivity in the order of 5×10^{4} dB/RIU can be achieved with TM mode and 10 % coupling coefficient between the waveguide and the ring, corresponding to a refractive index detection limit of about 2×10^{-7}. With the advancement of III-V on silicon integration technology and micro-fluidics, the sensing scheme can be extended to large array format for lab-on-a-chip applications.

Reference

[1] K. Matsubara, S. Kawata, and S. Minami, "Optical chemical sensor based on surface plasmon measurement," Appl. Optics, 27, 1160-1163, 1988.

[2] A. K. Sharma, R. Jha, B. D. Gupta, "Fiber-optic sensors based on surface plasmon resonance: a comprehensive review," IEEE Sens. J., 7, 1118-1129, 2007.

[3] X. Ma, X. Xu, Z. Zheng, K. Wang, Y. Su, J. Fan, R. Zhang, L. Song, Z. Wang, J. Zhu, "Dynamically modulated intensity interrogation scheme using waveguide coupled surface plasmon resonace sensors," Sens. Actuators A: Physical, 157, 9-14, 2010.

[4] A. Cattoni, P. Ghenuche, A.-M. Haghiri-Gosnet, D. Decanini, J. Chen, J.-L. Pelouard, and S. Collin, "λ3/1000 plasmonic nanocavities for biosensing fabricated by soft UV nanoimprint lithography," Nano Lett., 11, 3557-3563, 2011.

[5] A. Densmore, D.-X. Xu, P. Waldron, S. Janz, P. Cheben, J. Lapointe, A. Delâge, B. Lamontagne,J. H. Schmid, and E. Post, "A Silicon-on-Insulator Photonic Wire Based Evanescent Field Sensor," IEEE Photon. Technol. Lett., 18, 2520-2522, 2006.

[6] A. Densmore, D.-X. Xu, S. Janz, P. Waldron, T. Mischki, G. Lopinski, A. Delâge, J. Lapointe,P. Cheben, B. Lamontagne, and J. H. Schmid, "Spiral-path high-sensitivity silicon photonic wire molecular sensor with temperature-independent response," Opt. Lett., 33, 596-598, 2008.

[7] K. De Vos, I. Bartolozzi, E. Schacht, P.r Bienstman1, R. Baets, "Silicon-on-Insulator microring resonator for sensitive and label-free biosensing," Opt. Express, 15, 7610-7615, 2007.

[8] T. Claes, W. Bogaerts and P. Bienstman, "Vernier-cascade label-free biosensor with integrated arrayed waveguide grating for wavelength interrogation with low-cost broadband source," Opt. Lett., 36, 3320-3322, 2011.

[9] D.-X. Xu, A. Densmore, A. Delâge, P. Waldron, R. McKinnon, S. Janz, J. Lapointe, G. Lopinski, T. Mischki, E. Post, P. Cheben and J. H. Schmid, "Folded cavity SOI microring sensors for high sensitivity and real time measurement of biomolecular binding," Opt. Express, 16, 15137-15148, 2008.

[10] L. Jin, M. Li, and J.-J. He, "Highly-sensitive silicon-on-insulator sensor based on two cascaded micro-rings resonator with vernier effect," Opt. Commun., 284, 156-159, 2011.

[11] L. Jin, M. Li, and J.-J. He, "Optical waveguide double-ring sensor using intensity interrogation with a low-cost broadband source," Opt. Lett., 36, 1128-1130, 2011.

[12] S. S. Saini, C. Stanford, S. M. Lee, J. Park, P. DeShong, W. E. Bentley, M. Dagenais, "Monolayer detection of biochemical agents using etched-core fiber bragg grating sensors," IEEE Photon. Technol. Lett., 19, 1341-1343, 2007.

[13] P. Cheben, J. H. Schmid, A. Delâge, A. Densmore, S. Janz, B. Lamontagne, J. Lapointe, E. Post, P. Waldron, and D.-X. Xu, "A high-resolution silicon-on-insulator arrayed waveguide grating microspectrometer with sub-micrometer aperture waveguides," Opt. Express, 15, 2299-2306, 2007.

[14] J. Mohr, B. Anderer, and W. Ehrfeld, "Fabrication of a planar grating spectrograph by deep-etch lithography with synchrotron radiation," Sens. Actuators A, 27, 571-575, 1991.

[15] M. A. Webster, R. M. Pafchek, A. Mitchell, and T. L. Koch, "Width dependence of inherent TM-mode lateral leakage loss in silicon-on-insulator ridge waveguide," IEEE Photon. Technol. Lett., 19, 429-431, 2007.

[16] A. W. Fang, H. Park, O. Cohen, R. Jones, M. J. Paniccia, and J. E. Bowers, "Electrically pumped hybrid AlGaInAs-silicon evanescent laser," Opt. Express, 14, 9203-9210, 2006.

[17] G. Roelkens, D. Van Thourhout, R. Baets, R. Nötzel, and M. Smit, "Laser emission and photodetection in an InP/InGaAsP layer integrated on and coupled to a Silicon-on-Insulator waveguide circuit," Opt. Express, 14, 8154-8159, 2006.

[18] CRC Handbook of Chemistry and Physics, edited by David R. Lide, (90th Edition CD-ROM Version 2010).

CHAPTER 4

Design and analysis of temperature compensation in waveguide sensors

In Chapter 3, we have demonstrated a sensor based on cascaded ring and FP laser using intensity interrogation. Compared to cascaded double-ring sensor, the sensitivity is improved due to the sharp peaks and higher spectral power density of FP laser. Further to the proof-of-principle experiment, there are several issues that need to be resolved.

First, we have to control the temperature of the sensing ring to eliminate the transmission shift caused by temperature fluctuation. Second, the wavelength of the FP laser must be well stabilized during the measurements. These additional controlling modules add much more cost to the whole device. To resolve the two stability problems, another improved scheme using the same building blocks is proposed and analyzed in this chapter.

The stability and temperature compensation have been realized by using on-chip temperature referencing [1-3]. The combination of this approach and intensity interrogation can greatly simplify the device with temperature compensation. We only used two rings to maintain the stability of the laser and compensate the influence of the temperature fluctuation at the same time. It provides a simple scheme on design, fabrication and interrogation for full-integration and stability controlling of optical sensor.

In this chapter, we will illustrate this improvement scheme and analysis the system sensitivity with temperature compensation. The FP laser source could be replaced with single-mode laser allowing design flexibility at the cost of fabrication complexity. At last, the effect of waveguide loss is discussed especially the case of high loss waveguide providing a guide for transplanting the same idea to other material system.

4.1 The structure of the sensor

In this section, the basic structure and working principle are illustrated. The most part of this design is from the legacy of last chapter. We still use semiconductor laser and ring resonator as the building blocks. Intensity interrogation is implemented by integrated photodetectors.

4.1.1 Basic principle and transmission spectrum

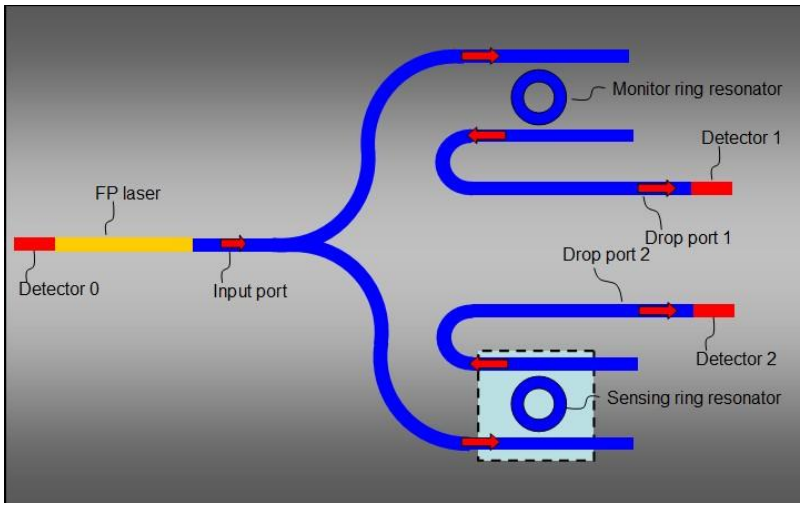

Fig. 4.1. Schematic of the cascaded FP cavity laser and micro-ring resonator sensor.

As shown in Fig. 4.1, the sensor consists of a FP laser as the source. The output power of the laser is monitored by Detector 0. The input light is spitted into two arms. One arm is coupled with monitor ring and the output power through drop port 1 is detected by detector 1. The second arm is coupled with sensing ring and the output power through drop port 2 is detected by detector 2. It should be mentioned that the scheme can also work with the FP laser replaced by a single-mode laser, but the latter requires more complicated fabrication process.

All the passive ring resonators are based on SOI because it is a material system with many advantages for this application, including its high index contrast that allows small footprint and the incorporation of many sensors on a chip to simultaneously measure multiple parameters. Moreover it permits low cost, high quality and reliable fabrication with CMOS-compatible processes. The laser diode can be fabricated on InP material system as described in last Chapter.

4.1.2 Working principle of the device

It should be noted that in a practical device, the output power and central wavelength of the laser are not stable without additional complicated and expensive control systems. Besides, the transmission spectrum of the sensing ring shifts with temperature fluctuation of the environment. Therefore, they are all functions of time. Here we use a monitor ring to keep the central wavelength of the laser shift in synchronization with the change of the transmission spectrum of the monitoring ring, thus eliminating the effect of temperature instability on the sensing ring.

Since the highest sensitivity is obtained when the FSRs of FP laser and ring resonators are exactly the same as discussed in last chapter and in the case of cascaded FP laser and ring,

the effect of the difference of FSRs is not critical as shown in Fig. 3.4, for simplicity, in this chapter we assume the FSRs of laser and rings are the same.

As shown in Eq. (3.1), the output power distribution $P_{\mathrm{L}}(\lambda)$ of the multimode FP laser source can be written as the product of a spectral power distribution function $P_G(\lambda)$ which is related to the material gain, and a periodic comb function $C_L(\lambda)$ corresponding to the resonance peaks of the FP cavity. In this chapter, we take the fluctuation into consideration and consider the time t as another parameter. The output power distribution of the FP laser source is written as $P_{\mathrm{L}}(\lambda,t)$.

The sensing ring and monitor ring are of the same waveguide structure and satisfy the following resonance equation

$$m\lambda = 2\pi R n_{eff} \tag{4.1}$$

Here R is the radius of the ring, n_{eff} is the effective index of the ring and m is an integer. λ is the resonance wavelength. From Eq. (4.1), we can get

$$\frac{\Delta\lambda}{\lambda} = \frac{\Delta n_{eff}}{n_g} \tag{4.2}$$

where Δn_{eff} is the shift of the effective index of the ring, n_g is group index of the waveguide and $\Delta\lambda$ is the shift of the wavelength due to the shift of the effective index. Δn_{eff} , n_{eff} and n_g are determined by the waveguide transverse structure and the environmental change of the waveguide and not related to the length of the ring. If the waveguide structure is the same for the two rings, $\Delta\lambda$ will be the same under the same environment.

The power of the laser is given by

$$P_L(t) = \int_0^\infty P_L(\lambda,t)d\lambda \tag{4.3}$$

Detector 0 is used to monitor the power of the laser and we denote it as $P_0(t)$. Similarly, the output of detector 1 and 2 are $P_1(t)$ and $P_2(t)$ respectively.

The power of the drop port of monitoring ring and the sensing ring can be respectively written as

$$P_{monitoring}(t) = \int_0^\infty [P_L(\lambda,t)T_{monitoring}(\lambda,t)]d\lambda \tag{4.4}$$

$$P_{sensing}(t) = \int_0^\infty [P_L(\lambda,t)T_{sensing}(\lambda,t)]d\lambda \tag{4.5}$$

Here $T_{monitoring}(\lambda,t)$ and $T_{sensing}(\lambda,t)$ are the transmission of the monitoring ring and sensing ring, respectively. $P_0(t)$, $P_1(t)$ and $P_2(t)$ are proportional to $P_L(t)$, $P_{monitoring}(t)$ and $P_{sensing}(t)$ respectively. So we have

$$C_0 = \frac{P_0(t)}{P_L(t)} \tag{4.6}$$

$$C_1 = \frac{P_1(t)}{P_{monitoring}(t)} \tag{4.7}$$

$$C_2 = \frac{P_2(t)}{P_{sensing}(t)} \tag{4.8}$$

where C_0, C_1 and C_2 are constants which depend on the response of the detector.

As shown in Fig. 4.2(b), the resonance peaks of the sensing ring transmission spectrum is aligned with the comb function $C_L(\lambda)$ of the laser at time t_0.

The resonance peaks of the laser is located at the slope of the monitoring ring peaks as shown in Fig. 4.2(a) at time t_0. To maintain high accuracy of the stability control, the slope at the position P_{t0} should be the largest slope of the monitoring ring peak at the central wavelength of the spectral power distribution function $P_G(\lambda)$ of the FP laser. The power ratio of $P_1(t)$ to $P_0(t)$ at time t_0 is $C_{monitoring} = \frac{P_1(t_0)}{P_0(t_0)}$.

$C_{monitoring}$ is determined by the relative position of the spectrum of the laser and the monitoring ring transmission spectrum. When the analyte is detected at time t_1, adjust the spectrum of the laser and maintain $\frac{P_1(t_1)}{P_0(t_1)} = C_{monitoring}$ to compensate the shift of the transmission spectrum of the rings as $\Delta\lambda_1$ shown in Fig. 4.2(a).

At the same time, $P_2(t_1)$ is noted to reflect the real shift caused by refractive index change from the analyte detection, as $\Delta\lambda_2$ shown in Fig. 4.2(a). We can get from Eqs. (4.6) and (4.8), $\frac{P_2(t_1)}{P_0(t_1)} = (\frac{C_2}{C_0})\frac{P_{sensing}(t_1)}{P_L(t_1)}$.

From Eq. (4.2), we can get

$$\frac{\Delta n}{\Delta\lambda} = \frac{n_g}{S\lambda} \tag{4.9}$$

where S is the ratio of the change in the waveguide effective refractive index to the change of the analyte refractive index, which is determined by the transverse structure of the waveguide. Δn is the index change of the analyte.

For the sensing ring, we can get

$$\frac{\Delta P_2}{\Delta \lambda} = \frac{dP_2}{d\lambda} \tag{4.10}$$

From Eqs. (4.9) and (4.10), when ΔP_2 equals to the minimum detectable power difference $\Delta P_{\min}$ we can get the detection limit of the sensing ring is

$$\Delta n_{\min-sensing} = \frac{n_g \Delta P_{\min}}{S\lambda} / \max(\frac{dP_2}{d\lambda}) \tag{4.11}$$

$\max(\frac{dP_2}{d\lambda})$ is the max slope of the sensing ring peak.

At the initial point of P_{t0}, we can get

$$\frac{\Delta P_1}{\Delta \lambda} = \left.\frac{dP_1}{d\lambda}\right|_{P_{t0}} \tag{4.12}$$

Here $\left.\frac{dP_1}{d\lambda}\right|_{P_{t0}}$ is the slope at the point P_{t0} as shown in Fig. 4.2 (a). When ΔP_1 equals to the minimum detectable power difference $\Delta P_{\min}$ we can get the instability limit of the wavelength from Eq. (4.12) as

$$\Delta \lambda_{instability} = \Delta P_{\min} / (\left.\frac{dP_1}{d\lambda}\right|_{P_{t0}}) \tag{4.13}$$

The instability of wavelength can result in an error in the sensing ring. From Eqs. (4.9) and (4.13), we can achieve the refractive index error of the sensing ring as

$$\Delta n_{instability} = \frac{n_g \Delta P_{\min}}{S\lambda} / (\left.\frac{dP_1}{d\lambda}\right|_{P_{t0}}) \tag{4.14}$$

The detection limit of the sensing ring is related to the slope of its resonance peak and the stability of the wavelength of laser depends on the slope of the monitoring ring at the initial point. The detection limit of the system can be written as

$$\Delta n_{system} = \Delta n_{instability} + \Delta n_{\min-sensing} \tag{4.15}$$

From Eq. (4.14), the optimized initial position of P_{t0} as shown in Fig. 4.2 (a) should be equal to the maximum slope of the monitoring ring peak as

$$\left.\frac{dP_1}{d\lambda}\right|_{P_{t0}} = \max(\frac{dP_1}{d\lambda}) \tag{4.16}$$

In the condition of Eq. (4.16), Eq. (4.14) can be written as

$$\Delta n_{instability} = \frac{n_g \Delta P_{\min}}{S\lambda} / \max(\frac{dP_1}{d\lambda}) \tag{4.17}$$

From Eqs. (4.11) and (4.17), Eq. (4.15) can be written as

$$\Delta n_{system} = \frac{n_g \Delta P_{\min}}{S\lambda} (1/\max(\frac{dP_2}{d\lambda}) + 1/\max(\frac{dP_1}{d\lambda})) \tag{4.18}$$

When the system works at the optimized situation which means the steepness at P_{t0} is the maximum of the monitoring ring peak. In this case, the sharpness of the monitoring ring and the sensing ring plays the equivalent role in the determination of the detection limit of the system according to the Equation (4.18). The best way is therefore to design and fabricate the two rings with same parameters. And the detection limit of the system is double of the detection limit of a single ring.

For the intensity interrogation, only half period of FSR can be used in order to uniquely determine the refractive index change. Therefore, the measurement range of the refractive index change is given by

$$\Delta n_{\max} = \frac{1}{2S} \times \lambda n_g / 2\pi R n_g = \frac{1}{2S} \times \lambda / 2\pi R \tag{4.19}$$

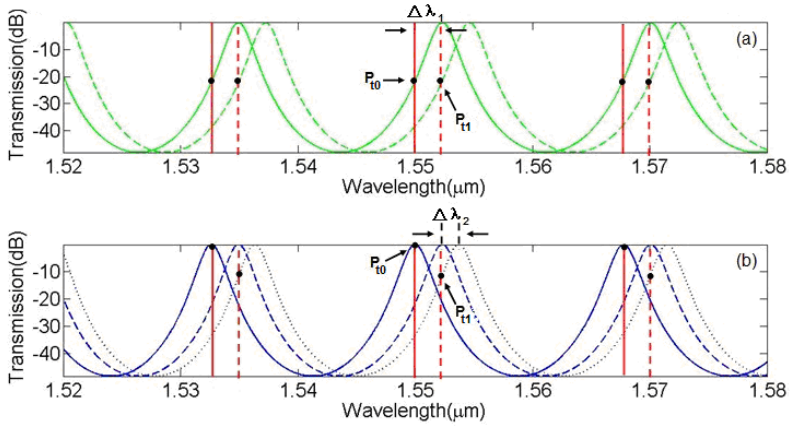

Fig. 4.2. (a) The transmission of monitoring ring at time t_0 (solid curve in green) and time t_1 (dashed curve in green). The laser spectrum at time t_0 (solid line in red) and time t_1 (dashed line in red). P_{t0} and P_{t1} is the working point at time t_0 and time t_1.2(b) The transmission of sensing ring at time t_0 (solid curve in blue) and time t_1 (dotted curve in blue). The dashed curve is the transmission spectrum caused by environmental instability.

4.2 Simulation results and discussion

In this section, the ring and laser components are described in detail. The simulation is performed and the sensitivity of the system is discussed.

4.2.1 Components description

We consider the passive part of the sensor is on SOI platform with 260 nm-thick silicon layer (with a refractive index of 3.48) on a 2 μm-thick SiO_2 (refractive index of 1.44) buried oxide layer. Silicon nanowire waveguides with a width of 450 nm are used in the ring resonators. This platform is widely used by many groups. A straight waveguide with a loss of around 4 dB/cm and a negligible bending loss of as small as 5 μm radius have been demonstrated for operation in TM mode [4, 5]. In the following calculation, the loss of the ring is assumed to be 5 dB/cm. The system is operated in TM mode because of its higher sensitivity. The ratio of the change in the waveguide effective refractive index to the change of the analyte refractive index reaches to 25 % in this case. The effective refractive index of the waveguide in the ring resonator is calculated by $n(\lambda) = n_g - 1.5\times10^6 \lambda$ (with n_g =4.35).

The FP laser is easy to fabricate. The wavelength can be controlled by the temperature with a typical coefficient of 0.5 nm/℃. The thermo-optic coefficient (*dn/dT*) of silicon [6] and silica [7] at 1.5 μm and room temperature (295K) is 1.87×10^{-4} and 8.45×10^{-6}, respectively. The corresponding thermo-optic coefficient of the effective index of the waveguide (d_{neff}/d_T) is around 2×10^{-4} and according to Eq. (4.2), we can get

$$\frac{\Delta\lambda}{\Delta T} = (\lambda / n_g)\frac{\Delta n_{eff}}{\Delta T} \tag{4.20}$$

The temperature coefficient of the wavelength (d_λ/d_T) is 0.0713 nm/℃. The 1 nm turning range of the laser can cover around 14 ℃ temperature change of the rings. Hence, no accurate temperature controlling is required for the operation of the system.

4.2.2 Simulation analysis

The Q factor of the ring resonator changes with the intensity coupling coefficient *K* and the length of the cavity at a given loss value as shown in Fig. 4.3. When the radius of the ring is smaller, the Q factor is more sensitive to the *K* value. To use a smaller ring the *K* value must be well controlled to achieve high Q factor.

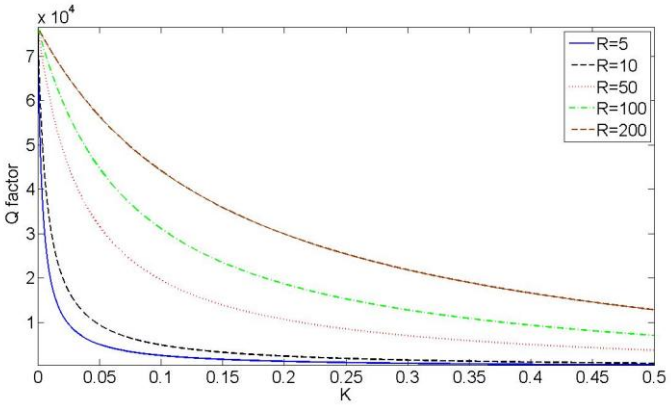

Fig. 4.3 Q factor versus intensity coupling coefficient, with the radius of the ring as a parameter.

It should be noted that the smaller *K* results in a degradation of output power at the same time. The transmission spectrum is calculated with different *K* value as shown in Fig. 4.4. The radius of the ring is set to be 100 μm and the length of the laser is around 335 μm. In this case, the maximum measurement range reaches 4.94×10^{-3} according to Eq. (4.19). Here we can see a *K* value as low as 0.005 can results in ~25 dB decrease at the peak wavelength which can highly degrade the performance of the sensor by intensity interrogation even if the Q factor reaches 7.16×10^{4}. The Q factor reaches 3.15×10^{4} with *K*=0.1 and in this case the intensity decrease is only ~5 dB. The high Q factor comes with high intensity decay. We take *K*=0.1 as an example for the following analysis.

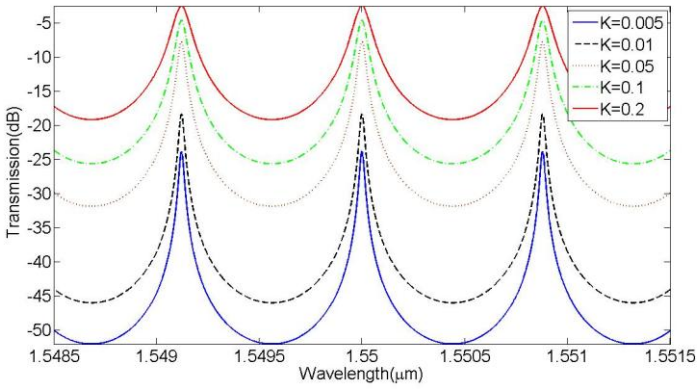

Fig. 4.4 The transmission spectrum of the ring (r=100μm) versus wavelength, with the intensity coupling coefficient as a parameter.

The output power ratio from the drop port of the sensing ring is calculated as shown in Fig. 4.5. Apparently, the sensitivity decreases with the increase of *K* value. When *K*=0.1, the sensitivity of the sensor reaches 1.5×10^{4} dB/RIU.

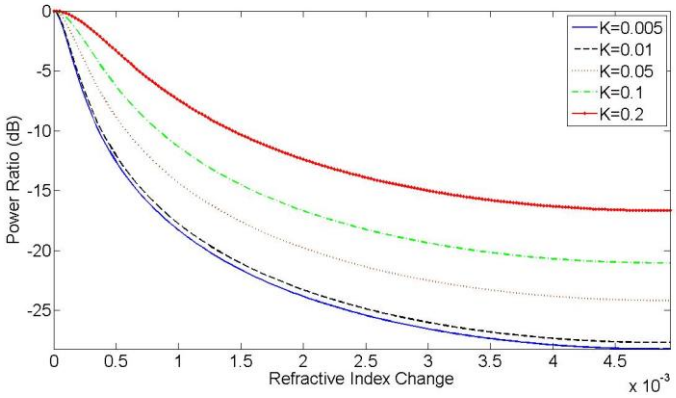

Fig. 4.5 The power ratio versus refractive index change, with the intensity coupling coefficient as a parameter (r=100 μm).

Assuming the minimal detectable power ratio variation is 0.01 dB, the detection limit of the sensing ring can reach 6.67×10^{-7} when *K*=0.1, which corresponds to a wavelength

shift of around 0.06 pm of the sensing ring. The detection limit is equivalent to a temperature change of 8.57×10^{-4} ℃ of the ring and 1.20×10^{-4} ℃ of the FP laser.

The monitor ring is of the same parameter and the system works on optimized condition as mentioned before. The detection limit of the system is double of the detection limit of the sensing ring, reaching 1.33×10^{-6}. The detection limit is related to the Q factor and can be improved by increasing the radius of the rings or decrease the *K* value as shown in Fig. 4.3. A larger ring with the same *K* value can have better sensitivity at the cost of reduced detection range and output power.

The scheme with FP laser as the source sets limitation on the size of the ring because the FSRs of the ring and the laser should be roughly the same. It is hard to fabricate ultra-short FP laser to match small rings. For example, the length of FP laser should be around 16 μm when the radius of ring is 5 μm. For some applications when smaller rings are favorable (i.e. fabricated on expensive or lossy material system), single-mode laser is an alternative source.

For example, the radius of the ring is set to be 5 μm which can be realized on SOI. The transmission spectrum is calculated with different K value as shown in Fig. 4.6. In this case, the maximum measurement range reached 9.87×10^{-2} according to Eq. (4.19). Here we can see a *K* value as low as 0.005 can results in only ~5 dB decrease at the peak wavelength and the Q factor reaches 3.25×10^{4} in this case.

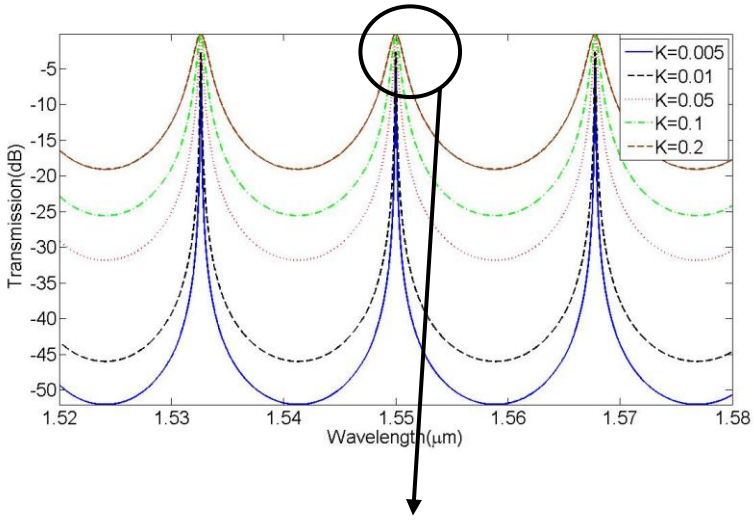

(a)

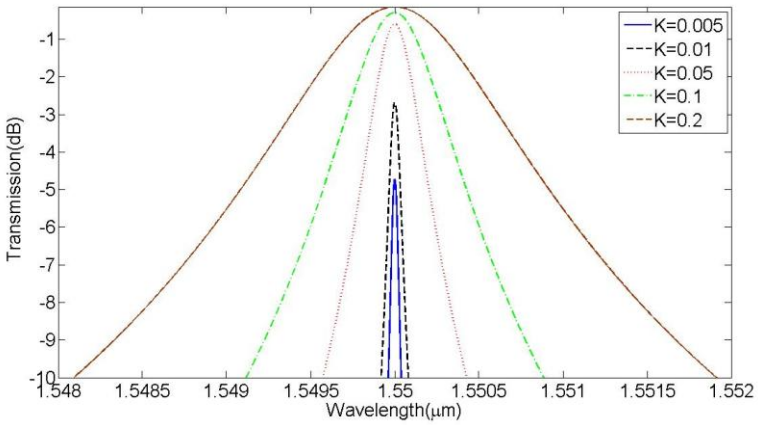

(b)

Fig. 4.6 The transmission spectrum of the ring (r=5 μm) versus wavelength, with the intensity coupling coefficient as a parameter.

The output power ratio from the drop port of the sensing ring is calculated as shown in Fig. 4.7. Apparently, the sensitivity decreases with the increase of *K* value. When *K*=0.005, the maximum sensitivity of the sensor reaches 10^4 dB/RIU. The detection limit of sensing ring can reach 9.52×10^{-7} when *K*=0.005 which corresponds to a wavelength shift of around 0.085 pm of the sensing ring. The detection limit is equivalent to a temperature change of 1.21×10^{-3} ℃ of sensing ring.

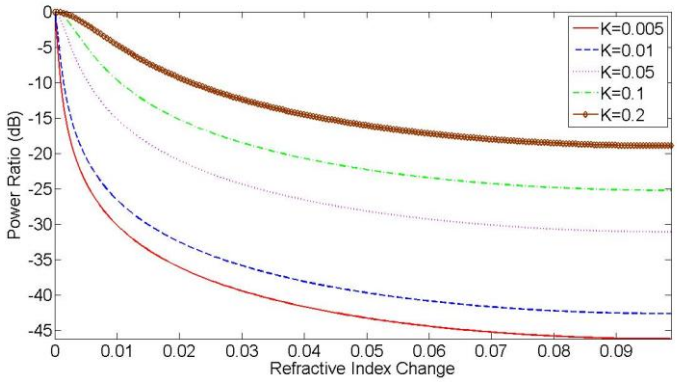

Fig. 4.7 The power ratio versus refractive index change, with the intensity coupling coefficient as a parameter (r=5 μm).

4.3 Effect of waveguide loss

We have analyzed a novel structure based on MRR and easy-to-fabricate FP laser using intensity interrogation which is suitable for integration and large-array fabrication. This scheme offers compensation of the fluctuation of environmental temperature and the wavelength drift of laser diode with no addition fabrication process and complex interrogation. However, the analysis is based on a typical loss value of advanced SOI

fabrication process. In this section we make a more detailed analysis on the effect of optical loss.

4.3.1 Analysis of the Q factor

Thanks to the advanced and reliable fabrication techniques based on SOI, the loss of the waveguide can be in the order of dB/cm. As shown in Fig. 4.8, the Q factor decreases with an increasing loss value. The maximum Q factor of 5μm radius ring for loss value of 100 dB/cm, 50 dB/cm, 10 dB/cm, 5 dB/cm is 3.83×10^3, 7.66×10^3, 3.83×10^4, 7.64×10^4, respectively.

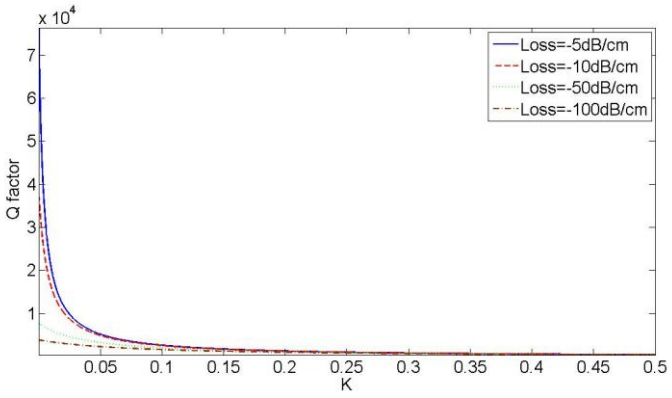

Fig. 4.8 Q factor versus K value with the loss as a parameter. The radius of the ring is 5 μm.

Fig. 4.9 shows the Q value for a ring with radius of 100μm. The maximum Q factor of 100μm radius ring for loss value of 100 dB/cm, 50 dB/cm, 10 dB/cm, 5 dB/cm is 3.51×10^3, 7.49×10^3, 3.83×10^4, and 7.66×10^4, respectively. The maximum Q factor is very similar as the smaller ring. However, from Fig. 4.8 and Fig. 4.9, to achieve the same Q value, a smaller *K* value is required for smaller ring .

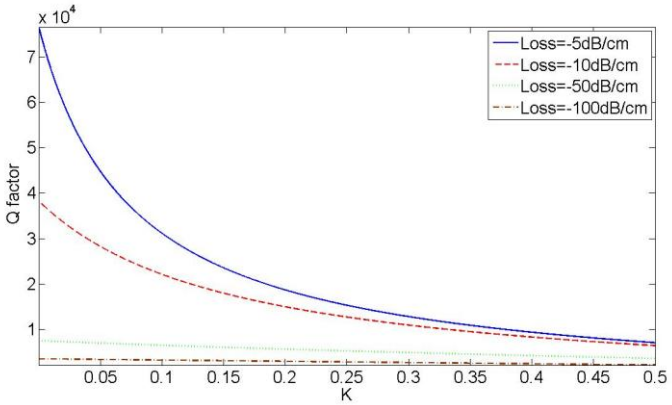

Fig. 4.9 Q factor versus K value with the loss as a parameter. The radius of the ring is 100 μm.

4.3.2 Analysis of the intensity of the transmission

The Q value also relays on *K* value as mentioned in chapter 2. To obtain a higher Q value, a smaller *K* value is required. But the intensity decreases with a decreasing *K* value as shown in Fig. 4.4 and Fig. 4.6. For a larger ring and high-loss waveguide, the intensity degrade is much larger.

Fig. 4.10 shows the transmission of ring with a radius of 50 μm and a loss of 5 dB/cm. The intensity degradation for K value of 0.2, 0.1, 0.05, 0.01 and 0.005 is -1.31 dB, -2.58 dB, -4.64 dB, -13.3 dB and -18.3 dB respectively.

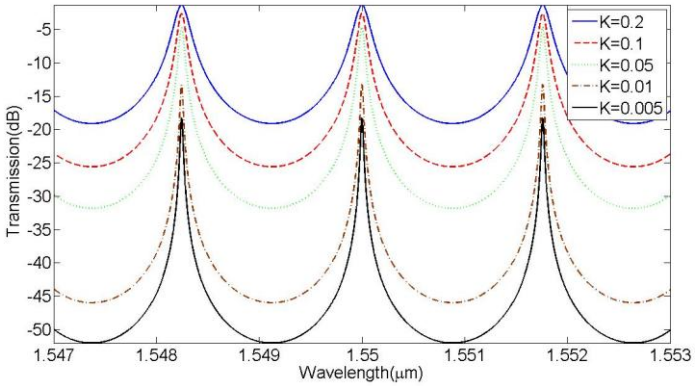

Fig. 4.10 transmission of the ring with radius of 50 μm and loss of 5 dB/cm.

Fig. 4.11 shows the transmission of ring with a radius of 50 μm and a loss of 100 dB/cm. The intensity degradation for *K* value of 0.2, 0.1, 0.05, 0.01 and 0.005 is -12.9 dB, -18.2 dB, -23.8 dB, -37.5 dB and -43.4 dB respectively.

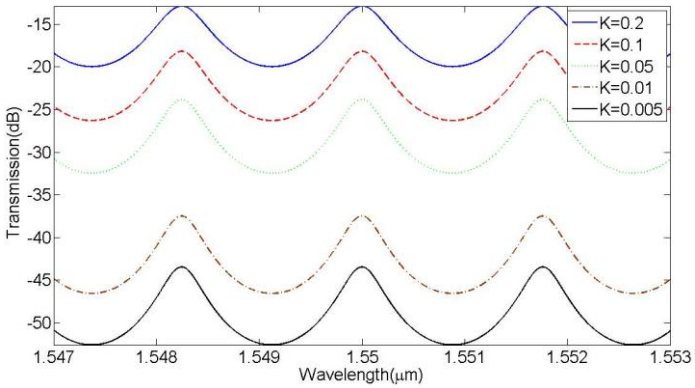

Fig. 4.11 transmission of the ring with radius of 50μm and loss of 100 dB/cm.

Fig. 4.12 shows the transmission of ring with a radius of 5 μm and a loss of 100 dB/cm. The intensity degradation for *K* value of 0.2, 0.1, 0.05, 0.01 and 0.005 is -2.46 dB, -4.55 dB, -7.65 dB, -18.3 dB and -23.8 dB respectively.

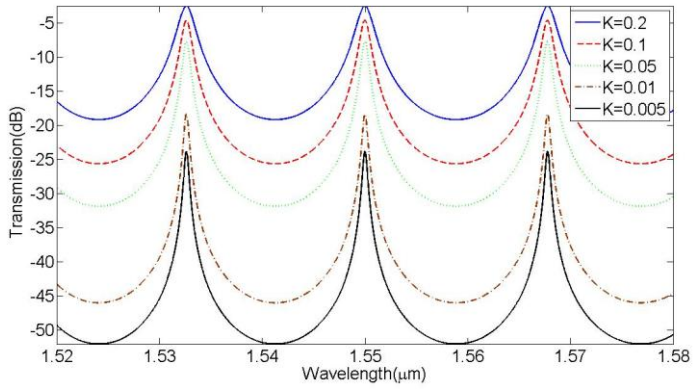

Fig. 4.12 transmission of the ring with radius of 5 μm and loss of 100 dB/cm.

Fig. 4.11 and Fig 4.12 show the influence of the size of the ring when the loss value is high. Apparently, the intensity is crucial for achieving a high sensitivity for sensors based on intensity interrogation. A small *K* value and a large ring provide a high Q value but the intensity degradation will limit the sensitivity. A large ring with high Q is therefore not useful in practical devices.

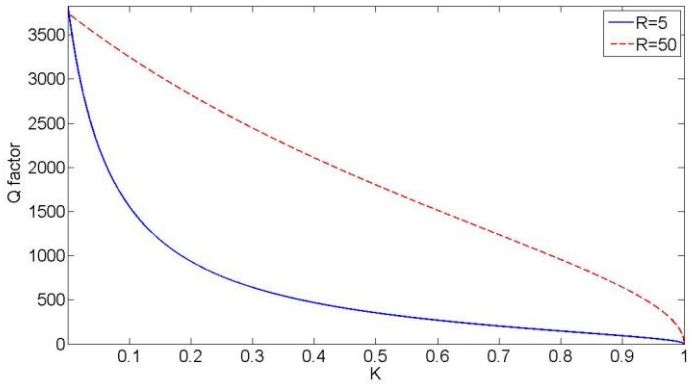

Fig. 4.13 Q factor versus K value with the radius as a parameter, the loss is set to be 100 dB/cm.

4.3.3 Analysis of the intensity of sensitivity

As shown in Fig. 4.12, *K*=0.1 allows for an intensity decay around 4.55 dB. In this situation, the Q factor is around 1556. For a 50 μm ring, the K value must reach 0.7 to achieve around 5 dB intensity decay. In this case, Q factor is around 1236. Because of the restriction of the intensity, a larger ring cannot provide a larger Q factor with the same intensity decay. From the graphs we can see the intensity difference (from peaks to valleys) of the small ring is much larger than that of the larger ring which means the average sensitivity of small ring is larger than that of the larger ring. Furthermore, larger *K* requires longer coupling region which is hard to realize.

For the reasons mentioned above, smaller ring is more promising at a larger loss value (e.g. in order of 100 dB/cm). We set the radius to be 5 μm, the loss is 100 dB/cm and *K* is 0.1 corresponding to intensity decay around 5 dB. The Q factor is 1556 in this case. The sensitivity reaches 725 dB/RIU and the detection limit of the sensing ring is 1.36×10^{-5} which is of an order of degradation compared with the 9.52×10^{-7} we have obtained on low loss (5 dB/cm) structure.

4.4 Conclusion

In conclusion, an optical sensor based on a FP laser and two rings has been theoretically investigated. By using a monitoring ring with the same waveguide structure, the wavelength instability of the laser and the ring can be monitored and controlled during the detection. Only three detectors are needed to apply the intensity interrogation method. No calibration is needed for the response of the detectors and no absolute wavelength or power control for the laser or rings is required. All we need is to control the relative wavelength from the relevant output power feedback from the three detectors.

A system detection limit of refractive index in the order of 10^{-6} can be achieved which corresponds to a wavelength shift of 0.06 pm. To achieve such a high sensitivity, the wavelength shift of the laser and the ring caused by environment must be less than 0.06 pm and the temperature change of the ring and FP laser would need to be controlled within 8.57×10^{-4} ℃ and 1.20×10^{-4} ℃, respectively, without the monitor ring.

There is no additional fabrication or interrogation complexity since the two rings contribute the same to the detection limit. The scheme is analyzed for SOI platform but it is not necessarily constrained on it. It is promising for realizing a high sensitivity, easy-to-fabricate and cost effective large array integrated sensor system.

By using small ring, the sensitivity of sensing ring decreases an order with a loss value increase from 5 dB/cm to 100dB/cm. The intensity degradation of the transmission of the two designs is maintained similarly (around -5dB). For the waveguides with high loss like 100 dB/cm, the detection limit reaches order of 10^{-5}.

Reference

[1] D.-X. Xu, M. Vachon, A. Densmore, R. Ma, A. Delage, S. Janz, J. Lapointe, Y. Li, G. Lopinski, D. Zhang, Q. Y. Liu, P. Cheben, and J. H. Schmid, "Label-free biosensor array based on silicon-on-insulator ring resonators addressed using a WDM approach," Opt. Lett., 35, 2771-2773, 2010.

[2] D.-X. Xu, M. Vachon, A. Densmore, R. Ma, S. Janz, A. Delage, J. Lapointe,P. Cheben, J. H. Schmid, E. Post, Sonia Messaoudene, and Jean-Marc Fedeli, "Real-time cancellation of temperature induced resonance shifts in SOI wire waveguide ring resonator label-free biosensor arrays," Opt. Express, 18, 22867-22879, 2010.

[3] Kristinn B. Gylfason, Carl Kristinn B. Gylfason, Carl F. Carlborg, Andrzej Kazmierczak, Fabian Dortu, Hans Sohlström, Laurent Vivien, Carlos A. Barrios, Wouter van der Wijngaart, and Göran Stemme, "On-chip temperature compensation in an integrated slot-waveguide ring resonator refractive index sensor array," Opt. Express, 18, 3226-3237, 2010.

[4] A. Densmore, D.-X. Xu, S. Janz, P. Waldron, T. Mischki, G. Lopinski, A. Delage, J. Lapointe, P. Cheben, B. Lamontagne, and J. H. Schmid, "Spiral-path high-sensitivity silicon photonic wire molecular sensor with temperature-independent response," Opt. Lett., 33, 596-598, 2008.

[5] Yurii. A. Vlasov and Sharee J. McNab, "Losses in single-mode silicon-on-insulator strip waveguides and bends," Opt. Express, 12, 1622-1631, 2004.

[6] D. B. Leviton and B. J. Frey, "Temperature-dependent absolute refractive index measurements of synthetic fused silica," Proc. SPIE 6273, 62732K, 2006.

[7] B. J. Frey, D. B. Leviton, and T. J. Madison, "Temperature-dependent refractive index of silicon and germanium," Proc. SPIE 6273, 62732J, 2006.

CHAPTER 5

Experimental investigation of the oxide/non-oxide interface after oxidation of AlGaAs

In previous chapters we experimentally demonstrated optical sensors for hybrid integration giving important proof-of-concept results. In this chapter we present the work on the GaAs/AlGaAs system explored for future monolithic integration. GaAs/AlGaAs material system is generally used in the manufacture of active devices such as light-emitting diodes (LED), laser diodes (LD), solar cells and integrated circuits. The GaAs/AlGaAs system is thus promising for the combination of passive sensing region and active source on a single chip.

To achieve monolithic passive-active integration, the first step is to develop high quality passive waveguide with high-sensitivity structure. For this purpose, the technology of wet oxidation of buried AlGaAs layer is used to obtain a high refractive index contrast structure which in turn is more sensitive to the ambient refractive index change.

We first show the principle and mechanism of the wet oxidation and the influence of different parameters to the oxidation process such as AlAs mole fraction, oxidation temperature, the flow rate of carrier gas, etc. We then present the unexpected vertical oxidation of GaAs and low-Al-content $Al_xGa_{1-x}As$ (x=0.34) layers induced by lateral wet oxidation of neighboring Al-rich $Al_xGa_{1-x}As$ (x>0.7) layer discovered during the waveguide fabrication. We designed a new structure to restrain the vertical oxidation and protect the waveguide core. The interface has been investigated by transmission electron microscopy (STEM) and *in situ* energy-dispersive X-ray spectroscopy (EDX). Experimental results show H_2 plasma treatment to a dry etched surface can activate the oxidation of GaAs demonstrating hydrogen residual plays a critical role in the oxidation process of the GaAs or AlGaAs.

The experiment and measurement works involved in this chapter were carried out in LPN.

5.1 Wet oxidation of AlGaAs

Wet oxidation is a technique to obtain buried oxide layer of AlGaAs or AlAs. The native oxide layer allows high refractive index contrast which is favorable for high sensitivity sensing waveguides. After oxidation, AlGaAs/Al_xO_y system has similar refractive index contrast as SOI.

Wet oxidation is an important technique in Ⅲ-Ⅴ semiconductor devices offering robust native oxide just as SiO_2 in silicon system. The formation of a robust and stable native oxide on silicon is the foundation of integrated circuit technology based on silicon. The merits of SiO_2 include high density, mechanical stability, low interface state density and insulating properties [1]. The native oxide of Ⅲ-Ⅴ semiconductors has been pursued for decades and these native oxides tend to be mechanically and chemically unstable [2, 3]. However the lateral oxidation of buried $Al_xGa_{1-x}As$ layer in a wet ambient discovered in 1990 allowed for a chemically and mechanically stable native oxide with reduced thickness [4]. The much higher oxidation rate of AlAs relative to GaAs has enabled the selective oxidation of buried $Al_xGa_{1-x}As$ (x>0.7) layers sandwiched between lower-Al-content $Al_xGa_{1-x}As$ or GaAs cladding layers.

In AlGaAs and several other Al-containing semiconductors (e.g., AlInGaP, AlInAs, and AlGaSb), these native oxides provide insulating material with low refractive index (n~1.6), which has been widely used for a variety of applications, such as current apertures [5, 6] and optical confinement [7] in vertical cavity surface emitting lasers, low-index material for ridge waveguides [8], higher refractive index contrast distributed Bragg reflectors (DBRs) [9], and nonlinear waveguide applications [10-12]. In parallel to the device development, important efforts have been carried out on oxidation process to improve the quality of resulting oxide, such as using small Ga mole fraction in the original layer composition to improve mechanical stability [13], post *in situ* annealing to remove the volatile products of the oxidation process and improve the thermal stability [14], enhanced kinetics of AlGaAs wet oxidation through the use of hydrogenation [15], the analysis of the role of hydrogen in wet oxidation reaction [16], the characterization of the influence of process parameters [17,18] and the chemical composition of the Al_xO_y material [19]. The oxidation of GaAs near the oxidized AlGaAs/GaAs interface was mentioned [20], but their experimental demonstration was ambiguous.

In this section, the mechanism of oxidation is introduced. Several parameters which affect the oxidation process are discussed including diffusion of oxidation species, thickness of layer, Al content, oxidation and bubble temperature and neighboring layers.

5.1.1 Basic principle

The wet thermal oxidation of $Al_xGa_{1-x}As$ layer (x> 0.7) is achieved by exposing the sample to a stream saturated with water in a chamber at a temperature around 400 ℃. Oxidation occurs when diffusion of oxidation species gets through the layer of AlGaAs and gives rise to aluminum oxide Al_xO_y or $Ga_{1-x}Al_xO_y$ amorphous structure. In the literature the equations that describe chemical reactions of wet oxidation process are listed as follows [16]:

$$2AlAs + 6H_2O_{(g)} \Leftrightarrow Al_2O_3 + As_2O_{3(l)} + 6H_2 \quad \Delta G^{698} = -473kJ/mol \qquad (5.1)$$

$$As_2O_{3(l)} + 3H_2 \Leftrightarrow 2As + 3H_2O_{(g)} \qquad \Delta G^{698} = -131kJ/mol \qquad (5.2)$$

$$As_2O_{3(l)} + 6H \Leftrightarrow 2As + 3H_2O_{(g)} \qquad \Delta G^{698} = -1226kJ/mol \qquad (5.3)$$

Unlike dry oxidation process in which oxide is achieved by the change from zero-valent oxygen O or O_2 to O^{-2}, during wet oxidation the oxygen is already in state of O^{-2} in water molecule. The agent element that enables the formation of oxide of aluminum in a thin film is H^+. The hydrogen produced by Eq. (5.1) reacts with intermediate As_2O_3 as shown in Eq. (5.2) and Eq. (5.3) obtaining production of As or AsH_3 which are highly volatile. The disposal of these products is essential for the oxidation propagation (up to several tens of microns) in a thin layer (down to a few tens of nm).

The mechanisms of diffusion takes place through the amorphous structure of already formed oxide to the interface with the semiconductor. In crystalline layers around the oxidized layer, this diffusion can be facilitated by the presence of defects. However, in the

temperature range where the oxidation occurs, the diffusion length of ions and molecules through the crystal lattice is very short. The propagation of oxide front is due to the transport of the oxidation species through the pores of the oxide [21].

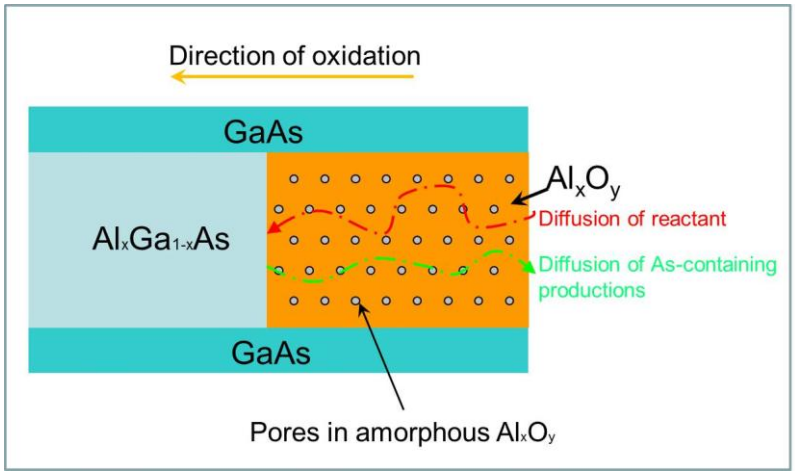

Fig. 5.1 Mechanism of diffusion during wet oxidation.

These pores would also allow the evacuation of volatile species resulting from the different chemical reactions involved.

Under the experimental conditions, the process reaches saturation with a limit of oxidation depth of an order of 50-100 µm. We found in the literature several attempts to explain this phenomenon, for example the closing of the pores of the oxide by oxygen [22] or induced by the accumulation of products of reaction at the interface of oxide/semiconductor [3].

5.1.2 Volume change after wet oxidation

When wet oxidation of AlAs was first reported in 1978 by Tsang [23], the native (Gibbsite phase) oxide was formed at the low temperature (100 ℃) with a greater thickness compared to the original AlAs layer. A decade later, it was discovered that wet oxidation of Al-containing compounds (AlGaAs, AlInAs, etc.) at a higher temperature (above 300 ℃) produces a chemically and mechanically stable oxide with a low refractive index and reduced thickness relative to the original layers [4, 24].

During the wet thermal oxidation process, the volume of the oxide layer reduces relative to the volume of AlAs layer which results in a reduction of thickness. This is partly due to tensile strain induced by the formation of oxide and the compression occurring at the oxidation front.

Theoretically this reduction in volume is estimated to have 20 % because in a molecule of AlAs the volume per aluminum atom is $(3.57Å)^3$ and it is only $(2.85Å)^3$ in the oxide γ-Al_2O_3 [25]. However, experimental studies by Takamori et al [26] show that AlAs layer gets a reduction in volume of 13 % during conversion to oxide. In Fig. 5.2, we can see during a transition length of 200 nm, the thickness reduces gradually through the interface

of AlAs/oxide. In the mean time, the thickness of the GaAs layer remains almost constant even if there is a slight change (about 2 %) in the area adjacent to the oxide which can be explained by a tensile strain induced by the decrease of the thickness of oxidized AlAs.

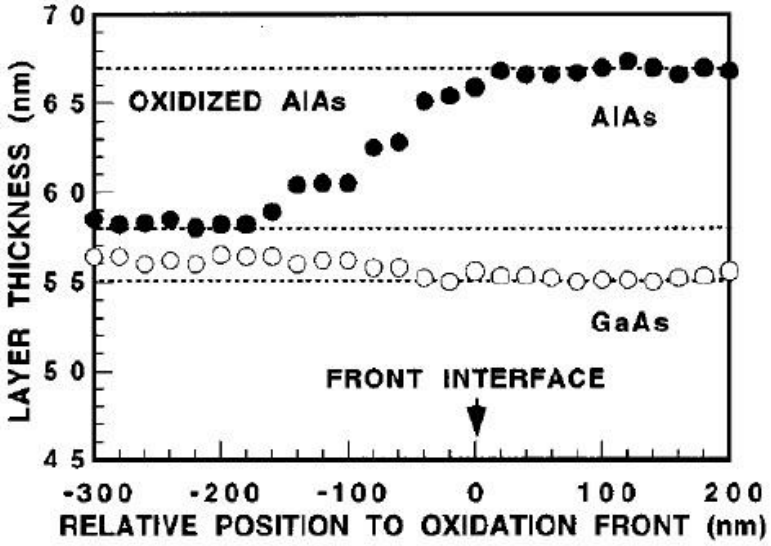

Fig. 5.2 Thickness measurements near the oxidation front, adapted with permission from [26]

This contraction can be significantly decreased by adding a small amount of gallium in the original layer. Indeed, Twesten et al showed that after wet thermal oxidation, the vertical contraction of a layer of $Al_xGa_{1-x}As$ (x=0.92 and 0.98) is only 6.7 % [27] which is consistent with the results of our works.

5.1.3 Presence of Ga fraction on isotropic and stable oxidation

For layers with high aluminum content (e.g. AlAs), the crystalline orientation also has an influence on the evolution of the oxidation front. Choquette et al observed that for an Al percentage greater than 94 %, oxidation was not progressing at the same oxidation rate in different crystalline planes [13]. It appears faster in the (100) planes than (110).

This phenomena can be explained by the low reactivity of the surface (110) planes as explained by Ranke et al in their studies on the adsorption of oxygen in a cylindrical GaAs crystal according to its crystal planes [28].

Consequently, this dependence leads to crystallographic anisotropy of oxidation. However, it is possible to improve this situation by adding a few gallium atoms. For a gallium proportion of more than 6 %, oxidation is uniform in all crystal planes and allows the production of an isotropic oxide.

Moreover, the mechanical stability of mesas which contain buried lateral oxide layers is also observed to depend on the original layer composition [13]. Fig. 5.3 shows a thermal mechanical stability comparison of mesas with or without small amount of gallium in

ready-to-oxidize layer. The mesas containing small amount of Ga in the oxide as shown in Fig. 5.3 (a) are unaffected by the annealing at 350 ℃ for 30 s, while the mesas shown in Fig. 5.3 (b) without Ga in the oxide apertures delaminate along the oxide/semiconductor interfaces. The susceptivity to thermal annealing is particularly hazardous during other post-oxidation fabrication processes which require high temperatures above 100 ℃ (e.g., photoresist baking).

The obvious change in mechanical stability is correlated with different strain levels observed by Choquette et al [29] for oxide apertures formed from AlGaAs and AlAs, respectively.

The addition of a small amount of Ga and the use of thin AlAs layers (e.g., 20 nm) is found to eliminate this mechanical instability.

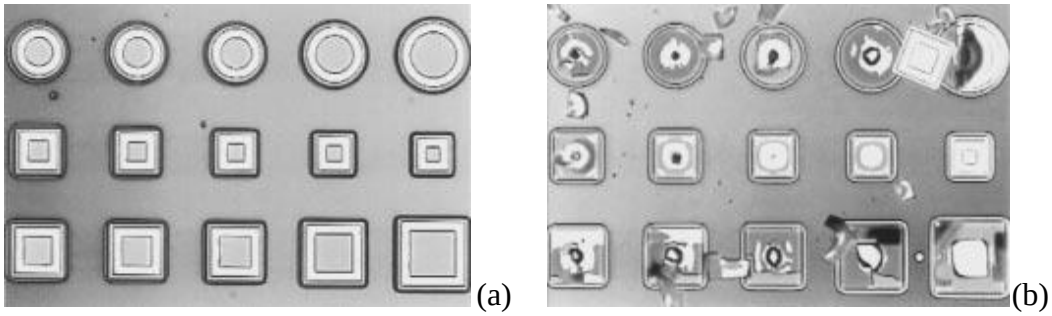

(a) (b)

Fig. 5.3. Top view of VCSEL mesas after wet oxidation and rapid thermal annealing at 350 ℃ for 30 s. The mesas contain $Al_xGa_{1-x}As$ oxide apertures with: (a) x=0.98, and (b) x=1.0. Adapted with permission from [13].

5.1.4 Influence of the aluminum content on oxidation rate

The oxidation rate of AlGaAs layer strongly depends on the proportion of aluminum because, considering the chemical reactions described above, the transformation of GaAs to oxide Ga_xO_y, is much harder than for AlAs.

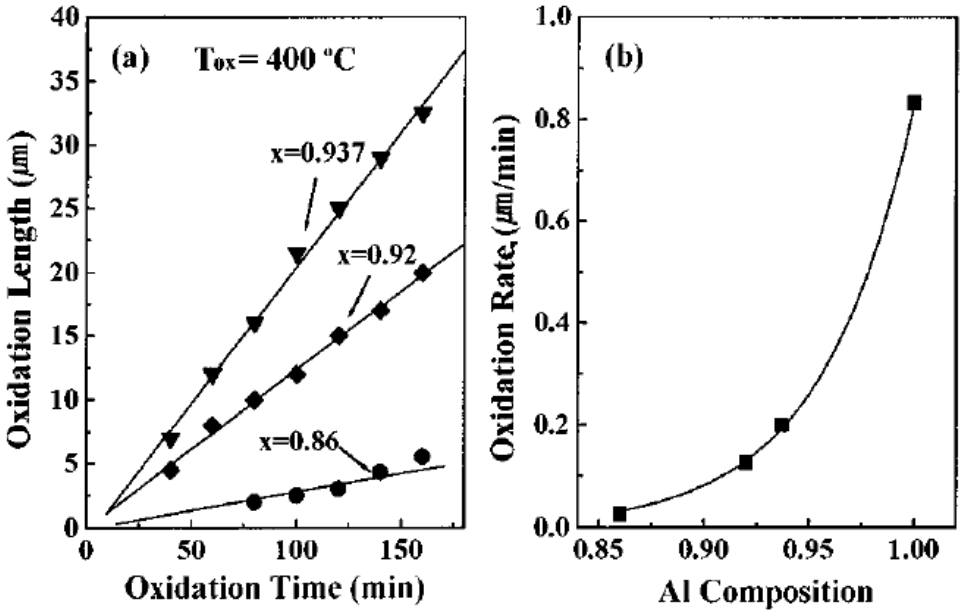

Fig. 5.4 Lateral wet oxidation of n-type 1-μm-thick AlxGa1-xAs layers; (a) oxidation length vs oxidation time indicating the linear growth rate law and (b) oxidation rate vs Al composition showing a high degree of oxidation selectivity. Adapted with permission from [30]

The oxidation rate dependence on Al percentage is illustrated in Fig. 5.4 [30]. We notice that for a change of Al proportion from 100 % to 84 % the oxidation rate falls two orders of magnitude. This selectivity permits various applications, for example for the production of single oxide aperture of a VCSEL. In this case, the high selectivity with respect to the Al content, allows using high concentrations of Al (~ 90 %) in Bragg mirrors and obtaining a large index contrast.

From realistic fabrication point of view, the high selectivity is however a drawback for precise control of the oxidation rate of the layer, since the processes of conventional epitaxy (MBE or MOVPE) do not allow control of the composition of alloys less than 1 % which is necessary for the stabilization of the oxidation rate.

5.1.5 Effect of the thickness of the layer to be oxidiwed

The thickness of the layer which is to be oxidized is an intrinsic parameter which affect considerably the kinetics of the oxidation [30, 31]. This influence is dominant for thicknesses less than 75 nm. Below this value there comes a saturation of the oxidation rate. The most likely explanation for this phenomenon is that the diffusion process of species for oxidation and the evacuation of volatile products of reactions are disrupted in the thin layers.

According to a publication by Kim et al [30], there is a minimum thickness of 11 nm for the lateral wet oxidation, below which no oxidation can occur. In a layer with a thickness of less than this value the progress of the oxidation front is blocked by the size of the grain

structure of the oxide Al_2O_3 of about 8 nm [19]. However the use of a thin layer can limit the strain generated by the phenomenon of volume shrinkage and help to reduce optical losses.

5.1.6 Influence of doping

The dependence of wet thermal oxidation on doping type has been observed so that whatever the temperature is, the oxidation rate of a P doped layer is higher than that of an N doped layer [32]. The difference of oxidation rate is not from the intrinsic properties of doping but the position of the Fermi level in the oxide relative to the semiconductor creating a potential barrier for oxidation species.

As explained above the oxidation process is affected by the diffusion of ions through the oxide enhanced by the crystal defects. So the oxidation rate depends on the concentration of defects which is linked to the Fermi level in the crystal [33]. So any change of doping causes a variation of the Fermi level and the concentration of charged defects. Finally the factor of oxidation rate is changed.

5.1.7 Effect of oxidation duration and temperature

To describe the development of wet thermal oxidation process in time, we can use the model of Deal-Grove [34] which is used for the kinetics of the oxidation of silicon. This model takes into account two processes of the oxidation ----species diffusion and reaction at the oxidation front. The oxidation depth as function of time t is expressed by the following relationship [35]:

$$X_{ox} = \frac{A}{2}\left(\sqrt{1+\frac{t}{A^2/4B}}-1\right) \tag{5.4}$$

Or more simply:

$$X_{ox}^2 + AX_{ox} = Bt \tag{5.5}$$

Where B is proportional to the diffusion constant of the oxidizing species and B/A is a function of the reaction rate constant for oxidation at the oxide/AlAs interface. For short oxidation time and thin oxide thicknesses Eq. (5.5) becomes a linear form $X_{ox} = [B/A]t$. While in the case of long duration oxidation with thicker oxide layers, there is a parabolic behavior such that: $X_{ox} = [Bt]^{1/2}$

The parameters A and B are functions of Arrhenius type and are expressed in literature by the following equations

$$A = A_0 \exp\left(-\frac{E_a^A}{kT}\right) \tag{5.6}$$

$$\frac{B}{A} = (\frac{B}{A})_0 \exp(-\frac{E_a^{B/A}}{kT}) \tag{5.7}$$

Where E_a^A and $E_a^{B/A}$ are the activation energies of corresponding reactions. The temperature of oxidation is T and k is the Boltzmann constant. Fig. 5.5 (a) shows the different evolutions of the oxidation depth of AlAs layer at temperatures of 440 ℃ and 518 ℃. We can see that at 440 ℃ oxidation scales linearly indicating that it is limited by the rate of reaction rather than oxidation species diffusion through oxide layer to the oxidation front. At 518 ℃ we find that beyond a depth of 40 μm oxidation regime changes and oxidation depth follows a parabolic law. There is a beginning of saturation that results in the slower oxidation limited by the rate of diffusion as confirmed by the nonlinear temporal growth profile at high temperature range of Fig. 5.5 (b).

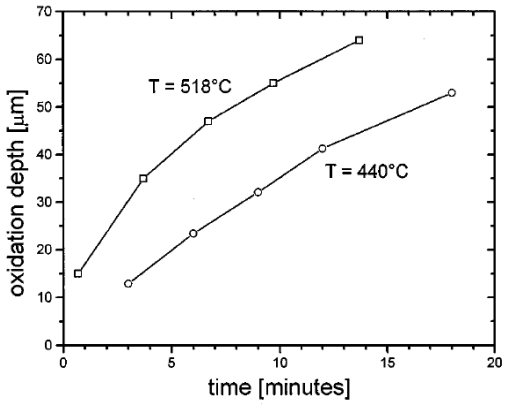

(a)

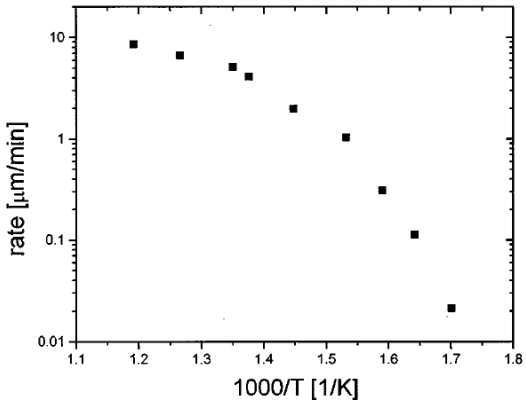

(b)

Fig. 5.5 (a) Evolution of the oxidation depth of AlAs layer at temperatures of 440 ℃ and 518 ℃. (b) Measured growth rate as a function of inverse temperature assuming a linear growth rate. Adapted with permission from [35].

Moreover, for each temperature it is possible to access the parameters A and B by making a fitting between the measured values of oxidation depths and Eq. (5.5). The values of B and B/A are plotted using an Arrhenius law for determining activation energies of the two corresponding processes as shown in Fig. 5.6. The diffusive and reactive activation energy values were found to be 0.8 eV and 1.6 eV, respectively for kinetics of the wet thermal oxidation of AlAs.

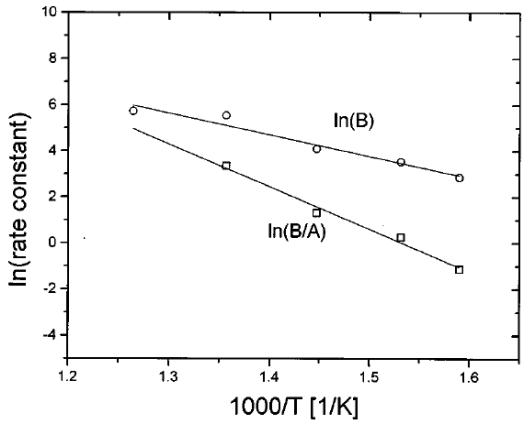

Fig. 5.6 Arrhenius plot of the diffusion and reaction constants. Adapted with permission from [35]

Other studies have also assessed the activation energy of reaction of the AlAs around 1.3eV [25]. These values compared with those reported in the literature for the oxidation of silicon (0.7 eV for the diffusion and 1.9 eV for the reaction) [35] show that the compounds based on aluminum oxidize faster than the silicon since the reaction mechanism requires less energy.

It should be noted that in low temperature range and for short oxidation depth the oxidation rate in AlAs is dominated by reaction rate rather than diffusion. When the temperature increases the reaction rate increases faster than diffusion making the diffusion process non-negligible.

5.1.8 Influence of layer structures

In addition to its thickness, the layer structure and the immediate vicinity of specific layers may affect the oxidation process. According to their composition, neighboring layers may accelerate or slow down the oxidation process of a given layer. For example, Fig. 5.7 taken from the work of Kim et al [30] shows two oxidation process of a layer of 60 nm AlAs in two different configurations. In the first case, the AlAs is sandwiched between two layers of GaAs (line (a)) while in the second configuration AlAs has been inserted between two layers of 10 nm $Al_{0.72}Ga_{0.28}As$ (line (b)). It is clear that the oxidation rate is higher in the former case than in the second. That is to say that the use of $Al_{0.72}Ga_{0.28}As$ as neighboring layers of AlAs resulted in a reduction of the oxidation rate. Note that in both cases, neighboring layers are not oxidized. The nature of the adjacent layers must be taken into account for better understanding the process of wet thermal oxidation.

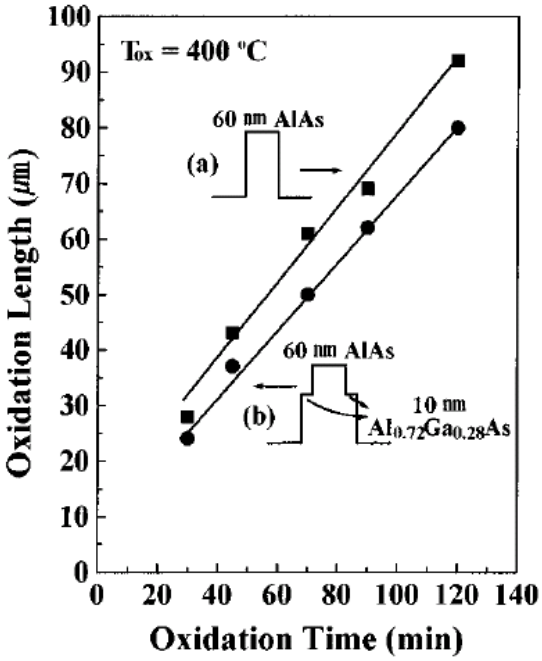

Fig. 5.7 Length of oxidation of AlAs as a function of time surrounded by (a) 60 nm of GaAs and (b) 10 nm of $Al_{0.72}Ga_{0.28}As$ on each side. Adapted with permission from [30].

In the literature there are several other studies of the dependence of oxidation rate of a layer relative to its structure. One of these examples is that of superlattices. Studies have shown that the behavior is equivalent to those of homogeneous alloys [36].

5.1.9 Influence of the gas flow

The oxidation rates of 84-nm-thick $Al_{0.98}Ga_{0.02}As$ layers as a function of N_2 gas flow through deionized water at different temperatures are studied [37]. Sufficient gas flow makes the system work in a water vapor saturated environment where the oxidation is not reactant-limited. It should be noted in their study the results are based on a 4-inch-diameter furnace where 3 L/min of N_2 is sufficient to maintain a constant oxidation rate. Moreover, the oxidation rate increases with an increasing bath temperature. Note that the water temperature in the bubbler (at constant bath temperature) is found to vary with changing gas flow, reinforcing the importance of maintaining a constant gas flow.

The wet oxidation is also studied by using various carrier gases through water. The oxidation rates vary only slightly with N_2, Ar, or forming gas (3 % H_2/N_2) as the carrier gas. In contrast, O_2 bubbled through water completely suppresses the AlGaAs oxidation process which is consistent with the wet oxidation principal mentioned above.

5.2 Characterization of the interfaces of oxidized samples

In this part, after a brief introduction of wet oxidation caractarisation setup the interfaces of the oxidized buried layer of Al rich AlGaAs and adjacent GaAs or AlGaAs layers have been studied by scanning transmission electron microscopy (STEM) and in situ energy-dispersive X-ray spectrometer (EDX). A vertical oxidation crossing the interface of Al_xO_y/AlGaAs or Al_xO_y/GaAs is observed which results in additional roughness along the interface. By using GaAs/AlAs superlattice layers instead of bulk GaAs or AlGaAs, the vertical oxidation rate is dramatically reduced compared with that of AlGaAs or GaAs bulk layer. Furthermore, the interface of the oxide and the superlattice layers is also improved according to the STEM observation and analysis.

5.2.1 Wet oxidation setup

As mentioned above, the wet oxidation is achieved in a wet atmosphere saturated with water vapor at a temperature around 400 ℃. In our work, the sample is placed on a cylindrical oven of quartz with heating plate inside. The temperature is regulated by a thermal controller from EUROTHERM. The carrier gas N_2 goes through deionized water in a bath heated flask and carries water vapor for the reaction. The flask has three orifices, one for the carrier gas, the second for the temperature controlling of the bath and the third for water supply.

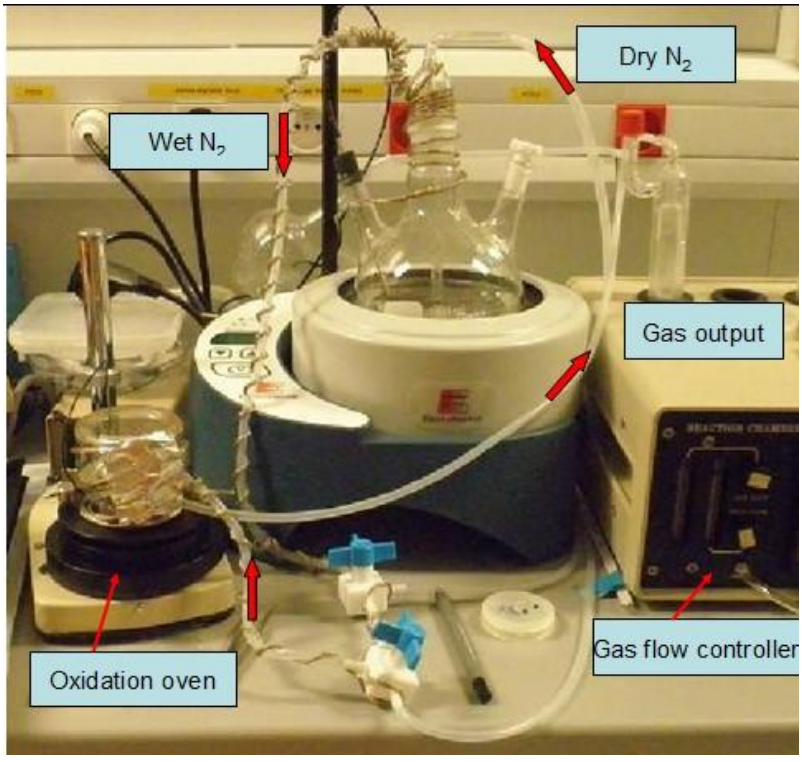

Fig. 5.8. The setup at LPN for wet oxidation.

The gas lines are heated during the oxidation process to avoid the condensation of the water vapor in the low temperature environment. Fig. 5.8 is a photo of the set-up at LPN to show all the elements of the wet oxidation system we used in this work.

It should be noted that the setup we used is a small cylindrical oven with gas input and output by the side. So the gas flow in the chamber is not very homogeneous. Furthermore, there is a gap between the heating plate and the quartz where we put the samples. The thermal sensor is set to connect with the heating plate. Because the gap is not uniform around the quartz cylinder, the temperature shifts from one spot to another. To avoid the influence of the gas flow and the temperature inhomogeneous, we put the sample at the same spot every time.

In this work, 1 μm $Al_{0.92}Ga_{0.08}As$ layer is sandwiched by $Al_{0.34}Ga_{0.66}As$ and GaAs. 8 % Ga in the AlGaAs can offer isotropic oxidization and thermal stability as discussed in previous part. The parameters we used are shown as follows.

Parameters of oxidation	Values found in literatures	Values used in this work
Temperature of bath(℃)	80-95	95
Temperature of oven(℃)	400-450	400-470
Carrier gas type	N2, N2+H2	N2
Carrier gas flow(L/min)	1-3	2
Pre-oxidation etching	RIE, H2SO4 H2O2	RIE,ICP

Table 5.1 Parameters of wet oxidation.

5.2.2 Characterization by ellipsometry

Ellipsometry uses polarized light to characterize thin film and bulk materials. A change in polarization is measured after reflecting light from the surface. Thin film thickness and optical constants are derived from the measurement.

Information is obtained from each layer interacting with the measurement. Light returning from the film-substrate interface interferes with the surface reflection to provide layer information (Fig. 5.9).

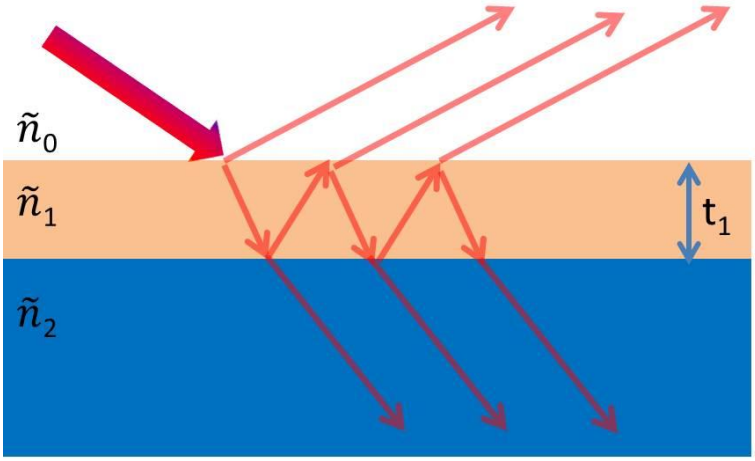

Fig. 5.9 Schematic of the measurement of reflection.

An ellipsometry measurement is a description of the change in polarization (Fig. 5.10) as polarized light is reflected from a sample surface. It is expressed as two parameters for each wavelength-angle combination: Psi (ψ) and Delta (Δ). These values can be related to the ratio of complex Fresnel reflection coefficients, r_p and r_s, for p and s polarized light, respectively.

$$\rho = \frac{r_P}{r_S} = \tan(\psi)e^{i\Delta} \tag{5.8}$$

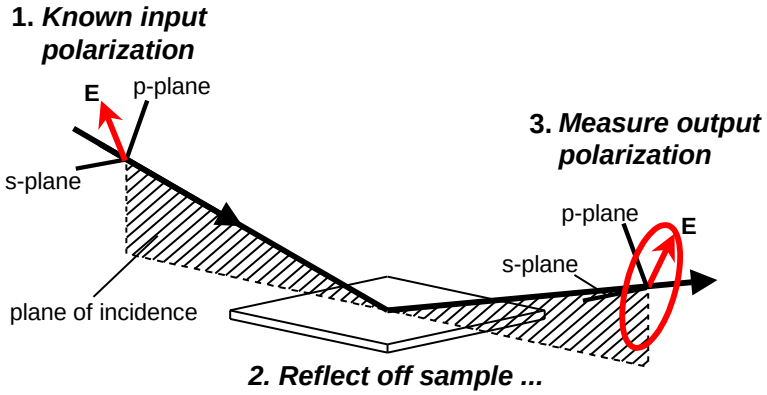

Fig. 5.10 Schematic of the measurement of polarization.

Optical constants of isotropic materials can be described using two parameters. These values decide how a material responds to excitation by light of a given wavelength. One representation is the complex refraction index, $\tilde{n}$ where the real part n is the index and the imaginary part, k, is the extinction coefficient as $\tilde{n} = \mathrm{n} + i\mathrm{k}$. By the measurement and data analysis, we obtained the complex refraction index of the oxide of $Al_{0.92}Ga_{0.08}As$ as shown in Fig. 5.11. The sample with 1 µm $Al_{0.92}Ga_{0.08}As$ on the top was directly and fully

oxidized from the surface providing Al_xO_y layer for the measurement. The epitaxy of the sample was performed at LPN by group ELPHYSE.

Both V-VASE and M-2000 spectroscopic ellipsometers were used to measure the samples. Al_xO_y appears to absorb in the deep ultraviolet (above 5.5 eV). Thus, it is modeled using Tauc-Lorentz oscillator.

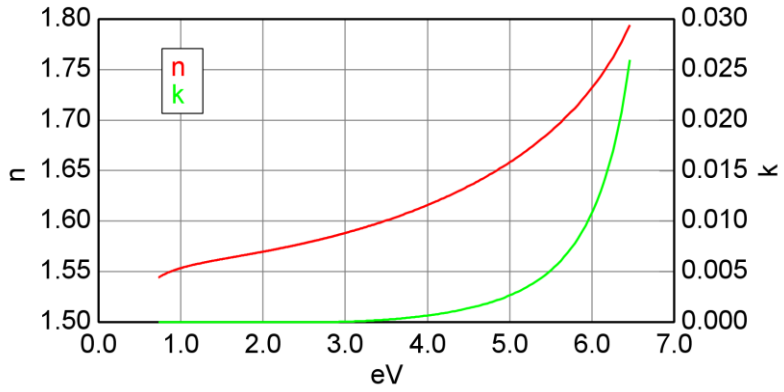

(a)

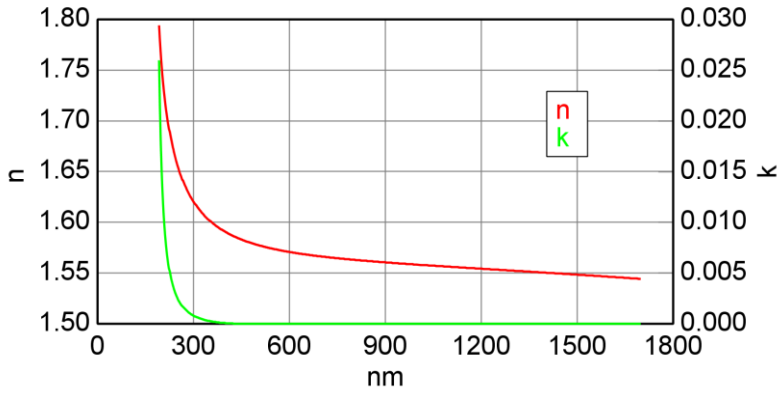

(b)

Fig. 5.11 (a) Optical Constants (versus energy in eV) of Al_xO_y of $Al_{0.92}Ga_{0.08}As$ (b)Optical Constants (versus wavelength in nm) of Al_xO_y of $Al_{0.92}Ga_{0.08}As$

The loss value is obtainedfrom the imaginary part of the complex index. The k value is 2.3 $\times 10^{-5}$ at 800 nm corresponding to a loss value of 15 dB/cm. At 1550 nm, the loss value is 0.

5.2.3 Fabrication of mesas and observation by STEM and EDX

In this part, we show the experimental observation of vertical oxidation of GaAs or low-Al-content AlGaAs layer in the vicinity of oxidized high-Al-content layer. This effect results in additional roughness along the oxide/semiconductor interface and a reduction of

the thickness of adjacent AlGaAs layer. To curb the vertical oxidation rate and obtain smoother interfaces, a novel superlattice structure is designed, fabricated and analyzed by STEM and *in situ* EDX. This structure can effectively restrain the vertical oxidation and provide a smoother interface.

5.2.3.1 Fabrication of the mesa

The samples used in this work were grown on n-doped (100) GaAs substrates by molecular beam epitaxy (MBE). Two similar structures with bulk $Al_{0.34}Ga_{0.66}As$ or GaAs/AlAs SL layers on top of the Al-rich layer have been grown. First a 100-nm thick GaAs buffer layer was grown. Then a 1-μm thick $Al_{0.92}Ga_{0.08}As$ layer was grown as the initial material to be oxidized. On top of the Al-rich layer, a 200-nm thick $Al_{0.34}Ga_{0.66}As$ layer and a 100-nm thick capping GaAs layer were grown for the standard structure (see Fig. 5.12 (a)). In the SL structure, the $Al_{0.34}Ga_{0.66}As$ layer was replaced by a 50-period SL layer (see Fig. 5.12 (b)). Each period consists of a 2.1 nm GaAs layer and a 1.9 nm AlAs layer giving an overall Al composition of 47.5 %. The bandgap energy of the SL structure is equivalent to that of bulk $Al_{0.34}Ga_{0.66}As$ alloy. All the epitaxial layers were undoped.

Both the standard and the SL structures were processed simultaneously. First, a 400-nm thick SiO_2 layer was deposited by plasma-enhanced chemical vapor deposition (PECVD). After photolithography and reactive ion etching (RIE) with SF_6, the pattern was transferred from photoresist to SiO_2. With a second RIE etching using $SiCl_4$, 10-μm wide, 1.5-μm deep mesas were formed on the AlGaAs/GaAs wafer as shown in Fig. 5.12 (c). Larger, 50-μm wide patterns were also defined in order to probe the oxidation kinetics for oxidized length larger than 10 μm.

Then the samples were oxidized in a quartz furnace at 420 ℃ while supplying water steam through a flow-controlled N_2 carrier gas from a water bubbler connected to the furnace and heated at 90 ℃. Samples were then prepared by focused ion beam (FIB) etching, defining ~150-nm thick, ~7-μm long, and ~5-μm high trenches for STEM observation. The STEM cross-sectional images in bright field (BF) or high-angle annular dark field (HAADF) mode were obtained with a transmission electron microscope Jeol 2200FS (200 kV field emission STEM/TEM with a CEOS GmbH hexapole Cs-corrector for the probe-forming lens). The composition in atomic percentage of each layer could be estimated using the EDX spectroscopy system installed in the microscope with the transmitted electron beam as the excitation source. The spatial resolution of the EDX analysis was estimated to be of ~ 3 nm.

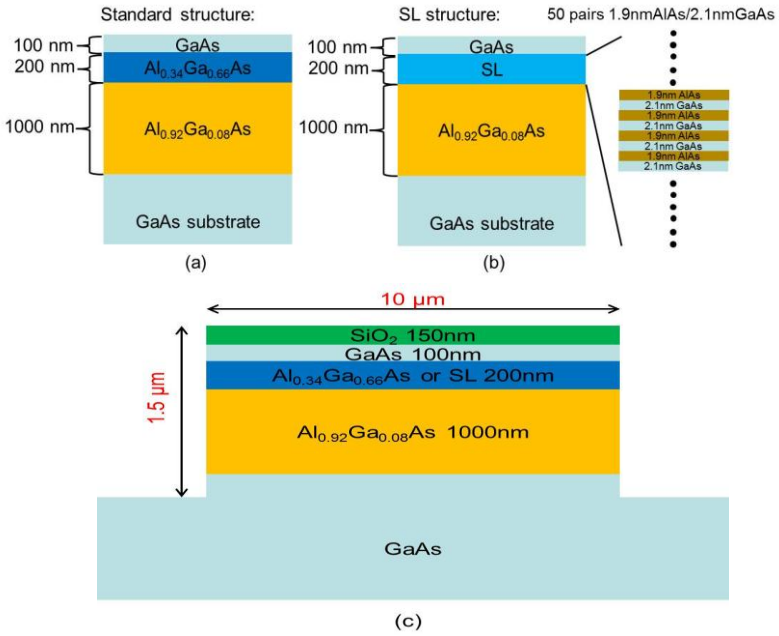

Fig. 5.12 Schematic of the standard (a) and SL (b) wafer structures and the cross-sectional view of the mesa (c). The remaining thickness of the SiO_2 mask is of ~150 nm after the etching step.

A cross-sectional view of the mesa is schematically depicted in Fig. 5.13. We chose position A and B at the mesa edge to illustrate the vertical oxidation process through the interface. Position C and D were used to observe the interfaces near the mesa center which is of importance for the processing of waveguides. The vertical oxidation of bulk material and SL has been compared at the same lateral position (positions A/B at the mesa edge, or positions C/D at the mesa center).

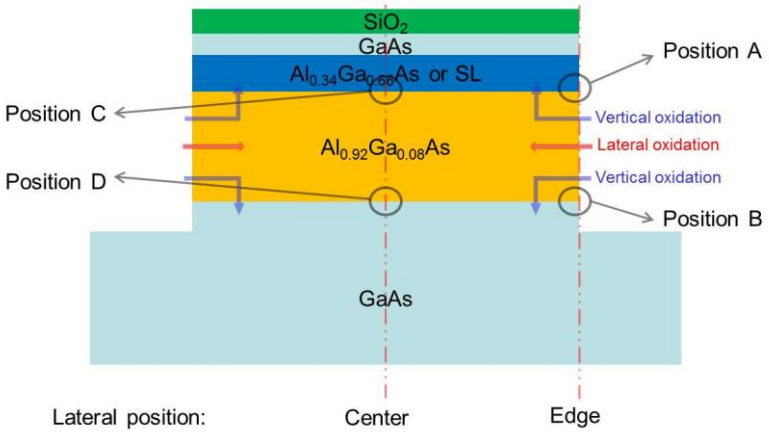

Fig. 5.13 Illustration of the cross section of the mesa. After wet oxidation, $Al_{0.92}Ga_{0.08}As$ layer will be oxidized laterally. Position A and B are used to observe the oxidation through the interfaces near the side of the mesa. Position C and D are used to observe and compare the interfaces near the center.

5.2.3.2 STEM observation and discussion

It was observed from the cross-section of a standard sample with 30 min oxidation that the $Al_{0.92}Ga_{0.08}As$ layer in the 10-μm wide mesas has been fully oxidized (the oxidation length was of ~ 6 μm from each side). The volume shrinkage of $Al_{0.92}Ga_{0.08}As$ layer after oxidation left the cracks at the oxide/non-oxide interfaces near the mesa edge as can be seen in Fig. 5.14. The upper bulk $Al_{0.34}Ga_{0.66}As$ layer was partially oxidized through the interface with the oxide of Al-rich layer as shown in Fig. 5.14. The atomic percentage of remaining As in the oxidized $Al_{0.34}Ga_{0.66}As$ was estimated by EDX and was found to be less than 3 %, indicating a complete oxidation of this layer. The oxidation depth in the $Al_{0.34}Ga_{0.66}As$ layer decreased with the increasing distance from the mesa edge which indicates that the vertical oxidation of the layer with low Al content started from the edge of the mesa, along with the lateral oxidation of the Al-rich layer. The oxidation depth in $Al_{0.34}Ga_{0.66}As$ was up to 65 nm at position A. Meanwhile, at the same position the sidewall of the $Al_{0.34}Ga_{0.66}As$ layer exposed to the ambience during the oxidation process was not oxidized. This result clearly shows that the oxidation of layer activated the vertical oxidation of the neighboring layer with low Al content which was not supposed to be oxidized under the same conditions otherwise.

The bottom interface between GaAs and the oxidized $Al_{0.92}Ga_{0.08}As$ layer was shown in Fig. 5.15. The GaAs underlayer was also oxidized with a lower oxidation rate than that of the $Al_{0.34}Ga_{0.66}As$ layer. The oxidation depth in GaAs peaked at 40 nm near the mesa edge (position B). The atom percentage of remaining As in the oxidized GaAs is found to be around 3 % from EDX analysis, indicating that GaAs oxidation into Ga-oxide was almost complete. On the other hand, the GaAs surface directly exposed to the ambience was not oxidized, similar to the case of $Al_{0.34}Ga_{0.66}As$. From Fig. 5.14 and Fig. 5.15, the vertical oxidation does not happen from the sidewall: the cracks or interface delamination caused by oxidation-induced volume shrinkage actually prevent the oxidation of the GaAs or $Al_{0.34}Ga_{0.66}As$ layer to be activated. In contrast, the direct contact to the oxidized Al-rich layer through the epitaxial interface allows for the activation of the oxidation of GaAs and $Al_{0.34}Ga_{0.66}As$. At the mesa center, the thickness of oxidized $Al_{0.34}Ga_{0.66}As$ and GaAs layers were reduced to 14 nm and 8 nm, respectively. At the same lateral position, the thickness of the oxide of $Al_{0.34}Ga_{0.66}As$ was always larger than that of the oxide of GaAs, which is consistent with the fact that the AlGaAs is easier to oxidize.

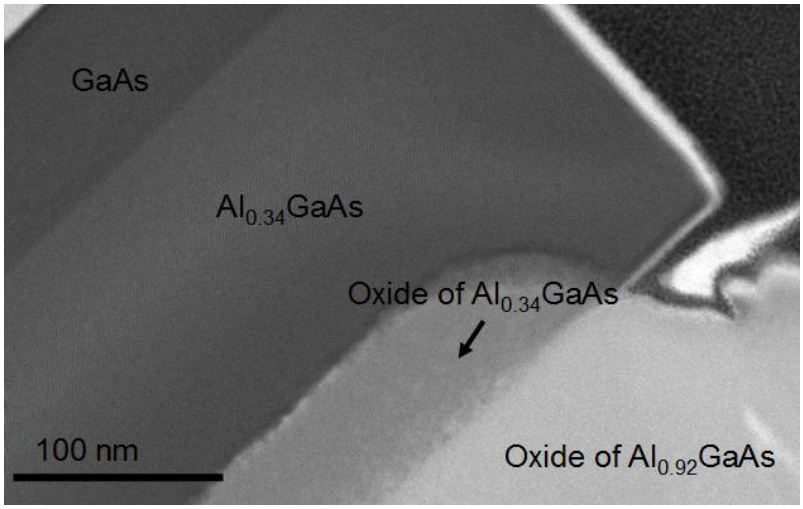

Fig. 5.14 BF-STEM cross-sectional image of wet oxidized $Al_{0.34}Ga_{0.66}As/Al_{0.92}Ga_{0.08}As$ interface near the sidewall of the mesa (position A in Fig. 5.13) oxidized for 30 min at 420 ℃.

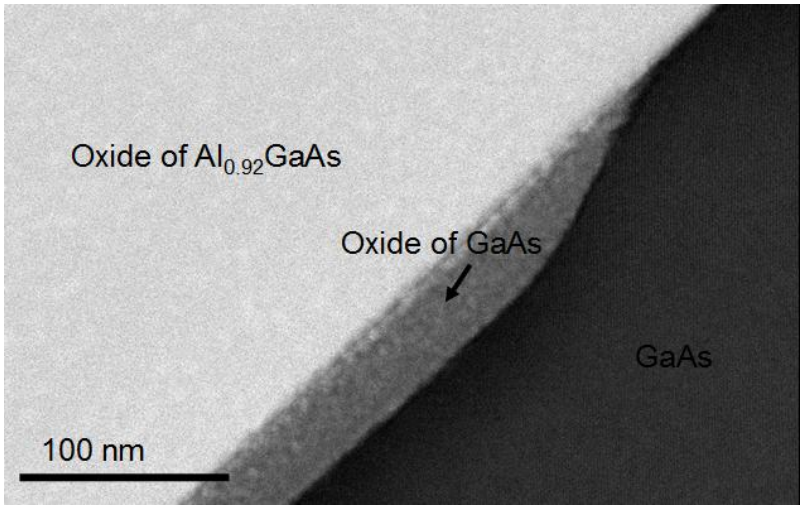

Fig. 5.15 BF-STEM cross-sectional image of wet oxidized $Al_{0.92}Ga_{0.08}As/GaAs$ interface near the sidewall of the mesa (position B in Fig. 5.13) oxidized for 30 min at 420 ℃.

As for the SL sample with 30 min oxidation, the oxidation rate of $Al_{0.92}Ga_{0.08}As$ was the same as with the standard structure. The SL layers were also oxidized from the mesa sidewall with an oxidation length of 230 nm as shown in Fig. 5.16. From EDX analysis, the SL layers were fully oxidized with 1.5 % As left (average value). The lateral oxidation rate of the SL was much lower than that of the $Al_{0.92}Ga_{0.08}As$ layer because the tiny thickness of the AlAs layers limited the oxidation process [31, 32]. The lateral oxidation rate of SL is indeed significantly suppressed when the thickness of AlAs layer is decreased [38]. It is clear from the STEM image in Fig. 5.16 that the oxidized SL layers still presented different contrasts corresponding to Ga-oxide and Al-oxide.

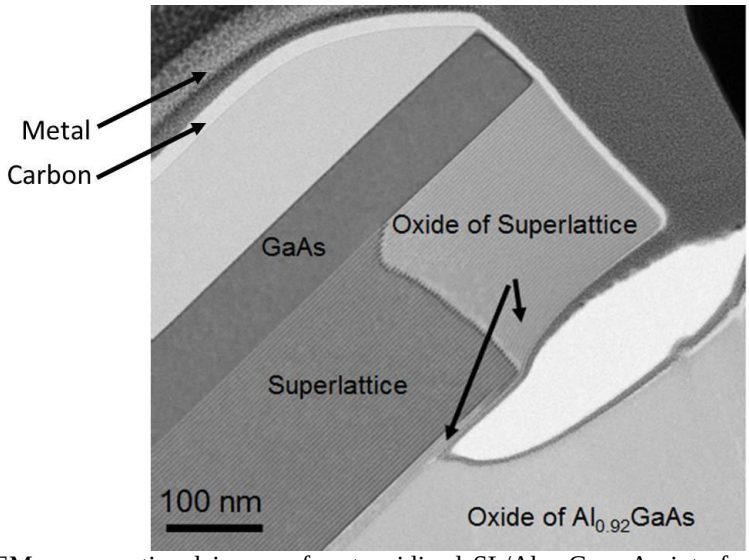

Fig.5.16 BF-STEM cross-sectional image of wet oxidized SL/$Al_{0.92}Ga_{0.08}As$ interface near the sidewall of the mesa (position A in Fig. 5.13) oxidized for 30 min at 420 ℃. Carbon and metal encapsulation is due to FIB preparation.

When looking at the interface between the SL and the oxidized Al-rich layer, it was found that only three SL periods (~12 nm) were oxidized from the interface close to the mesa edge (position A), which is much less than the oxidation depth in the bulk $Al_{0.34}Ga_{0.66}As$ (~65 nm), and more surprisingly less than the oxidation depth in bulk GaAs (~40 nm, position B). At the mesa center (position C) the vertical oxidation in the SL layer was limited to 1 period (4 nm). At the same lateral position, the thickness of the SL oxide was smaller than that of the $Al_{0.34}Ga_{0.66}As$ oxide, and even than that of the GaAs-oxide which cannot be simply explained by the Al composition of the material.

When the oxidation time reached 50 minutes, the lateral oxidation of the SL was around 400 nm. The vertical oxidation close to the mesa edge was 3 periods. In the central area, the vertical oxidation was 2 periods (~8 nm), while the oxidation of GaAs at the same position was 50 nm. This showed the high resistance of the SL structure against vertical oxidation from the interface with the oxide.

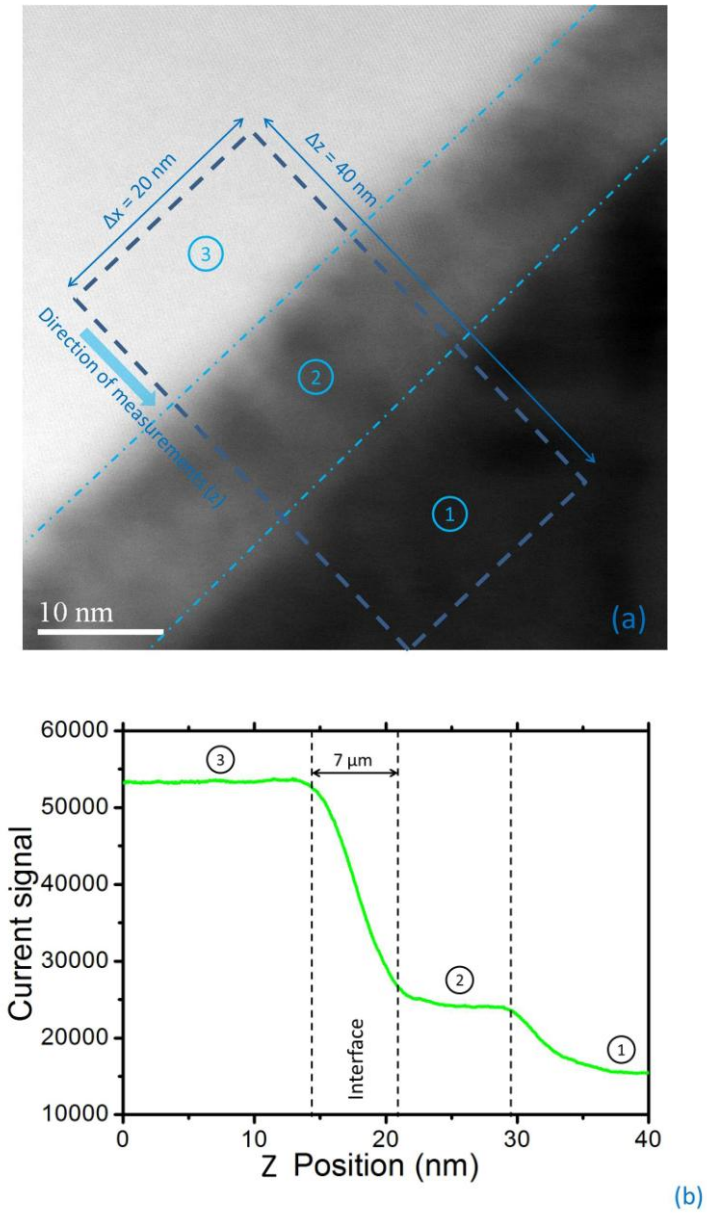

Figure 5.17 : (a)- HAADF STEM image of the oxide/non-oxide interface for the bulk $Al_{0.34}GaAs$ layer at lateral position C. The $Al_{0.92}GaAs$-oxide, $Al_{0.34}GaAs$-oxide, and non-oxidized $Al_{0.34}GaAs$ are labelled as 1, 2, 3 in the image. (b)- average density profile along the line Δz (b). For each position z the detector current is average over the width Δx.

A HAADF STEM image of the oxidized $Al_{0.34}Ga_{0.66}As/Al_{0.92}Ga_{0.08}As$ interface is shown in Fig. 5.17 (a). The oxidized $Al_{0.92}Ga_{0.08}As$ material of lowest density appears in dark, while the non-oxidized $Al_{0.34}Ga_{0.66}As$ of highest density appears in bright in this Z-contrast imaging mode. The intermediate layer corresponds to the vertically-oxidized $Al_{0.34}Ga_{0.66}As$ layer. It can be observed that the interface between the non-oxidized and oxidized materials is quite rough, which may increase the scattering loss in an optical waveguide. A quantitative estimation of the interface roughness can be derived from the average density profile extracted from the STEM image, reported in Fig. 5.17 (b). In this figure, the detector current is plotted as a function of position z along a line Δz perpendicular to the

interface. For each position z, the detector current is actually averaged over a width Δx. It was observed that the resulting curve did not very significantly for Δx > 15 nm, so that Δx was fixed to 20 nm to extract the density profile. It can be deduced from Fig. 5.17 (b) that the oxidized / non-oxidized interface extend over a width of around 7 nm.

The HAADF STEM image of the $Al_{0.92}Ga_{0.08}As$/GaAs interface, and the corresponding average density profile are shown in Fig. 5.18 (a) and (b). The vertically-oxidized GaAs corresponds to the intermediate layer in Fig. 5.18 (a). The crystalline structure of non-oxidized GaAs is apparent in the STEM image. It can be observed that the interface between the oxidized /unoxidized GaAs materials interface is also quite rough. The average density profile of Fig. 5.18 (b) shows that it extends over a width of around 6 nm.

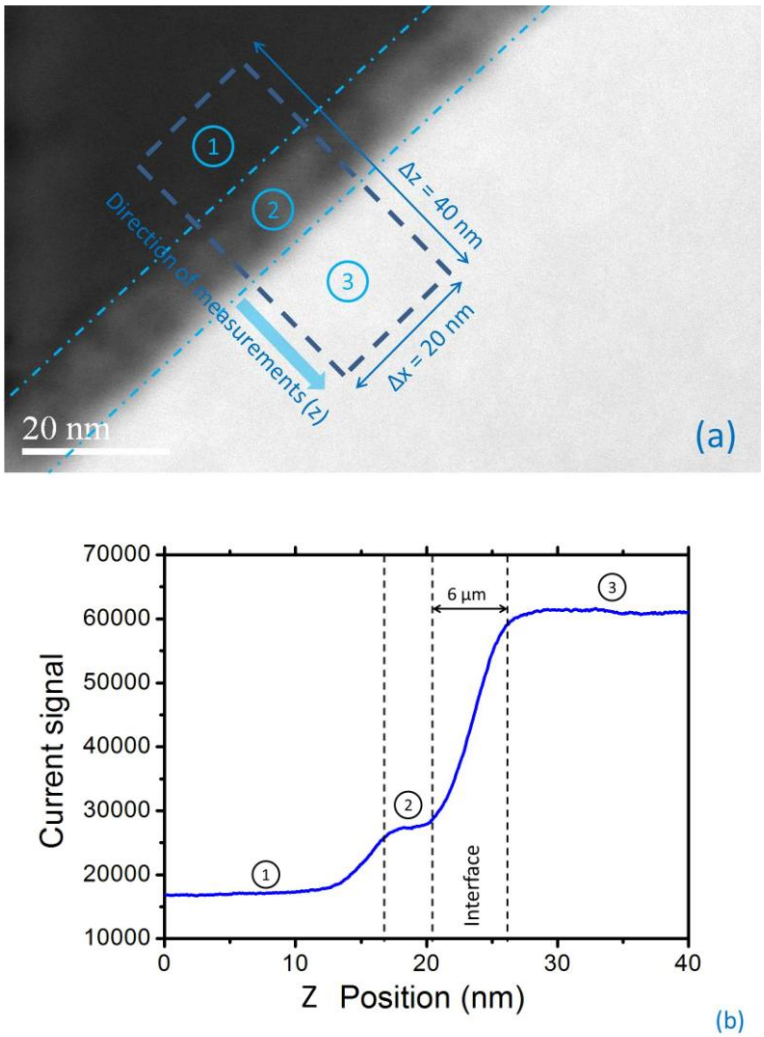

Figure 5.18 : (a)- HAADF STEM image of the oxide/non-oxide interface for the GaAs layer at lateral position D. The $Al_{0.92}$GaAs-oxide, GaAs-oxide, and non-oxidized GaAs are labelled as 1, 2, 3 in the image. (b)- average density profile along the line Δz (b). For each position z the detector current is average over the width Δx.

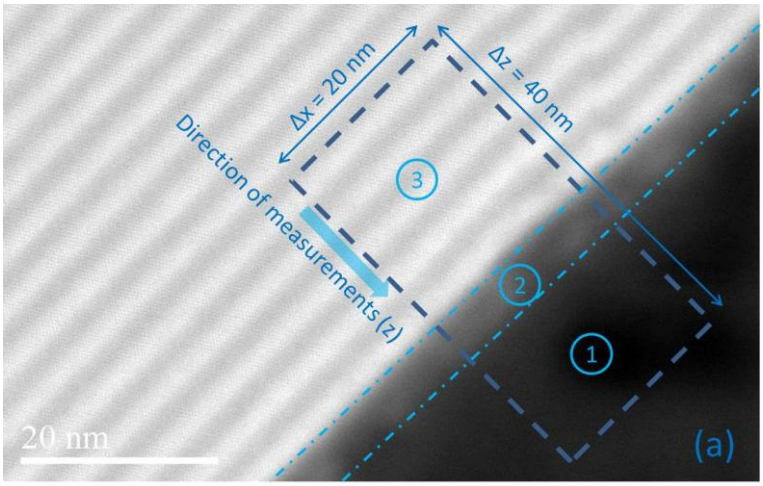

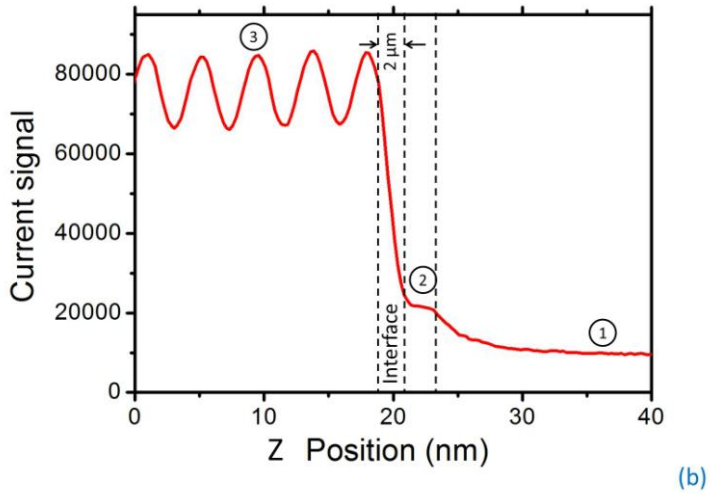

Figure 5.19 : (a)- HAADF STEM image of the oxide/non-oxide interface for the SL layer at lateral position C. The $Al_{0.92}GaAs$-oxide, SL-oxide, and non-oxidized SL are labelled as 1, 2, 3 in the image. (b)- average density profile along the line Δz (b). For each position z the detector current is average over the width Δx.

The HAADF STEM image of the $Al_{0.92}GaAs$/SL interface, and the corresponding average density profile are shown in Fig. 5.19 (a) and (b) for comparison. The STEM images of Fig. 5.17 (a), 5.18 (a), and 5.19 (a) correspond to the same lateral position (close to the mesa center). The SL layer was vertically-oxidized over one period only (Fig. 5.19 (a)), while the GaAs layer was oxidized over a depth of ~ 20 nm (Fig. 5.18 (a)). Moreover, the oxidation front is much flatter with the SL than in the two previous cases. Fig. 5.19 (b) shows that the roughness of the interface between un-oxidized and oxidized materials is at most of 2 nm with the SL layer.

The experimental results show that inserting a SL layer at the interface with the Al-rich oxidized layer slows down the vertical oxidation process, and allows to reduce the oxide/non-oxide interface roughness.

Although the SL is of higher average Al content than bulk $Al_{0.34}Ga_{0.66}As$ and GaAs, it has a higher resistance against the vertical oxidation compared with AlGaAs with lower Al content and GaAs which is contrary to the property of bulk material. The oxidation of superlattice happens period-by-period. The AlAs layer in SL was oxidized fast and the oxidation stopped always at the interface with the GaAs, not with AlAs. It means the high resistance comes from the interface of oxide/GaAs. Each thin GaAs layer requires an activation which slows down the oxidation process.

After oxidation, dislocation was found on the superlattice layer as shown in Fig. 5.20. This can be explained by the strain formed during oxidation process.

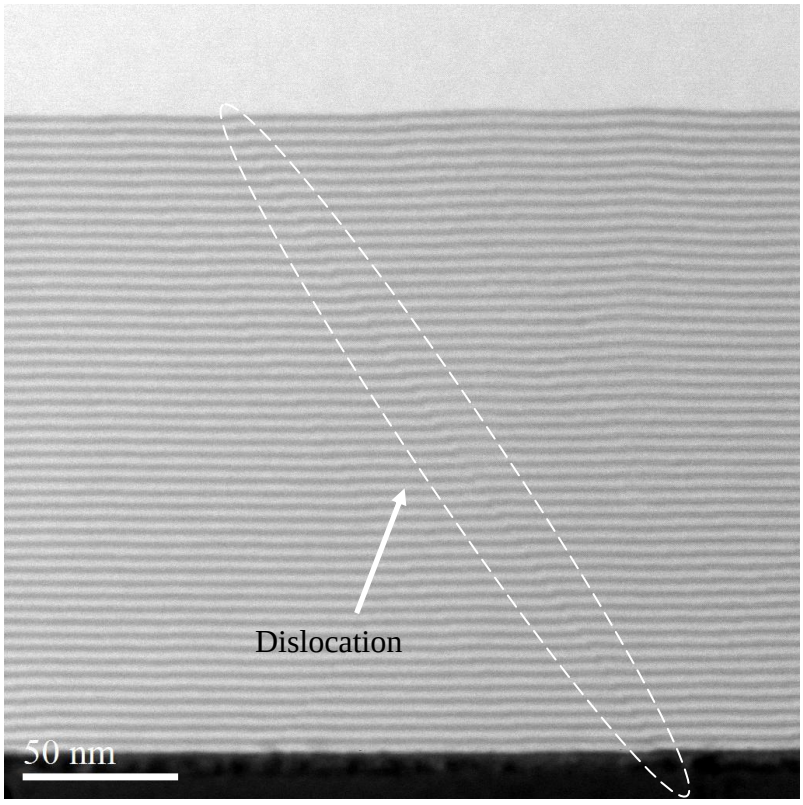

Fig. 5.20 HAADF STEM image of the SL layer after oxidation.

As shown in Fig. 5.21, the lateral oxidation reaches over 33 μm with a vertical oxidation length merely around 4μm from the sidewall showing the lateral oxidation has a priority over vertical oxidation. The vertical oxidation is not just a function of oxidation time and temperature. It also depends on the adjacent layer structure. It's not hard to imagine that the oxidation of neighboring high Al layer consumes much amount of reaction species and avoids the vertical oxidation for the most part of the region. The vertical oxidation only happens in a relatively short distance from the sidewall where the density of reaction species is relatively large.

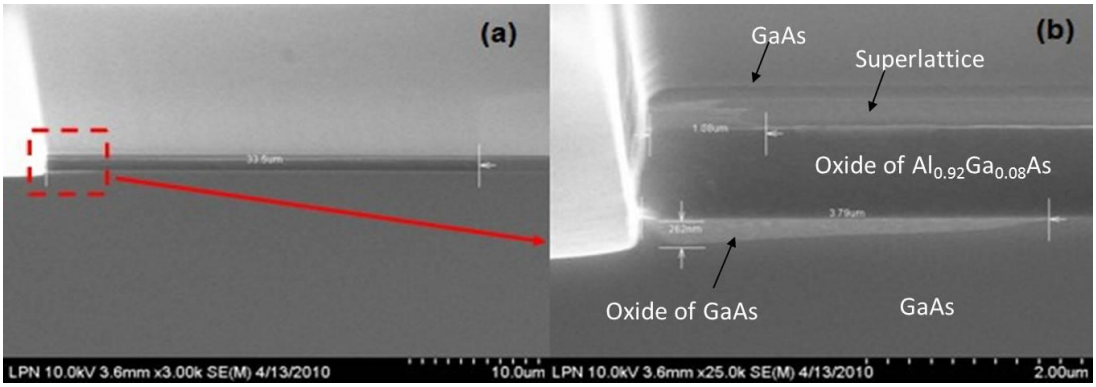

Fig. 5.21 SEM photos of the sample with 33μm lateral oxidation. (a) Lower magnification. (b) Higher magnification.

As for a 10μm mesa on the same sample as shown in Fig. 5.22, the lateral oxidation of high Al layer has long been finished and there are enough reaction species for the vertical oxidation. We can see from the photo, the oxidation of GaAs is much more considerable compared to Fig. 5.21. The depth of vertical oxidation of GaAs is not homogeneous reflecting the difference of oxidation time (the region near the sidewall) and the difference of density of reaction species (the center part).

From the comparison of Fig. 5.21 and Fig. 5.22, we can see the vertical oxidation strongly progressed after neighboring $Al_{0.92}Ga_{0.08}As$ was fully oxidized. Besides precisely controlling oxidation time, another possible way to curb the effect of vertical oxidation is to locate the waveguide upon a $Al_{0.92}Ga_{0.08}As$ layer not fully oxidized.

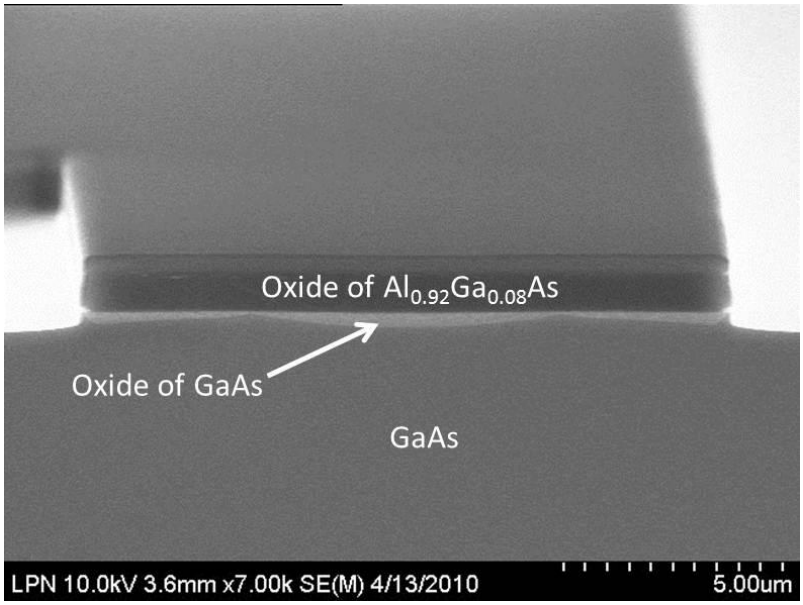

Fig. 5.22 SEM photos of a 10μm mesa of the same sample as Fig. 5.21.

5.2.3.3 EDX analysis

Energy Dispersive X-Ray spectroscopy (EDX), also referred to as EDS or EDAX, is an analytical x-ray technique used for identification of the elemental composition of materials. It relies on the investigation of an interaction of the material of a sample and a source of X-ray excitation. EDX characterization is due to the fundamental principle that each material element has a unique atomic structure corresponding to a unique set of peaks on its X-ray spectrum.

EDX systems are likely attached to SEM or TEM instruments where the imaging capability of the microscope identifies the samples of interest. The EDX technique is non-destructive and samples can be examined in situ with little or no sample preparation.

The EDX analysis has been performed at different regions around the oxidized samples described above to indentify the material. Fig. 5.23 illustrates the analysis results of the region already shown in Fig. 5.14. From the data we can confirm that the $Al_{0.34}Ga_{0.66}As$ layer near the interface has been oxidized with a high O atom percentage (~60 %) and low As atom percentages (less than 3 %).

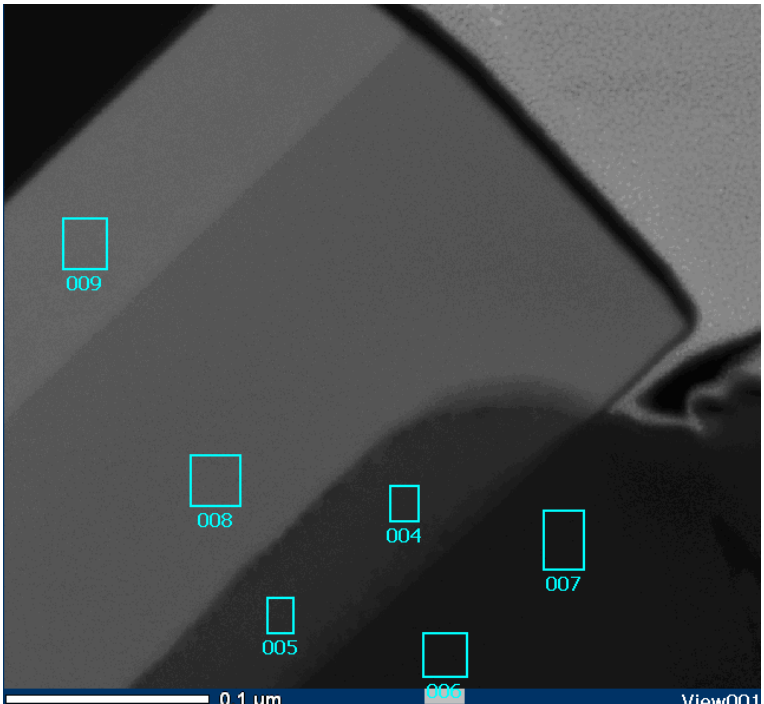

Memo	O	Al	Ga	As	Total(Atom%)
004	54.06	9.80	33.32	2.83	100.00
005	53.50	10.26	33.49	2.74	100.00
006	63.59	31.35	4.19	0.86	100.00
007	61.57	32.36	5.02	1.05	100.00
008	2.49	8.88	37.20	51.43	100.00
009	1.30	0.00	48.63	50.07	100.00

Fig. 5.23 EDX analysis at the region near the sidewall (position A in Fig. 5.16).

The SL layer was oxidized laterally with a much lower oxidation rate as mentioned before. The oxidation of SL layer was analyzed as shown in Fig. 5.24. A low average As percentage (1.47 %) of the layer indicates the SL has been fully oxidized. The oxidation of AlAs thin layers induced and activated the oxidation of neighboring GaAs layers. The different positions of the oxide of Al-rich layer were investigated and the oxide is homogeneous across the oxidation layer with a As percentage less than 1 % as shown in Fig. 5.24.

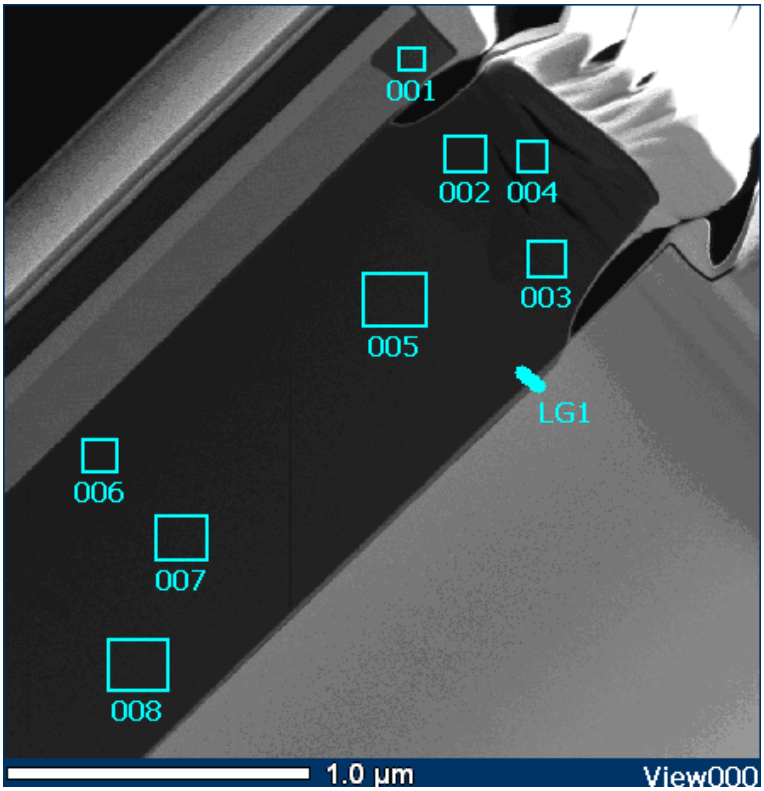

Memo	O	Al	Ga	As	Total(Atom%)
001	65.58	12.89	20.06	1.47	100.00
002	71.79	25.01	2.69	0.51	100.00
003	73.03	23.55	2.92	0.50	100.00
004	69.20	26.52	3.30	0.98	100.00
005	72.91	23.63	3.16	0.30	100.00
006	72.75	23.57	3.28	0.40	100.00
007	74.97	22.11	2.53	0.39	100.00
008	72.69	24.33	2.92	0.07	100.00

Fig. 5.24 EDX analysis on SL samples already shown in Fig. 5.19.

The interface of oxide and GaAs was investigated shown in Fig. 5.25 where EDX analysis was performed step by step. The layer in the middle of the photo is with low Al and As but high O content. It is the oxide of GaAs layer. From this analysis, the transition length from oxide to GaAs is less than 10nm with a typical spatial resolution of ~3 nm using the EDX spectroscopy. This transition length is consistent with the interface analysis in last section.

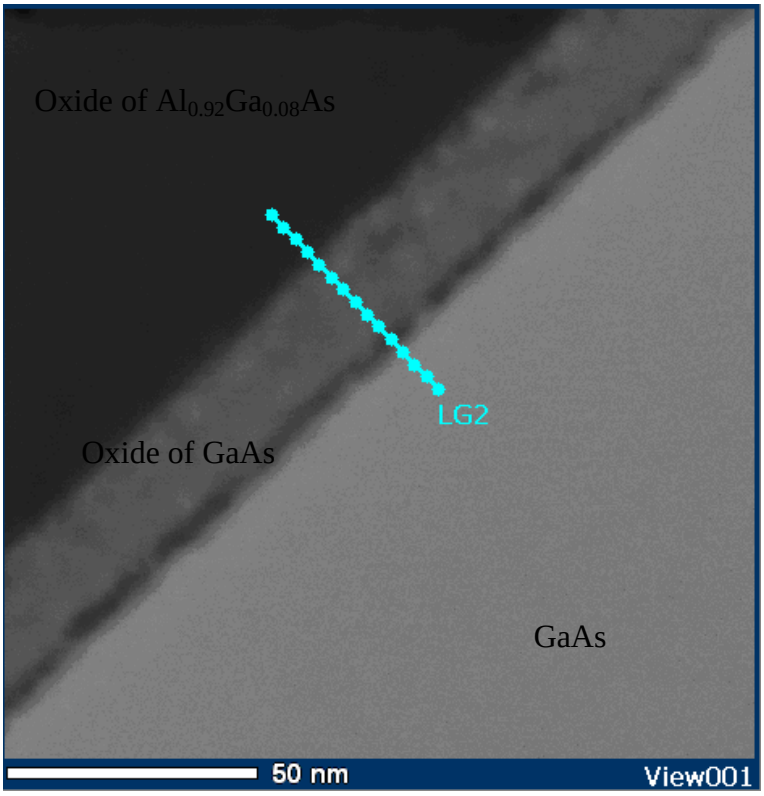

Memo	O	Al	Ga	As	Total(Atom%)
LG20000 ; 0.000 nm	64.58	29.82	5.48	0.11	100.00
LG20001 ; 3.448 nm	69.17	27.12	3.64	0.08	100.00
LG20002 ; 6.897 nm	58.29	34.63	6.88	0.20	100.00
LG20003 ; 10.345 nm	57.88	27.85	11.09	3.18	100.00
LG20004 ; 13.793 nm	41.32	17.91	36.09	4.68	100.00
LG20005 ; 17.242 nm	35.00	9.38	52.80	2.82	100.00
LG20006 ; 20.690 nm	51.93	2.90	40.18	4.99	100.00
LG20007 ; 24.138 nm	59.67	0.96	37.35	2.02	100.00
LG20008 ; 27.587 nm	52.07	0.63	43.44	3.86	100.00
LG20009 ; 31.035 nm	46.67	0.65	42.01	10.68	100.00
LG20010 ; 34.483 nm	23.67	0.00	40.89	35.43	100.00
LG20011 ; 37.932 nm	11.28	0.00	44.27	44.45	100.00
LG20012 ; 41.380 nm	4.95	0.00	48.63	46.42	100.00
LG20013 ; 44.828 nm	4.44	0.02	48.54	47.00	100.00
LG20014 ; 48.277 nm	3.20	0.00	48.86	47.95	100.00

Fig. 5.25 EDX analysis at the interface of oxide and GaAs.

The oxidation front of the high Al layer is also investigated as shown in Fig. 5.26. We can see the transition from oxide to AlGaAs is less than 10 nm consistent with other analysis mentioned above.

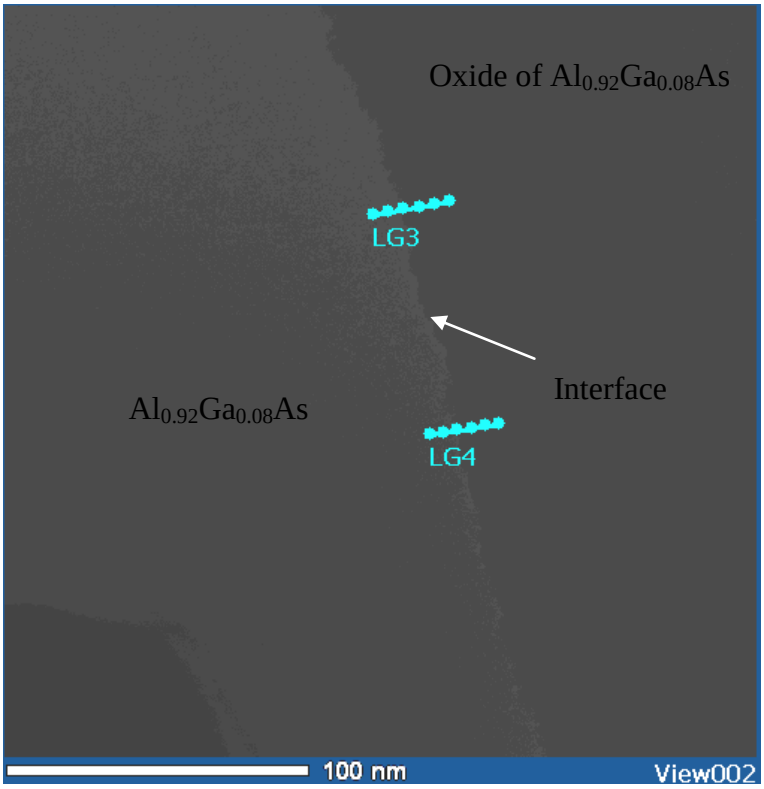

Memo	O	Al	Ga	As	Total(Atom%)
LG40000 ; 0.000 nm	10.10	21.96	8.05	59.89	100.00
LG40001 ; 4.694 nm	27.93	7.83	1.37	62.87	100.00
LG40002 ; 9.388 nm	36.10	45.15	3.76	14.99	100.00
LG40003 ; 14.082 nm	76.48	21.06	2.41	0.05	100.00
LG40004 ; 18.776 nm	65.57	30.33	4.02	0.08	100.00
LG40005 ; 23.470 nm	68.60	25.82	5.46	0.11	100.00
LG30000 ; 0.000 nm	8.19	22.29	10.75	58.78	100.00
LG30001 ; 5.146 nm	7.54	12.71	8.55	71.20	100.00
LG30002 ; 10.293 nm	28.44	48.45	7.02	16.09	100.00
LG30003 ; 15.439 nm	63.84	26.56	4.64	4.96	100.00
LG30004 ; 20.586 nm	57.13	38.84	1.16	2.86	100.00
LG30005 ; 25.732 nm	38.96	53.32	7.56	0.16	100.00

Fig. 5.26 EDX analysis at the oxidation front (interface of oxide and $Al_{0.92}Ga_{0.08}As$).

5.2.3.4 Vertical oxidation rate calibration of GaAs

The oxidation rate ratio was also studied experimentally. The similar fabrication process was used with the GaAs etching process controlled to leave 100 nm $Al_{0.92}Ga_{0.08}As$ on top of GaAs layer. The wet oxidation of $Al_{0.92}Ga_{0.08}As$ progressed through the sidewalls of the mesa and the $Al_{0.92}Ga_{0.08}As$ surface. After the remaining of the top $Al_{0.92}Ga_{0.08}As$ was fully oxidized the under GaAs layer was oxidized continuously. For the SEM images of the mesa, the oxidation rates of the lateral $Al_{0.92}Ga_{0.08}As$ layer were measured at different temperatures. At the same time, from the SEM images as shown in Fig. 5.27, the oxidized GaAs layer was also measured. Consequently, the lateral oxidation rate of $Al_{0.92}Ga_{0.08}As$ and the vertical oxidation rate of GaAs were obtained as shown in table 5.2.

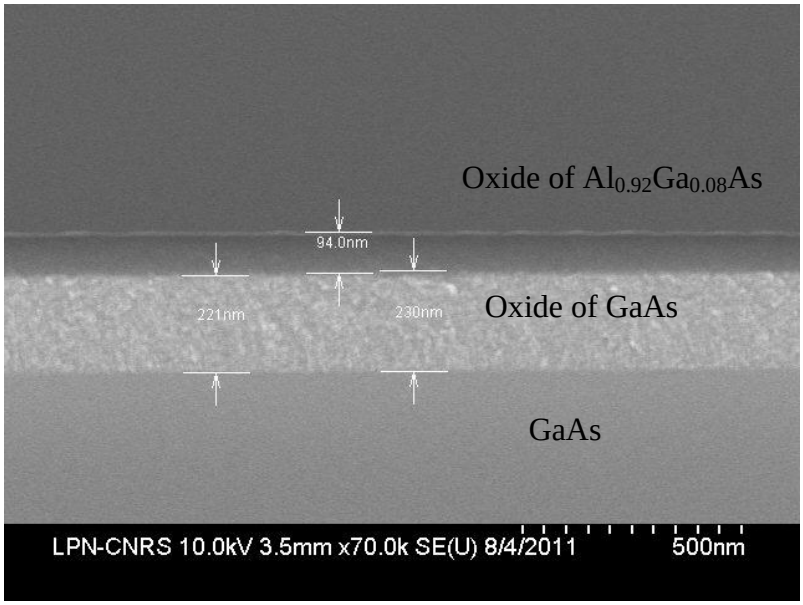

Fig. 5.27 Cross section image of the sample oxidized from the surface at 460 ℃, 40 min

Temperature	400℃	440℃	460℃
Lateral Oxidation rate of $Al_{0.92}Ga_{0.08}As$	4μm/h	19μm/h	34μm/h
Vertical Oxidation rate of GaAs	80nm/h	230nm/h	335nm/h
Oxidation rate of $Al_{0.92}Ga_{0.08}As$ over GaAs	50	82	101

Table 5.2. Lateral oxidation rate of $Al_{0.92}Ga_{0.08}As$ and vertical oxidation rate of GaAs at different temperatures.

To minimize the vertical oxidation at a given lateral oxidation length, a higher temperature seems preferred according to the table 5.2. However, the oxidation process is practically controlled by oxidation time and the higher oxidation temperature brings difficulty to precisely controlling of the oxidation depth. Therefore, the temperature should be carefully chosen depending on different applications.

5.3 Effect of H_2 plasma treatment in wet oxidation

Apparently, the oxidation of the neighboring high-Al-content layer activated the oxidation of GaAs or low-Al-content AlGaAs layer. The key role of hydrogen in wet oxidation has been reported [13] and high residual H concentration allows for an enhanced kinetics of wet oxidation [12]. In this part, we investigated experimentally the role of hydrogen in the oxidation of GaAs and low-Al-content AlGaAs.

5.3.1 Fabrication of samples

To study the role of hydrogen during the oxidation of GaAs, GaAs substrate wafers were used. The samples were etched by RIE (with $SiCl_4$) or IBE (with Ar). Some samples were

hydrogenated after surface etching and prior to oxidation, in radio-frequency hydrogen plasma. These samples were exposed to the 80 W hydrogen plasma for 2 h, at 200 ℃, under vacuum conditions. Another sample without any hydrogenation treatment is used for comparison.

The sample etched by RIE is fabricated as follows:

1 Sample: GaAs n+ substrate
Process: 1 Photolithography to define 2 μm lines 2 Deposit Au 200 nm as mask 3 Lift off to remove the photo resist. 4 $SiCl_4$ RIE etching ~1.6 μm 5 With or without H_2 plasma at 200 ℃ for 3 h Oxidation at 420 ℃ for 3 h

The sample etched by IBE is fabricated as follows:

2 Sample: GaAs n+ substrate
Process: 1 Photolithography to define 4 μm lines 2 Etching by IBE ~300 nm (Ar ion etching) 3 Remove resist 4 With/Without H_2 plasma at 200 ℃ for 3 h Oxidation at 420 ℃ for 2 h 45 min

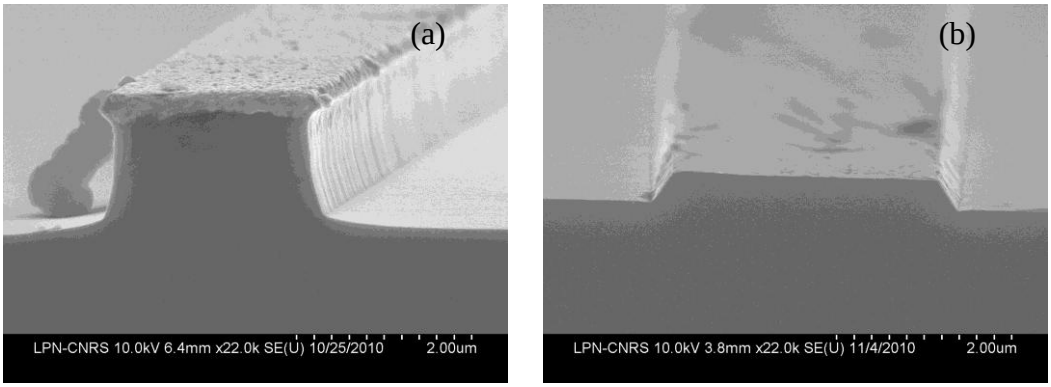

Fig. 5.28 Cross section images of GaAs substrates etched by RIE (a) and by IBE (b).

5.3.2 Experimental results and discussion

The samples were observed by SEM. The etched surface by RIE was oxidized after H_2 plasma treatment. The plain surface and the sidewall of the ridge were shown in Fig. 5.29 (a) and (b), respectively. The oxidation depth at the plain surface is around 120 nm.

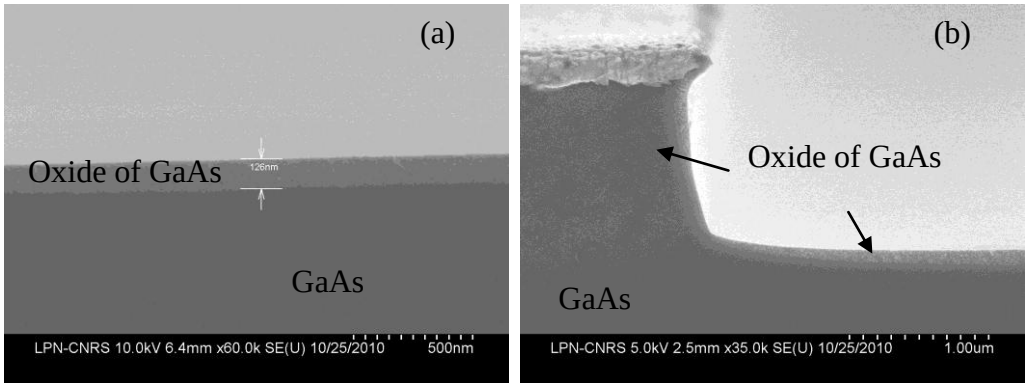

Fig. 5.29 SEM photos of cross section of samples: oxidation at the etching surface (a) and sidewall (b) after RIE etching and H treatment.

The etched surface by IBE was also oxidized after H_2 plasma treatment. The plan surface and the sidewall of the ridge were shown in Fig. 5.30 (a) and (b). The etched ridge was easier to be oxidized compared to the plain surface with an oxidation depth over 240 nm. However, the surface was not oxidized homogeneously. Scattered oxidized spots were found with different oxidation depth in the order of several tens of nanometers as shown in Fig. 5.30(a).

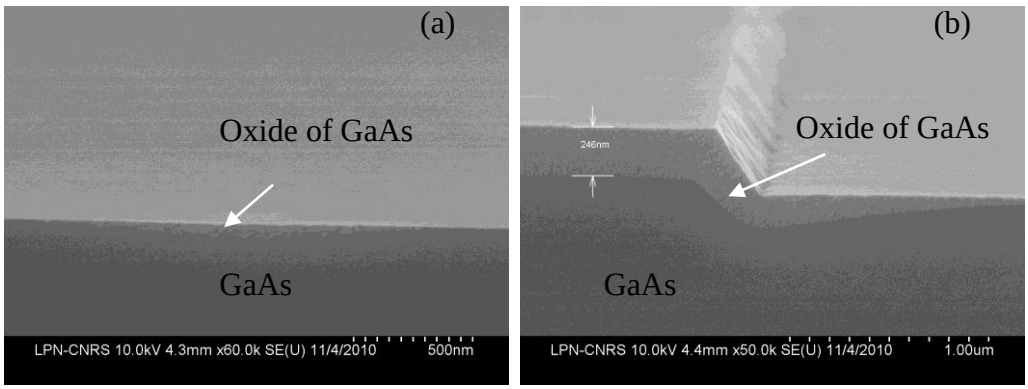

Fig. 5.30 oxidation at the surface (a) and the sidewall (b) after IBE etching and H treatment.

For comparison, the oxidation of GaAs did not happen to all the samples without H_2 plasma treatment as shown in Fig. 5.31 which is consistent to all the wet oxidation results reported before. Meanwhile, a GaAs substrate without any etching cannot be oxidized even with H_2 plasma.

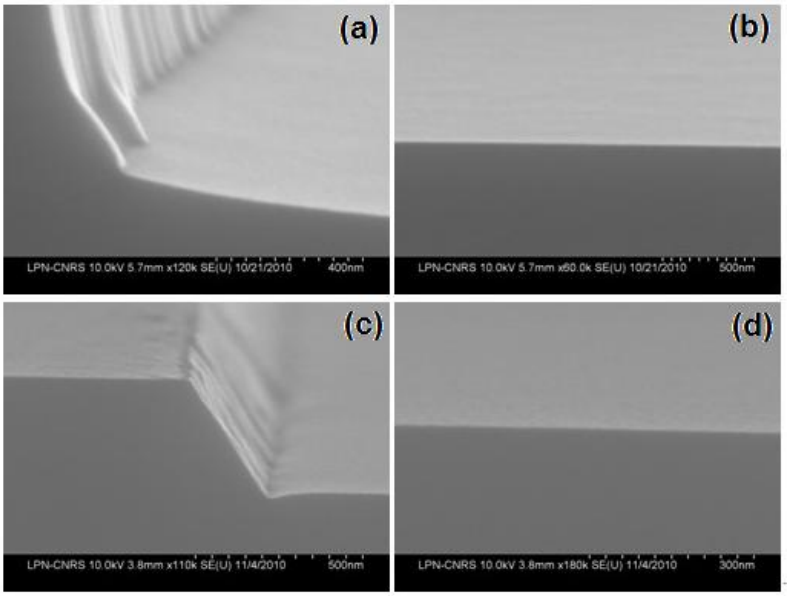

Fig. 5.31 (a) Oxidation at the corner after RIE etching without H treatment. (b) Oxidation at the etching surface after RIE etching without H treatment. (c) Oxidation at the corner after IBE etching without H treatment. (d) Oxidation at the etching surface after IBE etching without H treatment.

According to the results, hydrogen plays a key role in the wet oxidation of GaAs. The oxidation happened to the two dry etched samples with H_2 plasma treatment. The oxidation seems not from the etching species because the RIE and IBE etching are totally different. Especially, IBE etching is only physical bombard with Ar ion beam without introducing any chemical contamination. In contrast, the surface state can be critical for the residual hydrogen amount. A possibility was that the etched surfaces had morphology more suitable for the H implantation and permitted higher H amount at the surface.

However, the oxidation process was more difficult to take place for IBE etched plain surface. The possible explanation is that the etched surface by IBE is rather smooth. The activation of oxidation only happened at some spots. As for the sidewall the ridge, the roughness was apparently larger.

5.4 Conclusion

In summary, the vertical oxidation of GaAs or AlGaAs with low Al content activated by a neighboring oxidized Al-rich AlGaAs layer has been demonstrated experimentally. STEM observation clearly showed that the oxidation of GaAs and AlGaAs with low Al content came from the interface with the oxidized Al-rich AlGaAs layer. EDX analysis showed that As was completely removed from the vertically oxidized layer, indicating that the oxidation process was nearly complete. The vertical oxidation causes unexpected oxidation of the adjacent layers and brought additional roughness at the oxide/non-oxide interfaces which is detrimental to the fabrication of optical waveguides. A SL structure was proposed in order to limit the vertical oxidation. The SL showed a higher resistance against the

oxidation through the interface than bulk $Al_{0.34}Ga_{0.66}As$, and even than bulk GaAs. The vertical oxidation of the SL was period-by-period and could be limited to ~4 nm. By using SL structure instead of standard bulk material, the oxide/non-oxide interface was also improved. Hydrogen plasma treatment of a dry-etched GaAs surface allowed for the oxidation of bulk GaAs, which showed the key role of hydrogen incorporation in the activation of the oxidation process for GaAs or AlGaAs materials with low Al content. The production of hydrogen in a neighboring oxidized Al-rich AlGaAs layer and subsequent hydrogen diffusion through the interface was proposed as a possible mechanism accounting for the activation of the vertical oxidation observed in the GaAs/AlGaAs epitaxial structures.

Reference

[1] E. Katz, "Oxidation," in VLSI Technology, S. M. Sze, Ed. New York: McGraw-Hill, ch. 4, 1983.

[2] C. W. Wilmsen, "Oxide/III-V compound semiconductor interfaces," in Physics and Chemistry of III-V Compound Semiconductor Interfaces, C. W. Wilmsen, Ed. New York: Plenum, ch. 7, 1985.

[3] J. M. Dallesasse, N. El-Zein, N. Holonyak, Jr., K. C. Hsieh, R. D. Burnham, and R. D. Dupuis, "Environmental degradation of AlxGa1-xAs-GaAs quantum well heterostructures," J. Appl. Phys., 68, 2235-2238, 1990.

[4] J. M. Dallesasse, N. Holonyak, Jr., A. R. Sugg, T. A. Richard, and N. El-Zein, "Hydrolyzation oxidation of AlxGa1-xAs-AlAs-GaAs quantum well heterostructures and superlattices," Appl. Phys. Lett., 57, 2844-2846, 1990.

[5] D. L. Huffaker, D. G. Deppe, K. Kumar, and T. J. Rogers, "Native-oxide defined ring contact for low threshold vertical-cavity lasers," Appl. Phys. Lett., 65, 97-99, 1994.

[6] K. D. Choquette, K. L. Lear, R. P. Schneider, Jr., and K. M. Geib, "Cavity characteristics of selectively oxidized vertical-cavity lasers", Appl. Phys. Lett.,66, 3413-3415, 1995.

[7] F. A. Kish, S. J. Caracci, N. Holonyak, Jr, J. M. Dallesasse, K. C. Hsieh, M. J. Ries, S.C. Smith, and R. D. Burnham, "Planar native-oxide index-guided AlxGa1-xAs-GaAs quantum well heterostructure lasers," Appl. Phys. Lett., 59, 1755-1757, 1991.

[8] A. Fiore, V. Berger, E. Rosencher, N. Laurent, S. Theilmann, N. Vodjani, and J. Nagle, "Huge birefringence in selectively oxidized GaAs/AlAs optical waveguides," Appl. Phys. Lett., 68, 1320-1322, 1996.

[9] M. H. MacDougal, P. D. Dapkus, A. E. Bond, C.-K. Lin, and J. Geske, "Design and fabrication of VCSELs with AlxOy-GaAs DBRs," IEEE J. Sel. Top. Quantum Electron., 3, 905-915, 1997.

[10] L. Scaccabarozzi, M. M. Fejer, Y. Huo, S. Fan, X. Yu, and J. S. Harris, "Enhanced second-harmonic generation in AlGaAs/AlxOy tightly confining waveguides and resonant cavities," Opt. Lett., 31, 3626-3628, 2006.

[11] M. Ravaro, M. Le Dû, J.-P. Likforman, S. Ducci, V. Berger, and G. Leo, "Estimation of parametric gain in GaAs/AlOx waveguides by fluorescence and second harmonic generation measurements," Appl. Phys. Lett., 91, 191110, 2007.

[12] E. Guillotel, M. Ravaro, F. Ghiglieno, C. Langlois, C. Ricolleau, S. Ducci, I Favero, and G. Leo, "Parametric amplification in GaAs/AlO_x waveguide," Appl. Phys. Lett., 94, 171110, 2009.

[13] K. D. Choquette, K. M. Geib, H. C. Chul, B. E. Hammons, H. Q. Hou, and R. Hull, "selective oxidation of buried AlGaAs versus AlAs layers," Appl. Phys. Lett., 69, 1385-1387, 1996.

[14] H. Q. Jia, H. Chen, W. C. Wang, W. X. Wang, W. Li, Q. Huang, J. Zhou, and Q. K. Xue, "Improved thermal stabilityof wet oxidized AlAs," Appl. Phys. Lett., 80, 974-976, 2002.

[15] M. Le Dû, I. Sagnes, G. Beaudoin, L. Travers, J.-C. Esnault, and J.-C. Harmand, "Enhanced kinetics of $Al_{0.97}Ga_{0.03}As$ wet oxidation through the use of hydrogenation," Appl. Phys. Lett., 89, 111105, 2006.

[16] C. I. H. Ashby, J. P. Sullivan, K. D. Choquette, K. M. Geib, and H. Q. Hou, "Wet oxidation of AlGaAs: The role of hydrogen," J. Appl. Phys., 82, 3134-3136, 1997.

[17] A. C. Alonzo, X.-C. Cheng, and T. C. McGill, "Strain in wet thermally oxidized square and circular mesas," J. Appl. Phys., 87, 4594-4599, 2000.

[18] K. M. Geib, K. D. Choquette, H. Q. Hou, and B. E. Hammons, "Fabrication issues of oxide-confined VCSEL's, " in vertical-cavity surface emitting lasers, K. D. Choquette and D. Deppe, Eds., Proc. SPIE, 3003, 69-74, 1997.

[19] S. Guha, F. Agahi, B. Pezeshki, J. A. Kash, D. W. Kisher, and N. A. Bojarczuk, "Microstructure of AlGaAs - oxide heterolayers formed by wet oxidation," Appl. Phys. Lett., 68, 906-908, 1996.

[20] R. Y. Li, Z. G. Wang, B. Xu, P. Jin, X. Guo, M. Chen, "Interface of wet oxidized AlGaAs/GaAs distributed Bragg reflectors," Appl. Phys. A., 86, 19-21, 2007.

[21] T. Langenfelder, St. Schroder, and H. Grothe, "Lateral oxidation of buried AlxGa1-xAs layers in a wet ambient," J. Appl. Phys., 82, 3548-3551,1997.

[22] R. S. Burton, and T. E. Schlesinger, "Wet thermal oxidation of AlxGa1-xAs compounds," J. Appl. Phys., 76, 5503-5507, 1994.

[23] W. T. Tsang, "Self-terminating thermal oxidation of AlAs cpilayers grown on GaAs by molecular beam epitaxy," Appl. Phys. Lett., 33, 426-429, 1978.

[24] N. Holonyak, Jr, and J. M. Dallesasse, U.S. Patent 5 262 360, 1993.

[25] K. D. Choquette, K. M. Geib, C. I. H. Ashby, R. D. Twesten, O. Blum, H. Q. Hou, D. M. Follstaedt, B. E. Hammons, D. Mathes, and R. Hull, "Advances in selective wet oxidation of AlGaAs Alloys," IEEE Journal of selected topics in quantum electronics, 3, 916-926, 1997.

[26] T. Takamori, K. Takemasa, and T. Kamijoh, "Interface structure of selectively oxidized AlAs/GaAs," Appl. Phys. Lett., 69, 659-661, 1996.

[27] R. D. Twesten, D. M. Follstaedt, K. D. Choquette, and R. P. Schneider, Jr, "Microstructure of laterally oxidized AlxGa1-xAs layers in vertical-cavity lasers," Appl. Phys. Lett., 69, 19-21, 1996.

[28] W. Ranke, Y. R. Xing and G. D. Shen, "Orientation dependence of oxygen adsorption on a cylindrical GaAs crystal," J. Vas. Sci. Technol., 21, 426-428, 1962.

[29] K. D. Choquette, K. L. Lear, P. R., Schneider, Jr., K. M. Geib, J. J. Figiel, and R. Hull, "Wavelength insensitive performance of robust selectively oxidized vertical-cabity lasers," Photon. Technol. Lett., 7, 1237-1239, 1995.

[30] J. H. Kim, D. H. Lim, K. S. Kim, G. M. Yang, K. Y. Lim, and H. J. Lee, "Lateral wet oxidation of $Al_xGa_{1-x}As$ - GaAs depending on its structures", Appl. Phys. Lett., 69, 3357-3359, 1996.

[31] R. L. Naone and L. A. Coldren, "Surface energy model for the thickness dependence of the lateral oxidation of AlAs," J. Appl. Phys., 82, 2277-2280, 1997.

[32] F. A. Kish, S. A. Maranowski, G. E. Hbfler, N. Holonyak, Jr., S. J. Caracci, J. M. Dallesasse and K. C. Hsieh, "Dependence on doing type (p/n) of the water vapor oxidation of high-gap AlxGa1-xAs," Appl. Phys. Lett., 60, 3165-3167, 1992.

[33] W. Shockley and J. L. Moll, "Solubility of heavily-doped semiconductor," Physical Review, 119, 1480-1482, 1960.

[34] B. E. Deal and A. S. Grove, "General relationship for the thermal oxidation of silicon," J. Appl. Phys., 36, 3770-3778, 1965.

[35] M. Ochiai, G. E. Giudice, and H. Temkin, J. W. Scott and T. M. Cockerill, "Kinetics of thermal oxidation of AlAs in water vapor," Appl. Phys. Lett., 68, 1898-1900, 1996.

[36] G. W. Pickrell, J. H. Epple, K. L. Chang, K. C. Hsieh, and K. Y. Cheng, "Improvement of wet-oxidized $Al_xGa_{1-x}As$ (x~1) through the use of AlAs/GaAs digital alloys," Appl. Phys. Lett., 76, 2544-2546, 2000.

[37] K. M. Geib, K. D. Choquette, H. Q. Hou, and B. E. Hammons, "Fabrication issues of oxide-confined VCSEL's," in Vertical-Cavity Surface Emitting Lasers, K. D. Choquette and D. Deppe, Eds., Proc. SPIE, 3003, 69-74, 1997.

[38] I. Suarez, G. Almuneau, M. Condé, A. Arnoult, and C. Fontaine, "Optimal control of AlAs oxidation via digital alloy heterostructure compositions", J. Phys. D: Appl. Phys., 42, 175105, 2009.

CHAPTER 6

Design, fabrication and characterization of waveguides and laser based on GaAs/AlGaAs

To build monolithic integrated sensor on GaAs/AlGaAs, the first step is to build high quality waveguide with high sensitivity. The waveguide working on TM mode with high-index contrast and tight confinement (~200 nm Si core on SOI) shows high sensitivity to the ambient solution [1]. Besides SOI platform, wet oxidation of AlGaAs offers an approach to realize similar high-index-contrast structures on GaAs/AlGaAs platform as on SOI. Wet oxidation has been applied for waveguide applications especially on nonlinear structures [2-5].

Meanwhile, laser source working on TM mode is required given TM mode is preferable than TE mode in sensing applications [1]. According to the literature [6-8], tensile-stained quantum wells (GaAsP) permit laser diode working on TM mode rather than conventional TE mode.

In this chapter we explore the tightly confining optical waveguide and TM laser on GaAs/AlGaAs/GaAsP system in parallel. The propagation loss of the waveguide based on wet oxidation process has been measured by Fabry-Perot method at 830 nm and 1550 nm. Meanwhile, a Laser diode using tensile-strained quantum wells has been demonstrated working on TM mode.

6.1 Waveguides based on GaAs/AlGaAs material system

6.1.1 Design and fabrication

The waveguide structures are shown in Fig. 6.1. The core layer $Al_{0.34}Ga_{0.66}As$ is on the oxidized $Al_{0.92}Ga_{0.08}As$ layer. The thickness of the core layer is critical for the sensitivity of the sensing waveguide. According to the calculation of sensitivity versus the thickness, the optimized thickness of $Al_{0.34}Ga_{0.66}As$ core layer is around 100 nm which allows a ratio between the ayalyte index change and the effective index change around 37 % on TM mode. However, smaller thickness and tight confinement cause larger losses. Furthermore, the vertical oxidation mentioned above reduces the thickness of the core layer during the oxidation of the high Al cladding layer. Consequently, in this experiment the core layer is set to 150 nm. Both standard and SL structures are grown by MBE at LPN detailed in table 6.1 and 6.2. Three pairs of SL layers were added between $Al_{0.34}Ga_{0.66}As$ and $Al_{0.92}Ga_{0.08}As$. To achieve single mode operation, the width of the core should not be larger than 300 nm. The cladding $Al_{0.92}Ga_{0.08}As$ layer is oxidized to obtain tight confinement.

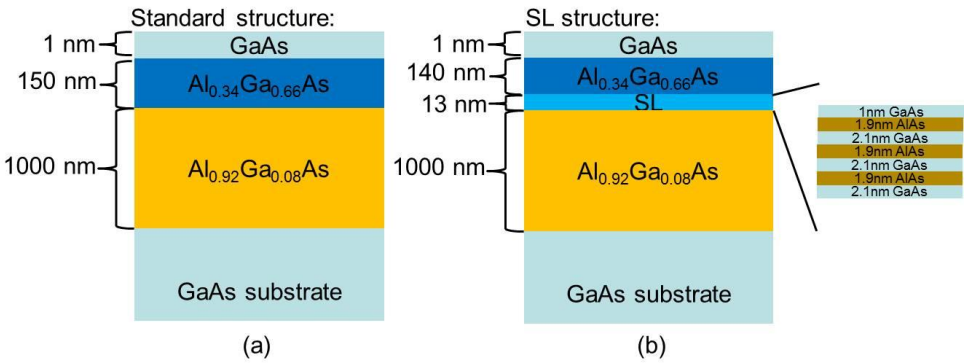

Fig. 6.1 Schematic of the standard (a) and SL (b) wafer structures.

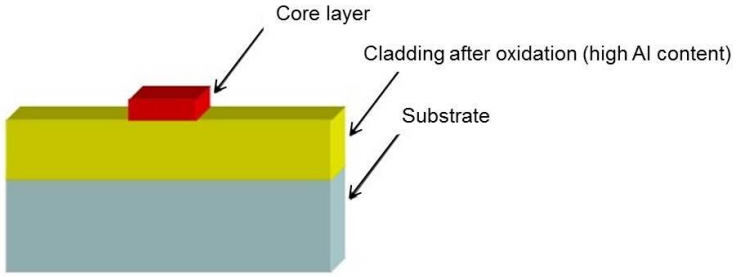

Fig. 6.2 Schematic of waveguide fabricated by etching and oxidation from surface referred to as technology A.

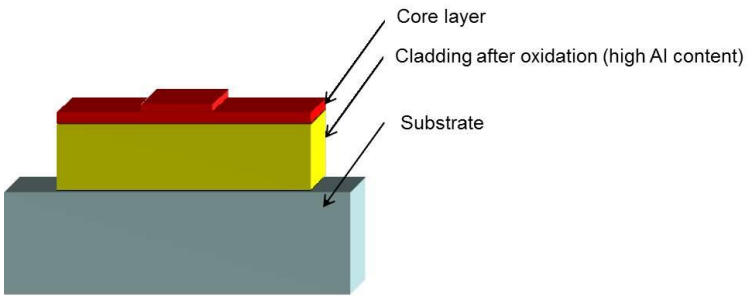

Fig. 6.3 Schematic of waveguide fabricated by oxidation of the mesa and etching of waveguide referred to as technology B.

As shown in Fig. 6.2 and Fig. 6.3, two fabrication processes can be used referred to as technology A and technology B.

Technology A:

1) EBL to define lines range from 0.3 μm to 2.0 μm wide
2) Etch the waveguide by ICP or RIE around 200 nm deep
3) Remove resist
4) Oxidation from the interface

Backside thinning and cleavage

Technology B:

1) Define the 20 μm wide mesa by photolithography
2) Etch mesa with depth ~1.5 μm
3) Remove the resist
4) Oxidation of the mesa from sidewall
5) Define the waveguide of 2 μm wide by photolithography
6) Etch the waveguide by ICP or RIE
7) Backside thinning and cleavage

Layer n°	Description	%Al	Thickness	Doping
3	GaAs surface protection	0	1nm	undoped
2	$Al_{0.34}Ga_{0.66}As$	34%	150nm	undoped
1	$Al_{0.92}Ga_{0.08}As$	92%	1000nm	undoped
0	GaAs buffer	0	200nm	undoped
	GaAs substrate			n doped

Table 6.1 layer structure of standard wafer.

Layer n°	Description	%Al	Thickness	Doping
10	GaAs surface protection	0	1nm	undoped
9	$Al_{0.34}Ga_{0.66}As$	34%	140nm	undoped
8	GaAs	0	1nm	undoped
7	AlAs	100%	1.9nm	undoped
6	GaAs	0	2.1nm	undoped
5	AlAs	100%	1.9nm	undoped
4	GaAs	0	2.1nm	undoped
3	AlAs	100%	1.9nm	undoped
2	GaAs	0	2.1nm	undoped
1	$Al_{0.92}Ga_{0.08}As$	92%	1000nm	undoped
0	GaAs buffer	0	200nm	undoped
	GaAs substrate			n doped

Table 6.2 layer structure of SL wafer.

6.1.2 Propagation loss characterization

In this part, the Fabry-Pérot (FP) method is introduced at first. It is for propagation loss measurement on single-mode waveguide but in some condition, multimode waveguide is also suitable for this method. The propagation losses of the oxidized waveguides have been measured by Fabry-Perot method at 830 nm and 1550 nm.

6.1.2.1 Fabry-Pérot method

This technique allows loss evaluation of single-mode waveguides. The knowledge of modal facet reflectivity is required to deduce the loss value and the precision of this value influence critically the measurement accuracy.

Given the reflectivity at input and output facets, the transmission of a waveguide can be treated analogously to that of a Fabry-Pérot resonator in plane-wave approximation. In a single-mode waveguide, the transmission is given by the Airy function

$$T_{FP} = \frac{T^2 e^{-\alpha L}}{(1-R')^2 + 4R'\sin^2(\phi/2)}\eta \tag{6.1}$$

where α is the modal attenuation coefficient, L is the length of waveguide, η is the coupling efficiency, and T ,R is the transmission and reflectivity of the two facets respectively, and $R' = \mathrm{R}\cdot \mathrm{e}\,xp(-\alpha L)$.

The transmission T_{FP}, is a periodic function with the free spectrum range (FSR) as

$$\mathrm{FSR} = |\Delta\lambda| = |\lambda_{p+1} - \lambda_p| = \frac{\lambda^2}{2Ln_{eff}[1-\frac{\lambda}{n_{eff}}\frac{dn_{eff}}{d\lambda}]} \tag{6.2}$$

By tuning the input wavelength or the effective index (by e.g. changing the sample temperature), T_{FP} oscillates between a maximum T_{max} and a minimum T_{min} that depend only on R'. By measuring the contrast of the transmission fringes related to the coefficient C defined as T_{min}/T_{max}, the attenuation coefficient can finally be calculated as.

$$\alpha L = -\ln[\frac{1+C}{R(1-C)}(1-\sqrt{1-(\frac{1-C}{1+C})^2}] \tag{6.3}$$

In single-mode weakly confining waveguides, R is approximated by the Fresnel formula as

$$R = (\frac{n_{eff}-1}{n_{eff}+1})^2 \tag{6.4}$$

However, especially for narrow ridges with tight confinement, three dimensional (3D) finite-difference time domain (FDTD) simulations are the most suitable tool to calculate the reflectivity.

This method is extended to the case of multimode semiconductor waveguides by Alfredo De Rossi et al [9]. In the multimode case, total transmission is given by the superposition of several Airy functions, corresponding to each excited mode. Normally, these modes have different amplitudes and different periodicities since the effective indices are not the same. By optimizing the coupling on the fundamental mode, the corresponding Airy function beats the others. In spite of that, the fringe contrast of the signal is reduced,

because of partial power coupled into higher-order modes which results in a considerable error in the loss coefficient measurement by this approach. Nevertheless, precision can be greatly improved under some conditions:

- The fringes of different Airy functions corresponding to different modes must have the same contrast. In this case, if they are all in phase, the total contrast represents the contrast of a single Airy function. To achieve this situation, all the guided modes must have the same reflectivity and the same loss coefficient. The former condition is reasonably fulfilled if the waveguide is multimode only in the horizontal direction; the latter, if roughness on the ridge sidewalls is negligible and scattering does not depend on the breadth of the modal distribution [10].

- The waveguide must have only few modes in the horizontal direction: in this case, by measuring the transmission over a sufficient spectral range, the Airy functions can be found all in phase at a certain wavelength. In this case, a broad band source or a tunable laser diode can be employed to find the maximum contrast in several tens of microns.

In practice, these conditions can hardly be perfectly satisfied. Typically, ridge semiconductor waveguides usually have more than two modes in the horizontal direction. In addition, their reflectivity and loss coefficient are not exactly identical. However, if most of the input power is coupled into the fundamental mode and the scan range is larger enough, the more these conditions are approximated, the better is the accuracy attained.

6.1.2.2 Measurement setup and method

The setup of the measurement is shown in Fig. 6.4. The light was first focused by an objective on the facet of the sample and the output signal collected by another objective was coupled into fibre for the measurement by OSA. The resolution of the OSA is 50 pm. A polarizer is employed to control the polarization state for TE mode or TM mode measurements.

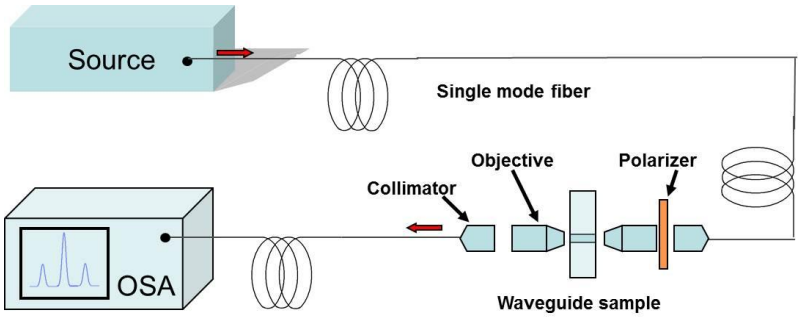

Fig. 6.4 Schematic of optical loss measurement setup.

The source we used in the measurement is Exalos830 SLED and Exalos1550 SLED. The total output power is 3 mW and 10 mW respectively. Fig. 6.5 shows a spectrum of an Exalos830 source.

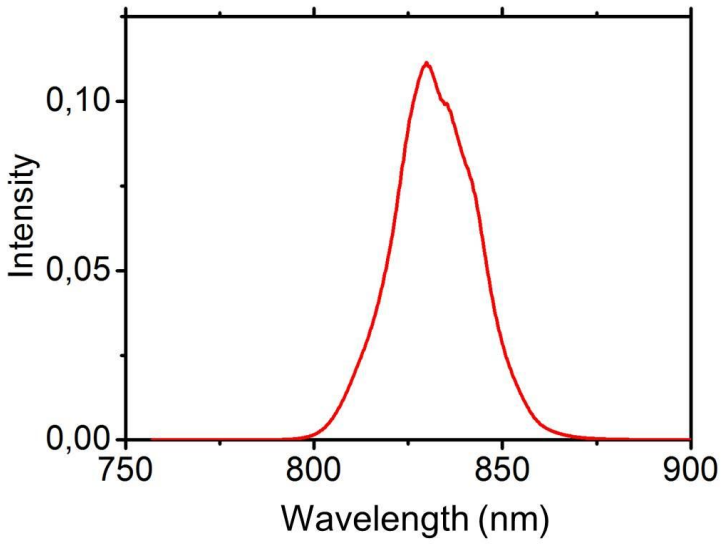

Fig. 6.5. Spectrum of the Exalos830 source

A typical measurement spectrum with TE mode is shown in Fig. 6.6. The coefficient *C* is obtained by measuring the T_{max} and T_{min} of each fringe. To reduce measurement error, *C* is an average value of several periods. The contrast varies with the wavelength because of the coexistence of multimode in the waveguide. The measurement is performed in a long wavelength range (50 nm in this experiment) to spot the largest contrast where all the modes are in-phase. The loss value is then calculated by the largest *C*.

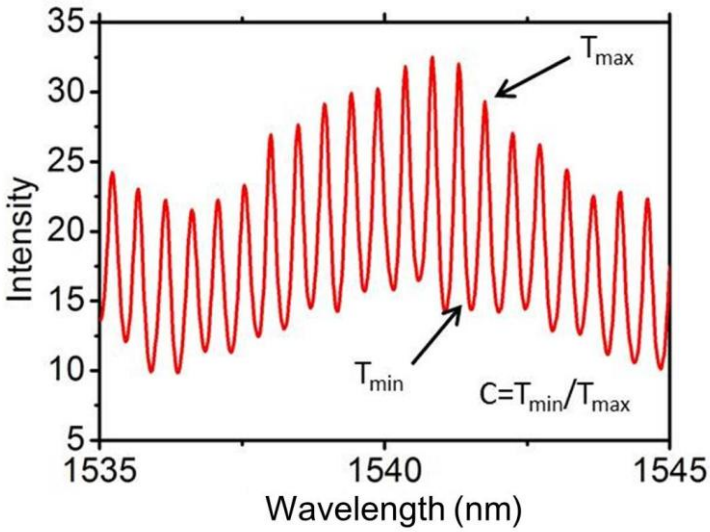

Fig. 6.6. A typical measurement spectrum with TE mode of an 810 μm-long waveguide at 1540 nm.

An alternative approach is using tuneable laser and power meter instead of broad band source and OSA. The objective can be replaced by lens fibre which is easier for coupling optimization.

6.1.2.3 Measurement at 1550 nm with TE mode

The samples are processed as listed in table 6.3 for the measurement at 1550 nm. AAR22E is based on standard structure. AAR29K and AAR34M are fabricated with different process based on SL structure.

	Structure	Process	Oxidation temperature	Oxidation time	Etching	Mask	Width of WG
AAR22E	Standard	A	470 ℃	2 min	ICP	Ebeam	2 μm
AAR29K	SL	A	470 ℃	9 min	ICP	Ebeam	2 μm
AAR34M	SL	B	470 ℃	20 min	ICP	Photolithography	2 μm/20 μm (mesa)

Table 6.3. The samples for the measurement at 1550 nm.

AAR34M was fabricated by etching the mesa before the waveguide referred to as technology B. The waveguide is located in the center of the mesa. The data is shown in table 6.4.

Length (μm)	207	810	1220	1610
C (Tmin/Tmax)	0.39-0.40	0.49	0.55	0.61
FSR(pm)	1835	480	312	238
Group index	3.16	3.09	3.16	3.13
Output power(nW)	30-40	20-25	15-20	15-20
Reflectivity value R	**0.25**	**Loss value**		**18.5 dB/cm**

Table 6.4. the measurement data of waveguides on AAR34M at 1550nm.

We measured samples with different lengths. These samples should share the same loss value. The reflectivity of the facet can be deduced from these data. As shown in Fig. 6.7, the correct reflectivity value allows the same loss value for the samples with different lengths. The R value fitting better this criterion is around 0.25. The corresponding loss value is 18.5 dB/cm.

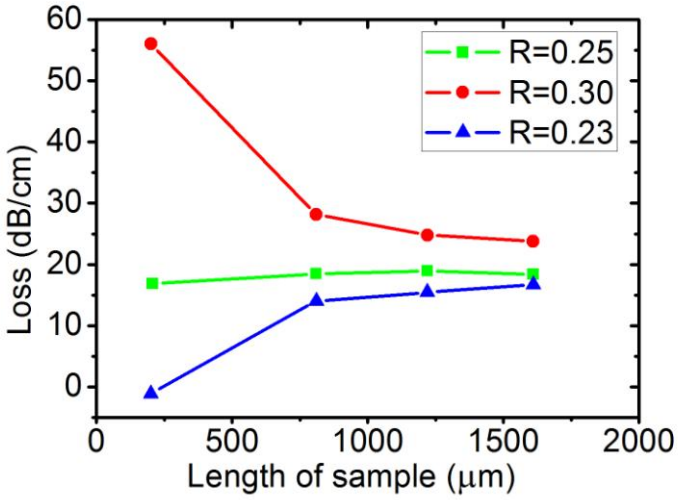

Fig. 6.7. Reflectivity fitting for different lengths of waveguides on AAR34M.

Similarly, the measurement of AAR22E is shown in table 6.5. The reflectivity is the same as that of AAR34M. The loss value is 18 dB/cm which is close to the loss value of the AAR34M. Another sample AAR29E fabricated by the same process as AAR22E and on SL structure was also measured showing no significant difference of the loss value for standard structure and SL structure at 1550 nm. The loss value is not far from the measurement in literature on a similar structure [2].

Length (μm)	420	790	1210	1620
C (Tmin/Tmax)	0.39-0.42	0.48	0.54	0.60-0.61
FSR(pm)	900	480	322	243
Group index	3.18	3.17	3.08	3.05
Output power(nW)	30-40	30	20-25	15-20
Reflectivity value R	**0.25**	**Loss value**		**18 dB/cm**

Table 6.5 the measurement data of waveguides on AAR22E at 1550 nm.

One over-oxidized sample AAR29K was measured. The over-oxidized time was 7 min. The loss value is 40 dB/cm showing the degradation of over oxidization.

6.1.2.4 Measurement at 830 nm

The loss values at 830 nm were also measured. Since the loss at 830 nm is much larger than at 1550 nm, the size of the waveguide must be short. Hence, we cannot measure different lengths and deduce the reflectivity. Instead, we calculate the value by 3 dimension FDTD simulation and the results are shown in table 6.6.

Width of waveguide (μm)	Reflectivity with TE mode	Reflectivity with TM mode
0.3	0.30	0.274
0.5	0.254	0.32
0.7	0.29	0.32
1.0	0.33	0.31
1.5	0.375	0.30
2.0	0.39	0.30

Table 6.6 Reflectivity calculated by 3D FDTD simulation.

2μm wide waveguides on AAR22E and AAR34M were measured according to the calculated reflection on the facet as shown in table 6.7. The loss value of waveguide on AAR22E was around 150 dB/cm which is much larger than that at 1550 nm. In contrast, the waveguide on AAR34M failed to transmit through the sample as short as 200 μm indicating huge loss or absorption.

	AAR22E	AAR34M	AAR22H	AAR29H
Process	A	B	A	A
Length (μm)	200	200	200	200
Oxidation temperature (℃)	470	470	470	470
Oxidation time(min)	2	20	4	4
Structure	Standard	SL	Standard	SL
Etching	ICP	ICP	ICP	ICP
Mask	Ebeam	Photolithography	Ebeam	Ebeam
Coefficient C (T_{min}/T_{max})	0.45	--	0.5	Not regular
Output power (nw)	>10	nothing	10	2
Loss (dB/cm)	150	--	180	--

Table 6.7 the measurement data of waveguides with TE mode at 830 nm.

As a comparison, the standard (n°AAR22H) and SL (n°AAR29H) samples fabricated in the same batch were measured. The loss value of standard sample AAR22H (180 dB/cm) is larger than that of AAR22E (150 dB/cm) which could be explained by the addition roughness of the interface and the reduction of the thickness of core layer induced by the over oxidation. However, the SL samples always had irregular fringes and lower output power compared with standard samples. The exact loss value can't be achieved by this approach.

The loss value with TM mode cannot be achieved because of the irregular fringes as shown in Fig. 6.8. Due to the irregular fringe with wrong FSR, the exact loss value of SL sample can't be achieved by this approach. For the TE mode measurements on standard sample, the contrast of the fringes shifts with wavelength. As discussed above, a maximum contrast along a wide range of wavelength should be close to the real value. Here the FWHM of the source is around 30 nm which is a limit for detection of the maximum contrast. During the

measurements, the regularity of the fringes depended hugely on the focus adjustment which is consistent with the discussion above. The focus must be optimized for the maximum coupling to the fundamental mode of the waveguide which is the key condition for applying this approach to multimode waveguides.

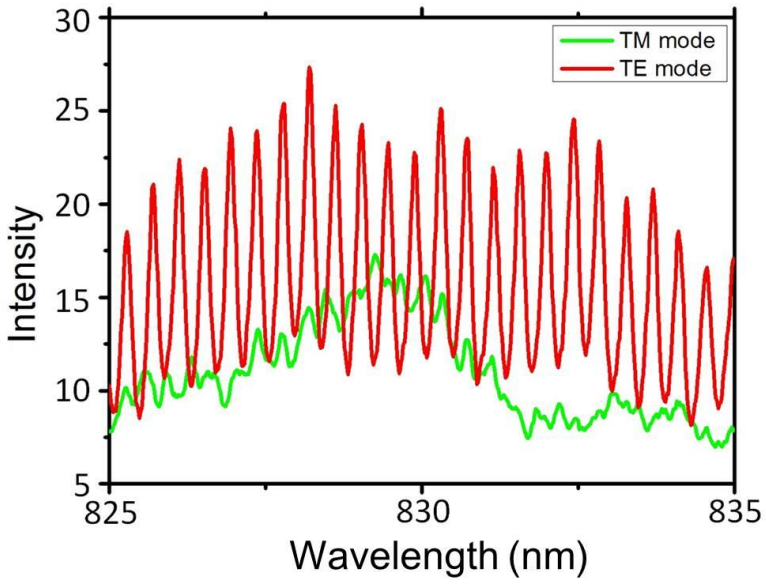

Fig. 6.8 TE and TM mode of 1.5 µm waveguide with a length of 200 µm.

The measurement of narrow waveguides of 0.5 and 0.3 µm were performed with the best loss value in the order of 100 dB/cm and 200 dB/cm, respectively.

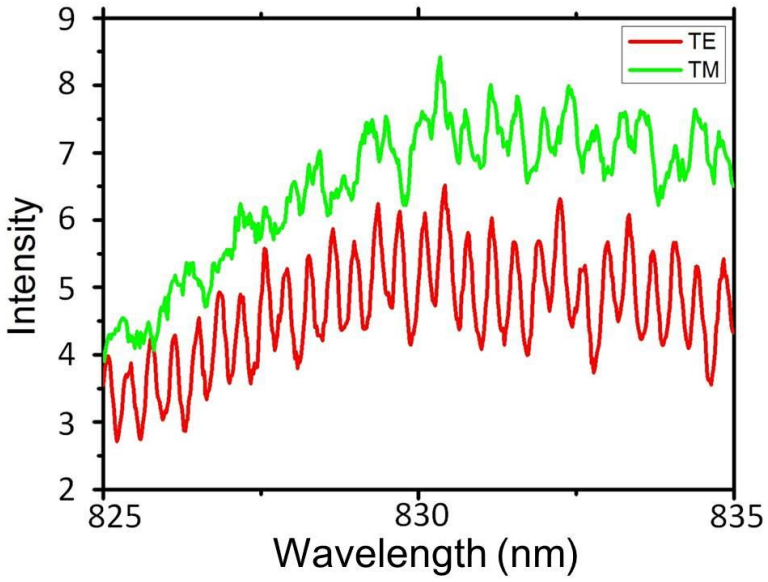

Fig. 6.9. Signal of TE and TM mode of 0.3 µm with a length of 200 µm

Fig. 6.9 shows the measurements of 0.3 μm waveguide. The TM mode signal was higher than TE mode because the scattering loss from the sidewall became dominant in this case so the TE mode suffered more loss than TM mode.

From the standard sample measurements, the best performance was on the largest waveguide in terms of output power and contrast. It can be explained by higher coupling coefficient and lower model distribution at the sidewall. However, From the SL sample measurement, one phenomenon should be noted that the best performance was on a waveguide around narrower waveguide like 0.7 or 0.5 μm.

6.1.3 Discussion of the loss measurements

The error of measurements comes from several parts. Firstly, the reflection calculation error from 3D FDTD simulation infects the loss value tremendously. Secondly, the spectrum range of the source may not large enough to find the maximum contrast position. Thirdly, the coupling condition is critical for the measurement.

- Despite the error during the calculation of facet reflectivity, the waveguides at 830 nm are of great propagation loss which can be recognized qualitatively by the dramatic decay with the waveguide length.

- The fringes were measured carefully along 50 nm spectrum range. The contrast varies as a function of wavelength and the maximum value is obtained by averaging several adjacent fringes.

- The coupling condition is rather tricky. However, this error can be diminished by careful adjustment and measuring multiple samples on an array.

The loss coefficients measured at 1550 nm are around 18 dB/cm for 2 μm-wide waveguides on standard and SL samples which is similar to the loss value (23 dB/cm) of tight confined waveguide with buried Al_xO_y layer in the literature [2]. The loss could come from the surface or interface roughness, the roughness or the sidewall and the measurement error. Over-oxidation increased the loss value by the vertical oxidation effect introduced in chapter 5. This could come from the roughness caused by vertical oxidation or the reduction of the thickness of the core layer.

The loss values measured at 830 nm are much larger than at 1550 nm. The loss of 2 μm-wide waveguides on TE mode and standard sample is in order of 150 dB/cm. The loss value on TM mode and SL samples are not measurable by the present approach. The loss of narrower waveguides of 0.5 μm and 0.3 μm on TE mode and standard structure were also measured in order of 100 dB/cm and 200 dB/cm.

The huge difference of the loss values between 1550 nm and 830 nm measurements could be due to the dependence of scattering loss on working wavelength [11]. The scattering loss could come from the roughness of sidewalls and the surface and interface.

- The surface was cleaned by oxygen plasma before oxidation to remove the residue of photoresist for technology A. In the case of technology B, the oxygen plasma was performed as the final step. The surface is smooth by SEM observation.

- The loss measurements were mostly on 2 µm-wide waveguides to reduce the effect of the sidewall roughness. The wet etching with very smooth surface was performed as an alternative approach to dry etching. However, no difference was found between wet etched and dry etched samples.

- The interface of oxide/non-oxide could play a main role to the high loss at 830 nm. The roughness at the interface has been shown in last chapter. Besides, the oxide studied by STEM showed different contrasts from the image indicating possible density variation (see Fig. 6.10). The contrast difference also happened along the interface.

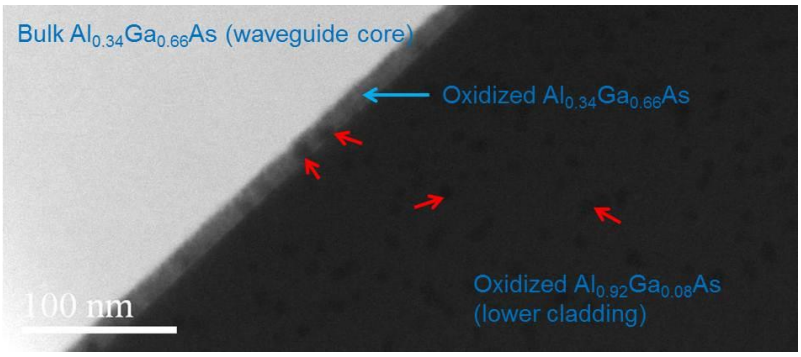

Fig. 6.10 HAADF STEM cross-sectional image of the standard oxidized sample. The variations of the contrast were marked by red arrows.

The failure to measure loss value of TM mode could be due to the much higher loss of TM mode and the difficult alignment of the measurement system in vertical direction. Especially, the SL structure has a problem at 830 nm.

- One possibility is that the SL structure has absorption at this wavelength which can explain why narrower waveguides perform better that larger waveguides. When the SL layer is oxidized partially, the absorption is not uniform resulting in irregular fringes of the measurement. The waveguides on AAR34M fabricated by technology B had flat oxidation interface as shown in Fig. 5.20. The absorption of the remaining SL layer can be the reason for the missing transmission.

- Another possibility is that the SL structure has a mechanical problem. There are micro defects or cracks produced during the oxidation process or the measurement process. These defects or cracks increased the scattering loss of the waveguide and induced the irregular fringes of the measurement.

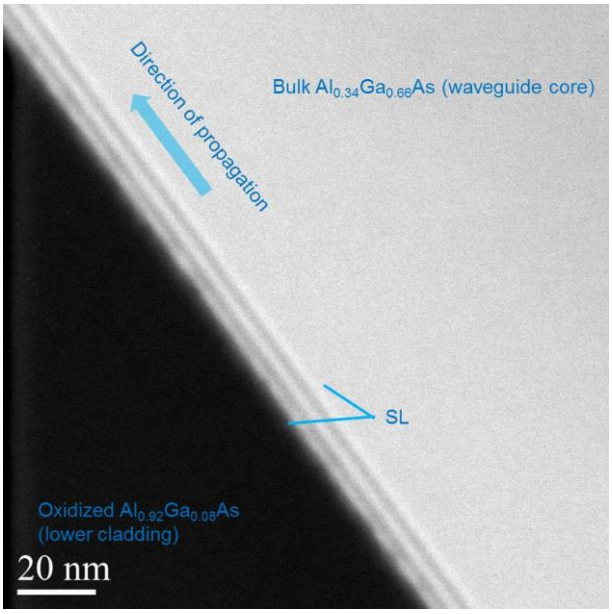

Fig. 6.11 HAADF STEM image of the oxide/SL interface for the sample AAR29E. The waveguide was fabricated by technology A. The cross-sectional image is along the direction of the light propagation

To investigate the interface of SL/oxide, the FIB laminas were prepared along the propagation direction of the waveguide. If the interface of SL has mechanical gaps or defects the 7-µm-long FIB laminas may accidentally encounter some discontinuity of interface. However, we did not find any noticeable defects or gaps from the STEM observation (see Fig. 6.11). The high loss of SL samples is still not clear.

6.2 Fabrication and characterization of FP laser working on TM mode based on GaAs/GaAsP/AlGaAs

According to the literature [6-8], tensile-stained quantum wells permit laser diode working on TM mode rather than conventional TE mode. The tensile-strain and quantum-size effects counter each other in modifying the relative level of the heavy-hole (HH) and light-hole (LH) bands. The combination of tensile strain and quantum confinement thus results in the HH being the highest valence band state, in degenerate LH and HH state, or in the LH being the highest state, depending on the relative strengths of the two effects. When the tensile-strain effect is dominant, leading to a highest LH band and TM mode operation which is a unique feature of tensile-strained QW devices [8]. The strain depends on the content of P in the GaAsP quantum well. The TM mode operation was demonstrated with P percentage ranging from 5 % to 22 % in QWs [6, 8].

Since TM mode is superior to TE mode in terms of sensitivity, we fabricated and characterized FP laser diode working on TM mode.

6.2.1 Fabrication

The active region of the wafer for laser fabrication (96P165) consists of 3 tensile-strain QWs of $GaAsP_{10\%}$. The layer structure is shown in table 6.8.

Layer n°	Description	%Al	Thickness	Doping
12	GaAs top contact	0	200nm	p++(2×10e19 cm-3)
11	$Al_{0.85}Ga_{0.15}As$ top cladding	85%	750 nm	p+ (2×10e18 cm-3)
10	$Al_{0.85}Ga_{0.15}As$ top cladding	85%	250 nm	p+ (5×10e17 cm-3)
9	$Al_{0.34}Ga_{0.66}As$	34%	35 nm	undoped
8	$GaAsP_{10\%}$ QW	0	9 nm	undoped
7	$Al_{0.34}Ga_{0.66}As$ Barrier	34%	5 nm	undoped
6	$GaAsP_{10\%}$ QW	0	9 nm	undoped
5	$Al_{0.34}Ga_{0.66}As$ Barrier Barrier	34%	5 nm	undoped
4	$GaAsP_{10\%}$ QW	0	9 nm	undoped
3	$Al_{0.34}Ga_{0.66}As$	34%	35 nm	undoped
2	$Al_{0.85}Ga_{0.15}As$ bottom cladding	85%	250 nm	n+ (5×10e17 cm-3)
1	$Al_{0.85}Ga_{0.15}As$ bottom cladding	85%	750 nm	n+ (2×10e18 cm-3)
0	GaAs buffer			n+ (3×10e18 cm-3)
	GaAs substrate			n doped

Table. 6.8. Layer structure of 96P165.

Another structure without the quantum wells layer (AAR28), as shown in table 6.9, was also grown by MBE to test the contact and the fabrication process.

Layer n°	description	%Al	thickness	doping
4	GaAs top contact	0	150nm	p++ (> 10e19cm-3)
3	$Al_{0.85}Ga_{0.15}As$ top cladding	85%	1000 nm	p+ (2×10e18 cm-3)
2	$Al_{0.34}Ga_{0.66}As$ core layer	34%	150 nm	undoped
1	$Al_{0.92}Ga_{0.08}As$ bottom cladding	92%	1000 nm	n+ (2×10e18 cm-3)
0	GaAs buffer			n+ (3×10e18 cm-3)
	GaAs substrate			n doped (n++)

Table. 6.9. Layer structure of AAR28.

The FP laser chip was fabricated by standard procedure and the fabrication process as shown in Fig. 6.12 is described in detail as follows:

Process:

1) Photolithography (negative tone resist) to define the pattern.
2) Metallization to form the electrode. (Ti 20nm, Au 400nm)
3) Lift-off to remove the resist.
4) ICP dry etching to shape the ridge (Etch depth around 1000nm).
5) Planarization by SU-8 or BCB.
6) Photolithography to define the electrode pattern.
7) Metallization to deposit the electrode on top surface.
8) Lift-off to remove the resist.
9) Back side thinning.
10) Back side electrode deposition.
11) Annealing at 400 ℃ and cleaving.

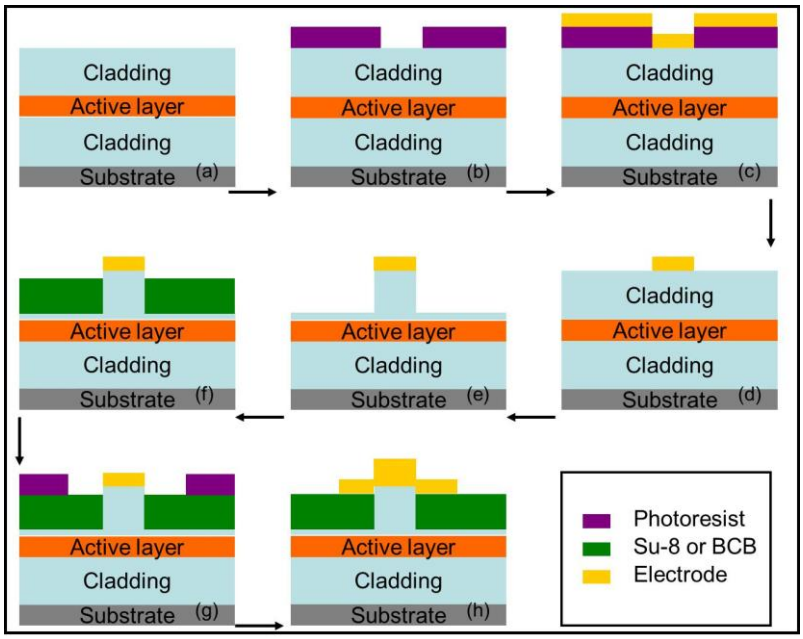

Fig. 6.12. Fabrication process of laser diode on GaAs system.

The fabrication process is the same for AAR28 and 96P165. The cross section of the laser diode is shown in Fig. 6.13.

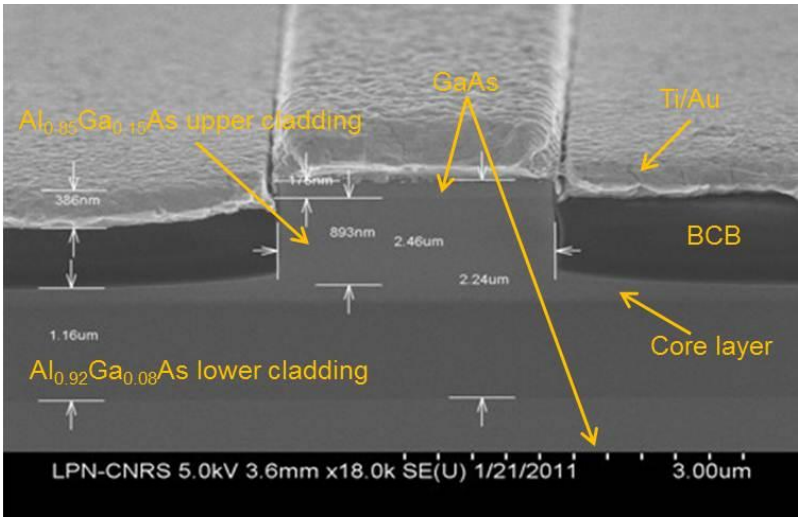

Fig. 6.13. SEM photo of the cross section of the laser diode.

6.2.2 Characterization

The VI curve and RI curve of the test wafer (AAR28) were measured and shown in Fig. 6.14. The turn-on voltage is around 2 V and the resistance is in the order of 10 Ω which are typical value of the laser diode. The tested waveguide is 3μm wide and 933 μm long. For getting a current density of 1 kA/cm^2, the current injection should be 28 mA.

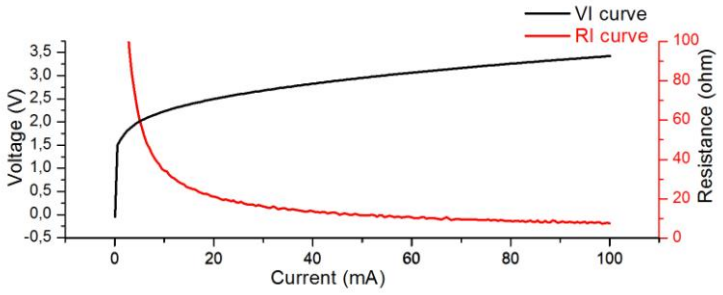

Fig. 6.14. Electrical measurement of AAR28 ridge waveguide

We also measured the resistance of the backside contact. After the anealing the resistance is less than 1 Ω and it means the backside contact only has a minor influence on the overall resistance.

The VI curve of 96P165 ridge with the same fabrication process was measured and compared with that of AAR28 as shown in Fig. 6.15. The turn-on voltage of 96P165 was around 3 V which is apparently higher than that of AAR28. The RI curves of the two samples show no difference (see Fig. 6.16) which means the contact condition is similar. The central wavelength of the laser was around 810 nm equal to 1.53 eV.

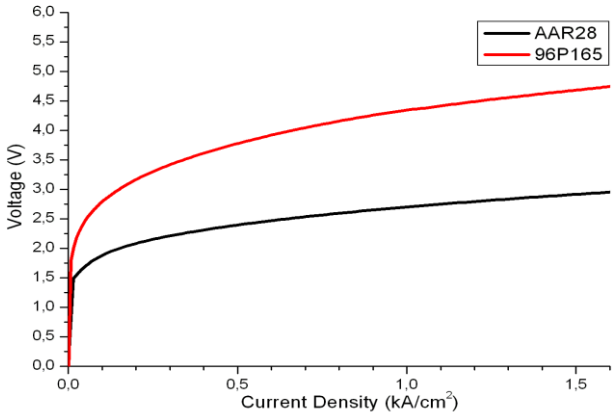

Fig. 6.15. VI curves of AAR28 and 96P165 ridge waveguide

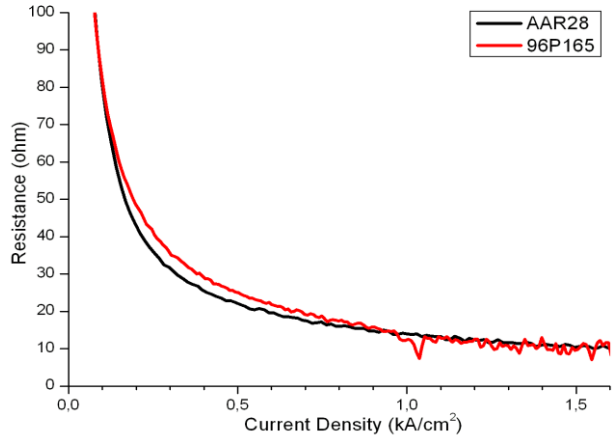

Fig. 6.16. The comparison of RI curve of AAR28 and 96P165

TE and TM polarization states of 96P165 ridge laser were measured. Below the threshold, there were both the two polarizations as shown in Fig. 6.17. TM mode emission was dominant. When the current was above the threshold, the laser operates on TM mode as shown in Fig. 6.18. The length of this sample (96P165-A3) is 555 μm and the ridge width is 3 μm. The current density threshold is around 3 kA/cm^2.

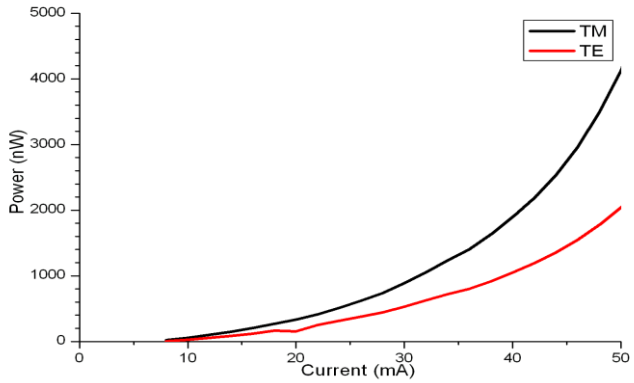

Fig. 6.17. TE and TM emissions of 96P165-A3 below threshold.

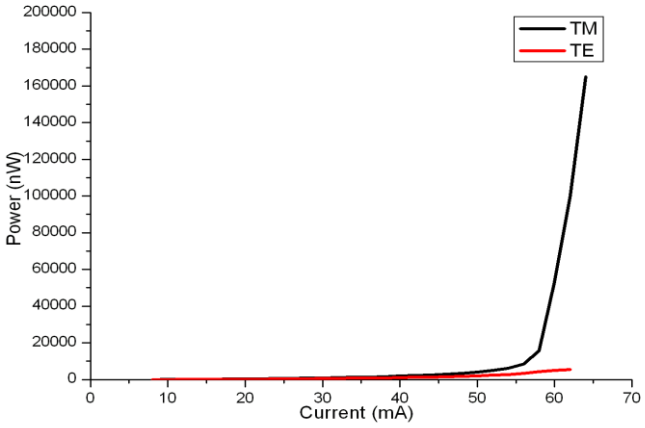

Fig. 6.18. TE and TM emissions of 96P165-A3 above threshold

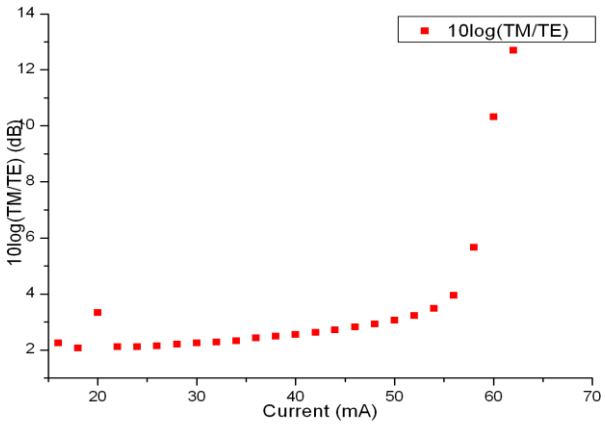

Fig. 6.19. The extinction ratio of TM over TE polarization of 96P165-A3 in dB.

The extinction ratio of TM over TE mode was measured as shown in Fig. 6.19. The extinction ration increased with the current.

In conclusion, a laser diode working on TM mode by using tensile-strained quantum wells has been designed, fabricated and characterized. The active region consists of 3 QWs of $GaAsP_{10\%}$. The ridge of laser diode was etched by ICP, with a width of 3µm, height of 1µm. The central wavelength is 810 nm. This device can be a building block of the integrated sensor on GaAs system.

6.3 Conclusion

In this chapter, the waveguides with buried oxidation layer were fabricated on standard sample and SL sample. A 3-period SL was inserted between the bulk $Al_{0.34}Ga_{0.66}As$ waveguide core and the lower cladding $Al_{0.34}Ga_{0.66}As$ which is to be oxided. The waveguides were measured by FP method at a long wavelength range (50 nm) using broad band SLD source. The propagation loss at 1550 nm (~18 dB/cm) was consistent with the value reported in literature of a similar structure. No significant loss difference was found between standard structure and SL structure at 1550 nm. However, the loss at 830 nm was considerably high (in the order of 150 dB/cm), probably mainly due to the interface scattering loss at short wavelength. The quality of the waveguide was not improved by smooth wet etching indicating that in our case the sidewall was not critical to the huge loss. A SL sample has been prepared for the STEM observation of the interface of SL/oxide along the light propagation direction. However, no noticeable defects, gaps or delamination was found to explain the irregular fringes of waveguide samples with SL. In parallel, an FP laser working on TM mode was demonstrated which can be a building block for highly sensitive monolithically integrated circuit.

Reference

[1] A. Densmore, D.-X. Xu, P. Waldron, S. Janz, P. Cheben, J. Lapointe, A. Delâge, B. Lamontagne, J. H. Schmid, and E. Post, "A Silicon-on-Insulator Photonic Wire Based Evanescent Field Sensor," IEEE Photon. Technol. Lett., 18, 2520-2522, 2006.

[2] L. Scaccabarozzi, M. M. Fejer, Y. Huo, S. Fan, X. Yu, and J. S. Harris, "Enhanced second-harmonic generation in AlGaAs/Al_xO_y tightly confining waveguides and resonant cavities", Opt. Lett., 31, 3626-3628, 2006.

[3] M. Ravaro, M. Le Dû, J.-P. Likforman, S. Ducci, V. Berger, and G. Leo, "Estimation of parametric gain in GaAs/AlO_x waveguides by fluorescence and second harmonic generation measurements," Appl. Phys. Lett., 91, 191110, 2007.

[4] E. Guillotel, M. Ravaro, F. Ghiglieno, C. Langlois, C. Ricolleau, S. Ducci, I Favero, and G. Leo, "Parametric amplification in GaAs/AlO_x waveguide,"Appl. Phys. Lett., 94, 171110, 2009.

[5] Marc Savanier, Alessio Andronico, Aristide Lemaître, Christophe Manquest, Ivan Favero, Sara Ducci, and Giuseppe Leo, "Nearly-degenerate three-wave mixing at 1.55 μm in oxidized AlGaAs waveguides," Opt. Express, 19, 22582-22587, 2011.

[6] D. Sun, and D. W. Treat, "Low-threshold 833-nm GaAsP-AlGaAs tensile-strained quantum-well laser diodes," IEEE Photon. Technol. Lett., 8, 13-15, 1996.

[7] D. Sun, D. P. Bour, K. J. Beernink, D. W. Treat and R. Bringans, "TE/TM cross-polarization laser diodes using tensile-strained quantum wells," SPIE, 2682, 108-115, 1996.

[8] F. Agahi, K. M. Lau, Hong. K. Choi, A. Baliga, and Neal. G. Anderson, "High-performance 770-nm AlGaAs-GaAsP tensile-strained quantum-well laser diodes," IEEE Photon. Technol. Lett., 7, 140-143, 1995.

[9] A. D. Rossi, V. Ortiz, and M. Calligaro, "Measuring propagation loss in a multimode semiconductor waveguide," J. Appl. Phys., 97, 073105, 2005.

[10] M. Ravaro, "Nonlinear GaAs/AlOx waveguides for parametric down-conversion," thesis, 2008.

[11] F. Grillot, L. Vivien, S. Laval, and E. Cassan, "Propagation loss in single-mode ultrasmall square silicon-on-insulator optical waveguides," J. Lightwave Technol., 24, 891-896, 2006.

CHAPTER 7

Conclusion

The objective of the thesis was to develop fully integrated micro-ring resonator sensors based on high refractive index contrast waveguides. Compared to all-passive cascaded double-ring sensor, the integration of a laser on the sensor chip will eliminate the need for an external light source and fiber coupling, thus resulting in more compact, robust and low-cost devices.

Major simulation methods related to waveguide analysis and resonance computation of ring resonators have been illustrated and the effects of key parameters have been discussed.

As a preliminary demonstration, an optical biosensor based on the cascade of a Fabry-Perot cavity laser and a micro-ring resonator is investigated theoretically and experimentally. The device explored intensity interrogation method which is a quite new concept used only by two groups in the world. A detection limit in the order of 10^{-5} RIU has been achieved in the preliminary experiment which is more than twice that of the double-ring resonator with a potential detection limit up to 10^{-7} RIU. The free spectral ranges of ring and Fabry-Perot cavity laser are deliberately matched to enable implement of the Vernier effect. By using intensity interrogation, the approach didn't require expensive tunable laser or optical spectrum analyzer. Instead, our method using low-cost easy-to-fabricate Fabry-Perot cavity laser and photodetectors provides high potential for miniature integrated economic devices for a large number of consumers. In our experiments, the ring and laser were fabricated separately and connected by an optical fiber to demonstrate its principle. It should be noted that although discrete FP laser is used in our proof-of-principle experiment, it demonstrate the feasibility of a heterogeneous integration of ring or Fabry-Perot cavity laser with the cavity length more accurately defined by photolithography.

To achieve practical and reliable devices, the impact of the fluctuation of temperature and the drift of laser's emitting wavelength has to be taken into consideration. A complete design based on a Fabry-Perot cavity laser and two ring resonators is also proposed and investigated to address the stability issues. In this scheme, a reference ring is added to compensate the influence of environmental temperature fluctuation and the wavelength drift of the laser. The simulation and analysis are performed on silicon-on-insulator material system but it can be easily transplanted to other substrates. For some applications when smaller rings are favorable (i.e. fabricated on expensive or lossy material system), single-mode laser is an alternative source for adopting small rings.

In parallel, the GaAs system is explored experimentally to pave the way to future monolithic integration. As a technology to achieve high refractive index contrast, wet oxidation was chosen and used for conversion from $Al_{0.92}Ga_{0.08}As$ to low index Al_xO_y. During the fabrication, a vertical oxidation crossing the Al_xO_y /AlGaAs or Al_xO_y /GaAs interface was discovered. The interface was investigated thoroughly by scanning transmission electron microscopy and energy-dispersive X-ray spectroscopy and the vertical oxidation can be dramatically restrained by the superlattice structure within several nm. The vertical oxidation rate of superlattice structure is much slower than bulk $Al_{0.34}Ga_{0.66}As$, even slower than bulk GaAs. Furthermore, the interface between superlattice and the oxide is smoother than the interface between bulk alloys and oxide. Experimental results show that hydrogen plays a key role to the activation of the oxidation

of GaAs. Besides hydrogen, surface state of the sample is also found critical in the mechanism of the vertical oxidation.

The waveguides with buried oxidation layer were fabricated and measured by Fabry-Perot method. The propagation loss at 1550nm was consistent with the value reported in literature with a similar structure. No remarkable difference was found between standard structure and superlattice structure. However, the loss at 830nm was rather high especially with the superlattice samples probably because of the scattering loss which is dominant at short wavelength. Meanwhile, an Fabry-Perot cavity laser working on TM mode was demonstrated which can be a building block for highly sensitive monolithically integrated circuit given that TM mode allows higher sensitivity than TE mode.

We have made progress as summarized above but still face several challenges in future works. To finally realize a ready-to-use, robust, reliable and cost-effective integrated sensors, we have to put in more efforts in the following directions. Firstly, the scheme with compensation ring needs to be accomplished experimentally. Secondly, the sensor is currently used to detect the ambient refractive index of homogeneous analytes. Combined with microfluidics, it can see much more biomedical applications by detecting molecules or particles. Finally, the oxidation process of AlGaAs/GaAs needs to be further studied and optimized to form high quality oxide and smooth interface and consequently the optical loss of the waveguide have to be minimized based on the advanced oxidation process.

COMMUNICATIONS

"Improvement of the oxidation interface in an AlGaAs/AlxOy waveguide structure by using a GaAs/AlAs superlattice,"Jinyan song, Sophie Bouchoule, Gilles Patriarche, Elisabeth Galopin, Alejandro M. Yacomotti, Edmond Cambril, Qingli Kou, David Troadec, Jian-Jun He, and Jean-Christophe Harmand, Phys. Status Solidi A-Appl. Mat. 1-7, 2013.

"High-Sensitivity Silicon Photonic Biosensors Based on Cascaded Resonators," Xianxin Jiang, Jinyan Song, Lei Jin, and Jian-Jun He, invited paper, Proceedings of SPIE, Photonics Asia, November 5-7, 2012.

"Intensity interrogated sensor based on cascaded Fabry-Perot laser and micro-ring resonator", Jinyan Song, Lei Wang, Lei Jin, Xiang Xia, Qingli Kou, Sophie Bouchoule, and Jian-Jun He, J. Lightwave Technol. 30, pp. 2901-2906, 2012.

"Picosecond to sub-picosecond pulse generation from mode-locked VECSELs at 1.55 μm," S. Bouchoule, Z. Zhao, A. Khadour, E. Galopin, J.-C. Harmand, J. Song, G. Aubin, J. Decobert, J.-L. Oudar, Proc. SPIE 8242, 824203, 2012.

"Subpicosecond pulse generation from a 1.56 μm mode-locked VECSEL", Zhuang Zhao, Sophie Bouchoule, Jinyan Song, Elisabeth Galopin, Jean-Christophe Harmand, Jean Decobert, Guy Aubin, and Jean-Louis Oudar, Optics Letters, Vol. 36, Issue 22, pp. 4377-4379, 2011.

Chinese patent: "An optical sensor based on cascade active cavity and passive cavity," patent number 201010206558.7, Jinyan Song, Tingting Yu, Jian-Jun He, and Qingli Kou, issued May 2, 2012.

SYNTHESE EN FRANCAIS

La détection rapide des analytes chimiques et biologiques présente un intérêt croissant en raison d'une grande variété d'applications, comprenant par exemple le contrôle de la qualité, le diagnostic des maladies, la reconnaissance molécule biologique et la surveillance de l'environnement. Le secteur de la détection optique suscite un intérêt mondial et de nombreuses technologies innovantes sont en cours d'élaboration.

La plupart des travaux concernant les capteurs optiques décrits dans la littérature utilisent un interféromètre passif tel qu'un interféromètre de Mach-Zehnder, cavité de Fabry-Perot (FP), ou un résonateur en anneau à base de silicium sur isolant (SOI) ou du plate-forme de la silice. Une source de lumière externe est nécessaire dans ce cas, ce qui conduit à des complications sur le couplage optique et l'emballage. L'objectif de la thèse était de réaliser un capteur optique ultra-compact, potentiellement faible-coût, haute-sensibilité. Deux approches ont été explorées: l'intégration hybride et l'intégration monolithique.

Concernant l'intégration hybride, nous avons étudié théoriquement et expérimentalement un biocapteur ultrasensible interrogé en intensité et composé en cascade d'un laser Fabry Pérot et d'un résonateur en anneau en SOI. Le système utilise un laser FP à faible-coût et facile-à-fabriquer pour servir comme un peigne de référence pour l'anneau de détection. Ses pics d'émission étroits avec une haute densité de puissance spectrale ont améliorent la sensibilité du capteur d'un facteur deux par rapport à capteur tout passif à double anneaux précédemment étudié.

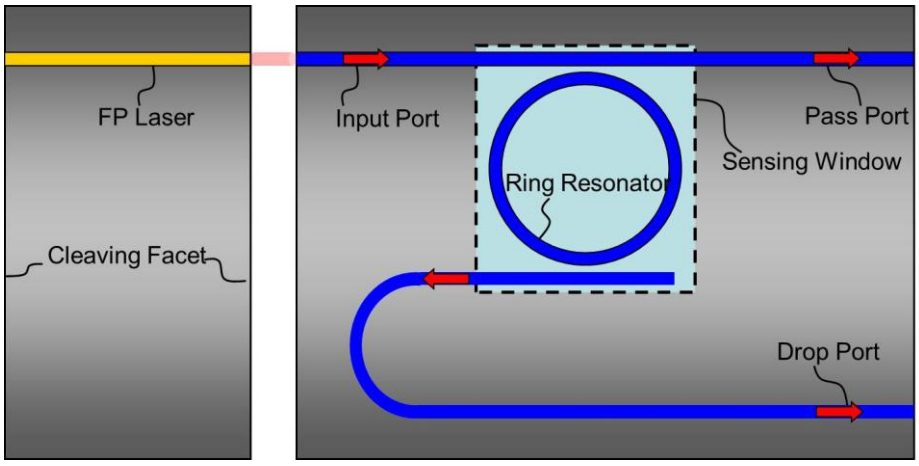

Fig. 1. Schéma du capteur composé en cascade d'un laser FP et d'un résonateur en anneau en SOI.

La Fig. 1 montre la structure du dispositif réalisé. La sortie d'un laser FP est couplée à un seul micro-résonateur en anneau à travers l'entrée du guide d'ondes. La lumière correspondant à des longueurs d'onde de résonance de l'anneau est transmise à travers l'anneau par la voie de sortie « Drop Port » alors que la lumière de toutes les autres longueurs d'onde est transmise directement à travers la voie « Pass Port ». Le laser FP peut être remplacé par un laser en anneau utilisant le même principe de travail.

Dans le dispositif réalisé par cette expérience, le laser FP est fabriqué sur le matériau InP, tandis que le résonateur en anneau est fabriqué en SOI pour sa haute sensibilité. Les plages spectrales libres (FSR) de la cavité FP et du résonateur en anneau sont conçues pour être aussi proches que possible pour obtenir une haute sensibilité avec la méthode d'interrogation en intensité. La puissance de sortie est mesurée par un détecteur à l'extrémité de la voie « Drop Port » de l'anneau.

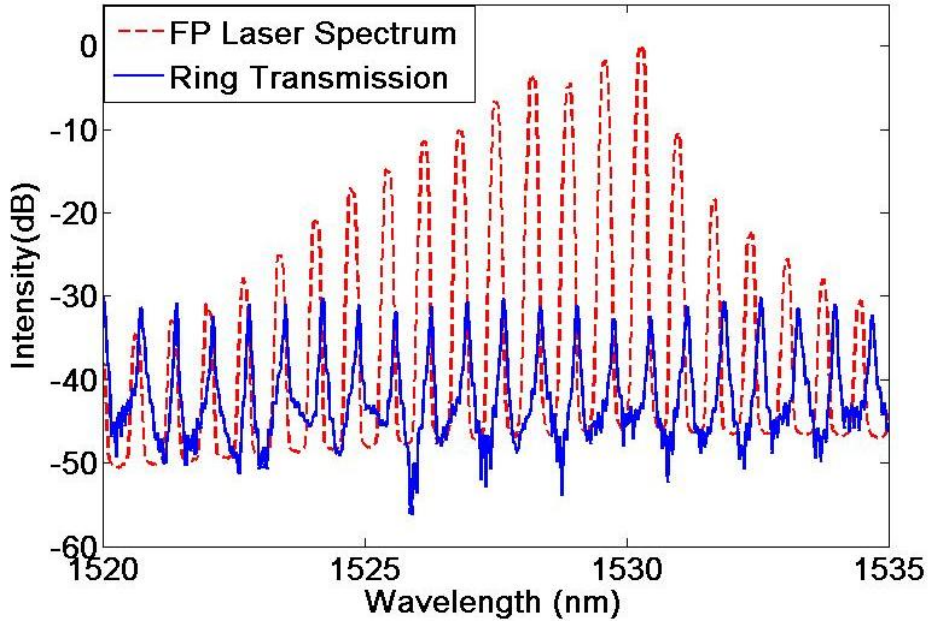

Fig. 2. Spectre du laser FP (trait pointillé) et spectre de transmission (trait plein) du résonateur montrant les FSRs presque identiques.

La Fig. 2 montre le spectre d'émission du laser FP mesuré par un analyseur de spectre optique (OSA) et le spectre de transmission du résonateur en anneau mesuré à l'aide d'un

laser accordable en tant que source et un détecteur de puissance. Une différence de FSR de moins de 1% a été atteinte entre l'anneau et le laser FP. Le centre de longueur d'onde d'émission du laser FP est 1528nm et la largeur à mi-hauteur (FWHM) de la fonction de distribution de puissance est d'environ 3 nm.

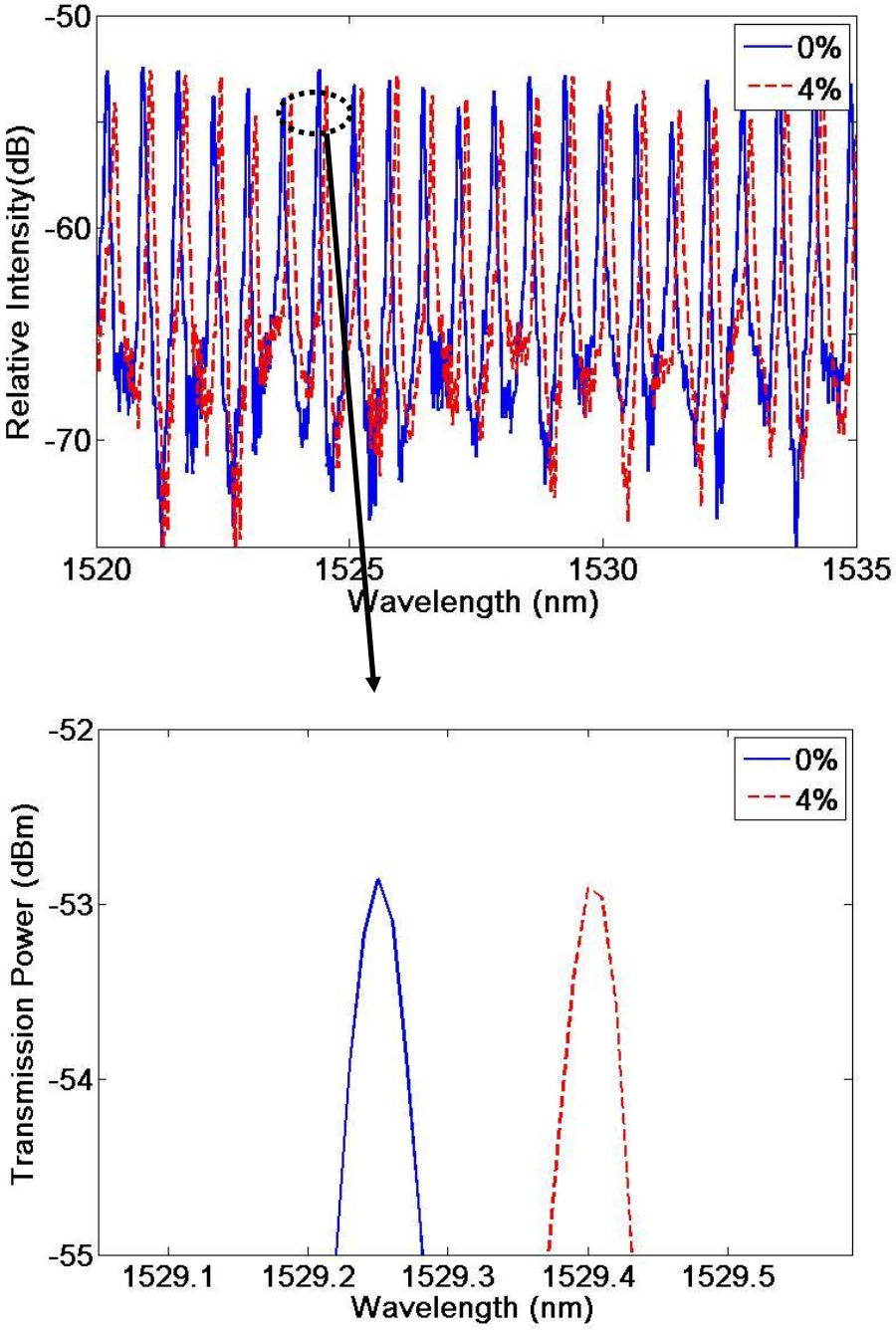

Fig. 3. Spectre de transmission de l'anneau à différentes concentrations de NaCl.

La Fig. 3 représente les spectres de transmission du résonateur en anneau mesurés à l'aide d'un laser accordable lorsque l'anneau de détection est exposé à des solutions aqueuses de NaCl à différentes concentrations de 0% à 4%. L'indice de réfraction d'une solution aqueuse de NaCl varie de 0,0017 à 0,0018 ~ RIU par% en masse. La sensibilité de changement de longueur d'onde de l'anneau est donc d'environ 22nm/RIU.

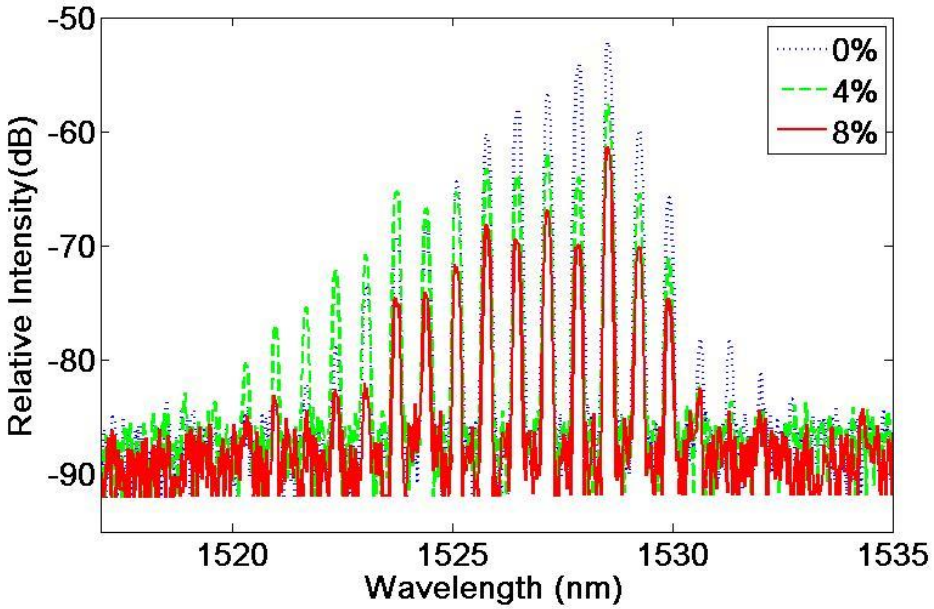

Fig. 4. Spectres à la sortie du capteur mesurés à différentes concentrations d'une solution de NaCl.

La Fig. 4 représente les spectres à la sortie du capteur mesurés à différentes concentrations d'une solution de NaCl de 0%, 4% et 8% lorsque le laser FP est utilisé comme source d'entrée. Lors de la configuration, le courant et la température du laser FP ont été ajustés de sorte que les pics de résonance du laser sont bien alignés avec les pics de l'anneau afin d'obtenir la puissance de sortie maximale lorsque la concentration de la solution de NaCl est nulle.

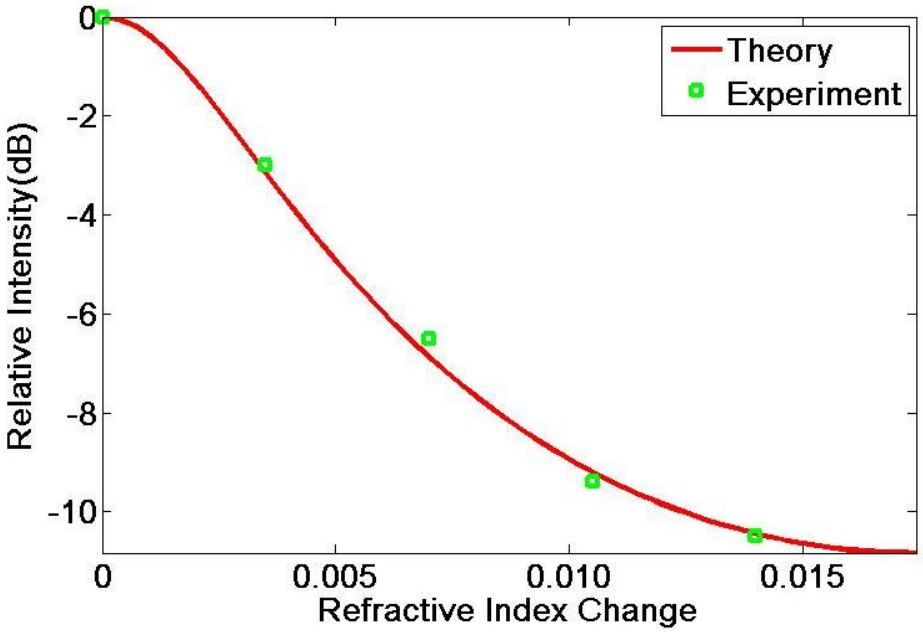

Fig. 5. Puissance de sortie normalisée en fonction du changement de l'indice de diffraction des solutions de NaCl.

La Fig. 5 montre la puissance de sortie normalisée par rapport à la variation de l'indice de réfraction de l'échantillon des solutions aqueuses de NaCl à différentes concentrations. En ajustant les données mesurées avec le calcul théorique, nous avons déterminer le facteur de qualité Q de l'anneau simple qui est d'environ $1{,}1\times10^{4}$. Ceci correspond à un coefficient de couplage entre l'anneau et les guides d'ondes de bus de 43%, en supposant que la perte de propagation est 1dB/cm et les FSR de l'anneau et la cavité FP sont 0,7 nm et 0,693 nm respectivement. La sensibilité du capteur atteint environ 1000dB/RIU (unité d'indice de réfraction). Cette sensibilité est plus de deux fois que celle du capteur en double anneaux en cascade, fabriqué à partir d'une même plaquette que le résonateur en anneau simple utilisé dans l'expérience actuelle. Cette sensibilité est aussi beaucoup plus élevée que celle du capteur SPR interrogé en l'intensité. En supposant que la précision de mesure de la puissance relative est 0,01dB (réalisable avec un capteur de puissance Agilent, par exemple), la limite de détection de la variation d'indice de réfraction est égal à 1×10^{-5}.

Ce résultat expérimental préliminaire devrait pouvoir être amélioré en optimisant le coefficient de couplage entre l'anneau et les guides d'ondes en augmentant le facteur de qualité Q du résonateur en anneau. En raison de la densité spectrale de la puissance élevée

du laser FP, les pics de résonance plus pointus de l'anneau peuvent se traduire par une plus grande sensibilité sans dégrader la puissance de sortie. Notre analyse théorique montre que la sensibilité peut atteindre à 5000dB/RIU en diminuant le coefficient de couplage de 40% à 10%. En outre, en utilisant un guide d'onde profondément gravé avec largeur plus étroite, ce qui peut être réalisé par lithographie par faisceau d'électrons, la perte de propagation pour le mode TM peut être réduit de façon drastique et le capteur peut fonctionner en mode TM avec la sensibilité améliorée par un ordre de grandeur par rapport au mode TE. Cela conduit à une limite de détection d'indice de réfraction d'environ 2×10^{-7}.

Nous avons amélioré la conception en utilisant un anneau de référence afin d'offrir une compensation de température. L'instabilité de longueur d'onde du laser et de l'anneau peut être surveillée et contrôlée au cours de la détection. Seuls trois détecteurs sont nécessaires pour appliquer la méthode d'interrogation en intensité. Une limite de détection de l'indice de réfraction de l'ordre de 10^{-6} peut être obtenue qui correspond à un déplacement de longueur d'onde de 0,06 pm.

Pour explorer le potentiel de l'intégration monolithique, nous avons étudié l'interface entre l'oxyde et non oxyde après l'oxydation de AlGaAs enterré. L'oxydation verticale de GaAs ou AlGaAs avec un teneur faible en Al activée par une couche voisine oxydée de AlGaAs avec un teneur riche en Al a été démontrée expérimentalement. L'oxydation verticale provoque l'oxydation inattendue des couches adjacentes et ajoute une rugosité supplémentaire à l'interfaces oxyde/non-oxyde ce qui est préjudiciable à la fabrication de guides d'ondes optiques. Une structure de super-réseau (SL) a été proposée afin de limiter l'oxydation verticale. L'échantillon du super-réseau a montré une résistance plus grande contre l'oxydation à travers l'interface d'$Al_{0.34}Ga_{0.66}As$ massif, et aussi d'GaAs massif.

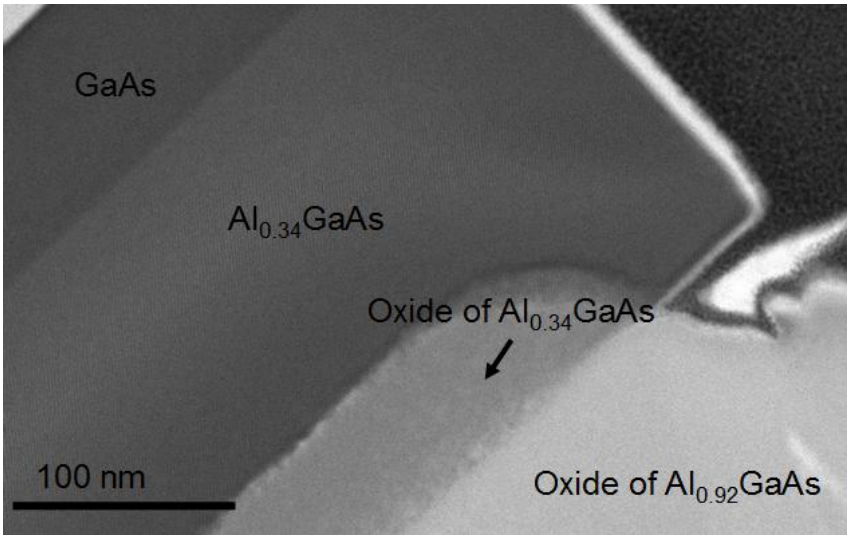

Fig. 6. Image BF-STEM (Bright field scanning transmission electron microscopy) de l'interface $Al_{0.34}Ga_{0.66}As/Al_{0.92}Ga_{0.08}As$ par l'oxydation humide près du paroi de mesa oxydé pendant 30 mn à 420 °C.

L'interface entre GaAs et la couche oxydée d'$Al_{0.92}Ga_{0.08}As$ est représentée sur la Fig. 6. La sous-couche de GaAs a été oxydée avec une vitesse d'oxydation inférieure à celle de la couche d'$Al_{0.34}Ga_{0.66}As$. La profondeur de l'oxydation de GaAs a culminé à 40 nm près du bord de la mesa. Le pourcentage atomique d'As resté dans le GaAs oxydé est environ 3%, mesuré par la spectroscopie de la dispersion d'énergie des rayons X (EDX), ce qui indique que l'oxydation de GaAs en Ga-oxyde a été presque complète. D'autre part, la surface de GaAs directement exposée à l'ambiance n'était pas oxydée, similaire au cas d'$Al_{0.34}Ga_{0.66}As$. D'après les figures 6 et 7, l'oxydation verticale ne se produit pas au bord latéral. Au centre de la mesa, l'épaisseur d'$Al_{0.34}Ga_{0.66}As$ oxydée et des couches de GaAs ont été réduites à 14 nm et 8 nm respectivement.

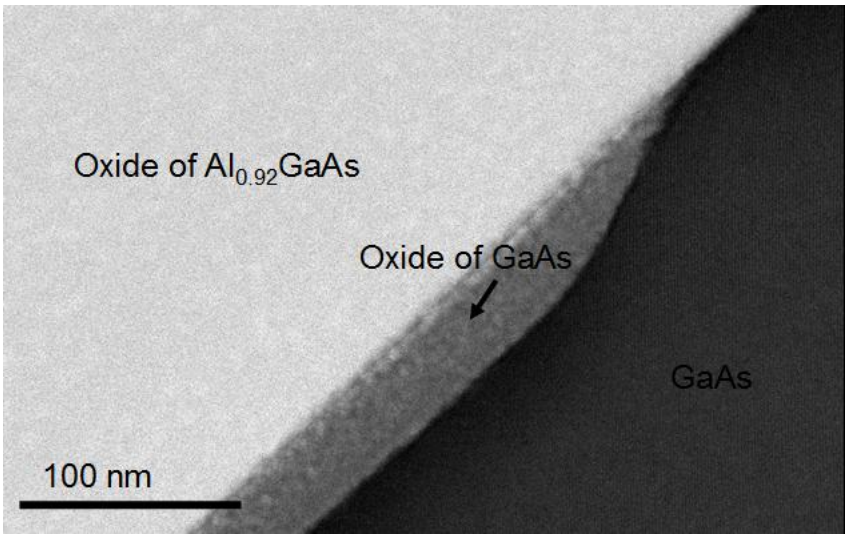

Fig. 7. Image BF-STEM (Bright field scanning transmission electron microscopy) de l'interface Al_0 $Al_{0.92}Ga_{0.08}As$/GaAs par l'oxydation humide près de la paroi de mesa oxydé pendant 30 mn à 420 °C.

Comme pour l'échantillon SL avec un temps d'oxydation de 30 min, la vitesse d'oxydation d'$Al_{0.92}Ga_{0.08}As$ était la même que celle de la structure standard. Les couches SL ont également été oxydées du bord latéral de la mesa avec une longueur d'oxydation de 230 nm comme indiquée dans la Fig. 8. Par l'analyse EDX, on voit que les couches SL ont été totalement oxydées avec 1,5% d'As en résidu (valeur moyenne). La vitesse d'oxydation latérale du SL est en effet sensiblement réprimée lorsque l'épaisseur de la couche de AlAs est diminuée. Il est clair dans l'image STEM de la Fig. 8 que les couches oxydées SL présentent encore des contrastes différents correspondant à Ga-oxyde et Al-oxyde.

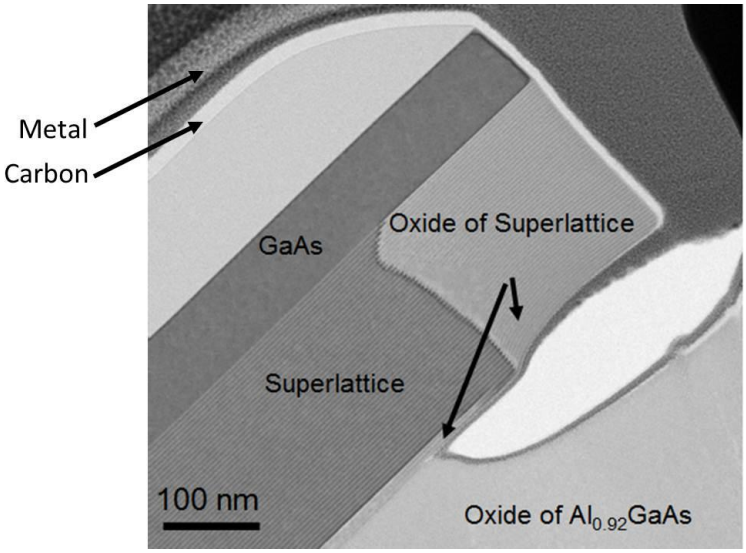

Fig. 8. Image BF-STEM (Bright field scanning transmission electron microscopy) de l'interface SL/$Al_{0.92}Ga_{0.08}As$ par l'oxydation humide près du paroi de mesa oxydé pendant 30 mn à 420 °C. Incorporation du carbon et métal est due à la préparation du focused ion beam (FIB).

Lorsque l'on regarde l'interface entre le SL et la couche oxydée en fort teneur d'Aluminium, il a été constaté que seuls trois périodes du SL (~ 12 nm) ont été oxydées à partir de l'interface près du bord de mesa, dont l'épaisseur est beaucoup moins grande que la profondeur d'oxydation dans l'$Al_{0.34}Ga_{0.66}As$ massif (~ 65 nm), et de façon plus surprenante moins grande que la profondeur de l'oxydation dans GaAs massif (~ 40 nm). Au centre de mesa l'oxydation verticale dans la couche du SL a été limitée à 1 période (4 nm). À la même position latérale, l'épaisseur de l'oxyde du SL est plus petite que celle de l'oxyde d'$Al_{0.34}Ga_{0.66}As$, et même à celle du GaAs-oxyde qui ne peut pas être expliquée simplement par la composition d'Aluminium de la matière.

Le traitement par plasma d'hydrogène d'une surface de GaAs sèche-gravée a permis l'oxydation de GaAs massif, qui a montré le rôle clé de l'incorporation d'hydrogène dans l'activation du processus d'oxydation de GaAs ou AlGaAs avec l'Aluminium en teneur faible.

Enfin, les guides d'ondes avec les couches d'oxydation enterrées ont été fabriqués sur l'échantillon standard et sur l'échantillon en super-réseau. Un SL de 3-périodes a été inséré entre le cœur de guide d'ondes d'$Al_{0.34}Ga_{0.66}As$ massif et le gaine inférieure

d'$Al_{0.92}Ga_{0.08}As$ qui doit être oxydé. Les guides d'ondes ont été mesurés par la méthode de Fabry-Pérot à une large plage de longueur d'onde (50 nm) en utilisant une source à diode super-luminescente large bande. La perte de propagation à 1550 nm (~ 18dB/cm) était compatible avec la valeur rapportée dans la littérature d'une structure similaire. Aucune différence de perte significative n'a été trouvée entre la structure standard et la structure du SL à 1550 nm. Toutefois, la perte à 830 nm est largement plus élevée (de l'ordre de 150dB/cm), sans doute due principalement à la perte par diffusion à l'interface à courte longueur d'onde. En parallèle, un laser FP travaille en mode TM a été réalisé et caractérisé ce qui peut être un élément de brique important du circuit intégré monolithique du biocapteur sensible.

RESUME

Ce travail de thèse porte sur la conception et la réalisation de capteurs optiques ultracompacts et sensibles utilisant le mode d'interrogation en intensité pour la détection d'analytes chimiques et biologiques. Deux approches, l'intégration hybride et l'intégration monolithique, ont été explorées durant cette thèse. Après un descriptif des outils d'analyse et de conception de guides d'onde et de micro résonateurs en anneaux, le manuscrit présente l'intégration hybride d'un laser Fabry-Perot en semiconducteur III-V avec un résonateur en anneau basé sur du matériau SOI. Le laser Fabry-Perot à faible coût fonctionnant en multimode longitudinal a été utilisé comme peigne de référence pour le résonateur en anneau en contact avec un échantillon liquide. L'effet Vernier a été implanté dans le système de détection en utilisant le mode d'interrogation en intensité. La largeur spectrale étroite du laser avec sa densité de puissance élevée ont permis d'obtenir un capteur de plus haute sensitivité en comparaison avec le capteur en double anneaux réalisé précédemment. Une étude numérique d'un capteur composé d'un laser Fabry-Perot et deux résonateurs en anneaux permettant de compenser la fluctuation de température a été ensuite présentée. Concernant l'intégration monolithique, l'interface entre oxyde et non-oxyde après l'oxydation de AlGaAs a été étudiée au Central de Technologies du LPN/CNRS. Un phénomène d'oxydation verticale de GaAs ou AlGaAs avec une faible teneur en aluminium activée par une couche voisine oxydée de AlGaAs avec une forte teneur en aluminium a été identifié expérimentalement. Afin de limiter l'oxydation verticale et de réduire la rugosité des interfaces, des guides d'onde basés respectivement sur une structure intégrant un super-réseau et sur une structure standard ont été fabriqués et caractérisés. L'impact de l'hydrogène sur l'activation du processus d'oxydation de GaAs ou AlGaAs avec une faible teneur en Al a été mis en évidence. Enfin, ce manuscrit décrit la réalisation et la caractérisation d'un laser Fabry-Perot fonctionnant en mode TM. Ce laser constitue une brique important vers l'intégration monolithique d'un capteur extrêmement sensible.

Mots clés: capteurs, laser FP, résonateur en anneau, oxydation humide, superréseau, laser mode TM

ABSTRACT

The objective of the thesis is to realize the integrated optical sensors with high sensitivity using intensity interrogation method for chemical and biological analyte detection. For this purpose, two approaches, hybrid integration and monolithic integration, have been explored theoretically and experimentally during this thesis. After a review of the design and analysis tools of optical waveguide and micro-ring resonators, the manuscript reports an experimental demonstration of a highly-sensitive intensity-interrogated optical sensor based on cascaded III-V semiconductor Fabry-Perot laser and silicon-on-insulator ring resonator. The low-cost easy-to-fabricate Fabry-Perot laser serves as a reference comb for the sensing ring in contact with liquid sample. The Vernier effet has been exploited in the detection scheme using intensity interrogation mode. The sharp emission peaks of the FP laser with high spectral power density result in a high sensitivity for the sensor compared to previously investigated all-passive double-ring sensor. The temperature compensation method has also been investigated numerically to improve the performance of the sensor. Concerning the potential monolithic integration of laser and sensing waveguide, the interface between oxide and non-oxide after wet oxidation of buried AlGaAs has been investigated at the Technology Centre of LPN/CNRS. The vertical oxidation of GaAs or AlGaAs with low Al content activated by a neighbouring oxidized Al-rich AlGaAs layer has been discovered experimentally. To limit the vertical oxidation and reduce the roughness of the interface, the waveguides with buried oxide layer on superlattice sample and standard sample have been fabricated and characterised. The key role of hydrogen incorporation in the activation of the oxidation process for GaAs or AlGaAs materials with low Al content has been shown experimentally. Finally, this thesis reports the fabrication and the characterisation results of a Fabry-Perot laser working on TM mode which is an important building block for highly-sensitive monolithically-integrated circuit.

Keywords: sensor, FP laser, ring resonator, wet oxidation, superlattice, TM mode laser